NON-INNOCENT LIGANDS: FROM PRO-TON SHUTTLE TO PHOTO-ACTIVATION

Adiran de Aguirre Fondevila

UNIVERSITAT ROVIRA I VIRGILI
NON-INNOCENT LIGANDS: FROM PRO-TON SHUTTLE TO PHOTO-ACTIVATION
Adiran de Aguirre Fondevila

UNIVERSITAT ROVIRA I VIRGILI
NON-INNOCENT LIGANDS: FROM PRO-TON SHUTTLE TO PHOTO-ACTIVATION
Adiran de Aguirre Fondevila

Adiran de Aguirre Fondevila

Non-innocent ligands: from pro-ton shuttle to photo-activation

DOCTORAL THESIS

Supervised by

Prof. Feliu Maseras

Institute of Chemical Research of Catalonia

Tarragona

2019

UNIVERSITAT ROVIRA I VIRGILI
NON-INNOCENT LIGANDS: FROM PRO-TON SHUTTLE TO PHOTO-ACTIVATION
Adiran de Aguirre Fondevila

ICIQ - Institut Català d'Investigació Química

Avgda, Països Catalans 16,

43007 Tarragona (Spain)

Prof. Feliu Maseras, Group Leader at the Institute of Chemical Research of Catalonia,

I STATE that the present study, entitled "Non-innocent ligands: from proton shuttle to photo-activation" presented by Adiran de Aguirre Fondevila for the award of the degree of Doctor, has been carried out under my supervision in my group at the Institute of Chemical Research of Catalonia and that it fulfills all the requirements to be eligible for the International Doctor Distinction.

Tarragona, September 2nd, 2019

Doctoral Thesis Supervisor

Prof. Feliu Maseras

UNIVERSITAT ROVIRA I VIRGILI
NON-INNOCENT LIGANDS: FROM PRO-TON SHUTTLE TO PHOTO-ACTIVATION
Adiran de Aguirre Fondevila

Acknowledgments

The elaboration of this thesis would not have been possible without the support of many friends and co-workers.

Sóc una persona que li costa una mica obrir-se i expressar els sentiments, però en aquest cas intentaré fer un esforç per agrair a tothom qui m'ha acompanyat durant aquests anys.

Vull començar donant les gràcies al meu supervisor, el professor Feliu Maseras. La veritat és que jo mai he sigut dels millors estudiants. Tot i així, em va donar l'oportunitat de realitzar les pràctiques del Grau de Química durant el meu últim any d'universitat, per després oferir-me fer el màster i el doctorat sota la seva tutela. He après molt durant tots aquests anys al seu grup, sobretot científicament. Però també he après personalment: paciència, perseverança i amabilitat. Considero que és molt important poder tindre a un supervisor proper en qualsevol feina, i en Feliu sempre ha sigut el millor "jefe" possible.

També m'agradaria agrair a tots els membres actuals i passats dels tres grups teòrics de l'ICIQ. Sempre hem compartit bons moments tant dins com fora del laboratori i de tots ells he après coses noves. Sobretot als professors Núria López i Carles Bo els quals sempre han compartit la seva experiència amb mi i m'han ajudat sempre que han pogut. Menció especial també per la Maria Besora, la qual sempre ha sigut com una mare dins del nostre grup i espero que li vagi molt bé ara a la URV. No puc oblidar-me en aquest apartat a les persones que fan que els grups teòrics funcionin: Nuria Vendrell, Martin Gumbau i Moises Álvarez. Sense ells la nostra vida diària durant el doctorat seria molt més difícil. Gràcies per tota l'ajuda amb els temes burocràtics i informàtics, i perdoneu tots els mals de cap que us he pogut fer vindre!

Vull agrair també al doctor Joan González. Ell va obrir el camí per poder fer les pràctiques de la carrera a l'ICIQ i gràcies a això jo vaig poder-

les fer al grup del Feliu. No sé on acabaràs (segurament al món de la política!) però espero que segueixis amb el teu altruisme i entusiasme allí on et porti la vida. Moltes gràcies també per tota l'ajuda durant els últims mesos d'escriptura!

M'agradaria donar les gràcies també al Haijun Jiao i a tots els membres del seu grup, en especial a la Zhiong Wei. Em van acollir de forma extraordinària durant el temps que va durar la meva estança al seu grup. Des d'un punt de vista personal, la relació amb ells va ser extraordinària, tot i la cultura i l'idioma diferent, em vaig sentir com a casa.

Han sigut quatre anys de doctorat. Com és normal, no tots els dies han sigut bons. Per això vull agrair a l'Ignacio Funes, antic membre del grup, per totes les xerrades que hem tingut en el temps que dura un cigarro. Amb l'antisocial que acostuma a ser ell, té encara més mèrit haver-nos fet amics. Un altre gran amic que m'emporto del doctorat és el Pablo Garrido. Ell i en Funes em van acollir durant els primers dies de màster i vam aconseguir formar "el nucli" d'una forta amistat, tant dins com fora de l'ICIQ. Hem compartit moltes nits i riures, sovint començant amb un bon plat de "lasaña al estilo Funes". Menció especial per les seves respectives parelles, l'Elena i la Marta, que encara no sé com han pogut aguantar-los per més de 10 anys! Espero que tot i els kilòmetres que ens separen, sempre trobem alguna ocasió per veure'ns.

No em puc oblidar tampoc d'altres grans amics, Sergi, Marcos, Victor, Fernando i molts altres que segur que em deixo. Hem passat moltes hores junts, dins i fora de l'ICIQ, i de tots d'ells m'emporto alguna cosa positiva. Gràcies també als "Echavarrinos" que van accedir a adoptar-me a l'hora de dinar durant els últims mesos de doctorat, i s'han convertit ara en bons amics. També he de mencionar a tots els amics que he fet al món de l'escalada. En especial a la Jana, que ja és part de la família! No puc tampoc oblidar a la meva amiga Denisse, que m'acompanya fa incomptables anys i que tot i no passar pels millors mesos de la seva

vida, sempre ha tingut temps per preguntar-me i oferir-me la seva ajuda. Dintre d'uns anys quan tornem a llegir això ens riurem de tots els problemes passats i superats! També a la Roser, que tot i no veure'ns gaire, quan ho fem sempre sembla que no ha passat el temps. Espero que segueixi així durant molts més anys!

No em puc oblidar tampoc de la Sílvia que ha sabut plasmar d'una manera increïble la portada de la tesi. Moltes gràcies!

Agrair també a la meva família, tant d'aquí com de Bèlgica. Sobretot als meus pares, per tot el suport i consells durant aquests quatre anys, tot i no entendre gaire que és el que feia davant de l'ordinador. També a mon germà, que m'ha ajudat amb algunes "figuretes" i sempre s'ha interessat pel que feia. Per fi has trobat el que t'agrada, estic molt orgullós de tu.

Per acabar, les últimes línies vull que siguin per la persona més important. Bruna, vas arribar l'última però xafant fort. Gràcies per totes les hores que has passat ajudant-me, escoltant-me i també fent-me oblidar, per una estona, els moments durs del doctorat. No sé què faria sense tu. No sé on ens portarà el futur, si haurem d'estar un temps separats o no, però estic segur que junts aconseguirem superar qualsevol cosa. Urbanització, tu ja m'entens. T'estimo.

UNIVERSITAT ROVIRA I VIRGILI
NON-INNOCENT LIGANDS: FROM PRO-TON SHUTTLE TO PHOTO-ACTIVATION
Adiran de Aguirre Fondevila

Funding Agencies

ICIQ
Institut Català d'Investigació Química

UNIVERSITAT ROVIRA i VIRGILI

Generalitat de Catalunya
Departament d'Innovació, Universitats i Empresa

GOBIERNO DE ESPAÑA
MINISTERIO DE EDUCACIÓN, CULTURA Y DEPORTE

List of publications

Related with this thesis:

[1] "The Acetate Proton Shuttle between Mutually *Trans* Ligands" de Aguirre, A.; Díez-González, S.; Maseras, F.; Martín, M.; Sola, E. *Organometallics* **2018**, 37, 2645-2651.

[2] "Computational Characterization of Single-Electron Transfer Steps in Water Oxidation" de Aguirre, A.; Funes-Ardoiz, I.; Maseras, F. *Inorganics* **2019**, 7, 32.

[3] "Four Oxidation States in a Single Photoredox Nickel-Based Catalytic Cycle: A Computational Study" de Aguirre, A.; Funes-Ardoiz, I.; Maseras, F. *Angew. Chem. Int. Ed.* **2019**, 131, 3938-3942.

[4] "Investigating the Stable Redox Partners of a Five-Coordinate Fe(II)[N_2S_2] Complex" Elsby, M. R.; de Aguirre, A.; Krouz, L.; Sears, J. D.; Gabidullin, B. M.; Neiding, M. L.; Bucher, C.; Maseras, F. Baker, R. T. *Manuscript in preparation.*

[5] "Computational modeling of selected photoactivated processes" (Book chapter) de Aguirre, A.; Fernandez-Alvarez, V. M.; Maseras, F. *In Press.*

Not presented in this thesis:

[6] "Exploring the mechanism of aqueos methanol dehydrogenation catalyzed by defined PNP Mn and Re pincer complexes under base-free as well as strong base conditions" Wei, Z.; de Aguirre, A.; Junge, K.; Beller, M.; Jiao, H. *Catal. Sci. Technol.* **2018**, 8, 3649-3665.

[7] "Photoinduced O2-Dependent Stepwise Oxidative Deglycination of a Nonheme Iron(III) Complex" Wegeberg, C.; Fernández-Alvarez, V. M.; de Aguirre, A.; Frandsen, C.; Browne, W. R.; Maseras, F.; McKenzie, C. J. *J. Am. Chem. Soc.* **2018**, 140, 14150-14160.

[8] "Benzyl Alcohol Dehydrogenative Coupling Catalyzed by Defined Mn and Re PNP Pincer Complexes – A Computational Mechanistic Study" Wei, Z.; de Aguirre, A.; Junge, K.; Beller, M.; Jiao, H. *Eur. J. Inorg. Chem.* **2018**, 4643-4657.

[9] "Copper-Catalyzed N—F Bond Activation for Uniform Intramolecular C—H Amination Yielding Pyrrolidines and Piperidines" Bafaluy, D.; Muñoz-Molina, J. M.; Funes-Ardoiz, I.; Herold, S.; de Aguirre A.; Zhang, H.; Maseras, F.; Belderrain, T. R.; Pérez, P. J.; Muñiz, K. *Angew. Chem. Int. Ed.* **2019**, 58, 8912-8916.

[10] "The Role of Electron-Donor Substituents in the Family of OPBAN-Cu Water Oxidation Catalysts: Effect on the Degradation Pathways and Efficiency" de Aguirre, A.; Garrido-Barros, P.; Funes-Ardoiz, I.; Maseras, F. *Eur. J. Inorg. Chem.* **2019**, 2109-2114.

[11] "Robust and efficient hybrid molecular electroanodes based on unprecedented multiple CH—π interactions between new oligomeric water oxidation catalysts and graphitic surfaces" Hoque, M. A.; Gil-Sepulcre, M.; de Aguirre, A.; Elemans, J. A. A. W.; Moonshiram, D.; Matheu, R.; Shi, Y.; Benet, J.; Sala, X.; Lanza, M.; Maseras, F.; Gimbert-Suriñach, C.; Llobet, A. *Manuscript in preparation.*

[12] "A Novel Dihydroimidazopyridine Ligand is Produced by the Photoactivated CO2 Extrusion from an Iron(III) Complex of a Pyridyl Glycyl Ligand" Wegeberg, C.; de Aguirre, A.; Maseras, F.; McKenzie, C. J. *Manuscript in preparation*.

[13] "Solvent-cage-like medium prompts reactivity on mechanochemical reactions: A DFT study" (Provisional title) Pladevall, B. S.; de Aguirre, A.; Maseras, F. *Manuscript in preparation.*

UNIVERSITAT ROVIRA I VIRGILI
NON-INNOCENT LIGANDS: FROM PRO-TON SHUTTLE TO PHOTO-ACTIVATION
Adiran de Aguirre Fondevila

Contents

Abstract

Metal-ligand cooperativity (MLC) exploits the reactive nature of non-innocent ligands for their participation in chemical processes. This behavior is complementary to that of innocent ligands which play a spectator role. The term non-innocent ligand covers a wide variety of behaviors: from ligands that assist in the cleavage or formation of bonds to ligands capable of accepting or donating electrons from/to the metal center or from/to an external source. In this Thesis, we focus on three different categories depending on the performance of the cooperative ligands: proton-responsive ligands, electron-responsive ligands, and photo-responsive ligands. Metal-ligand cooperation can be also found in Nature and some chemists have taken inspiration of it to develop new processes.

Computational Chemistry has gained relevance over the last decades thanks to method developments and to the increase on the computer power. Nowadays, we are able to model a wide variety of chemical reactions of interest, and predict or reproduce the reactivity through the chemical space. In this Thesis, we used Computational Chemistry to perform exhaustive computational studies on the mechanism of three different reactions involving the cooperation between the metal and the ligand. These reactions involve transitions metal complexes, and because of the size of these systems we selected Density Functional Theory (DFT) as the computational methodology to study the mechanism and the electronic structures of the species involved.

The first chapter introduces an overview of previous knowledge on metal-ligand cooperativity with an emphasis on the problems that will be discussed in the thesis. Chapter 2 describes the less-common computational methodologies used during the Thesis. Methods such as

Mössbauer parameter calculations and minimum energy crossing points (MECP) are addressed. We also report a case example of the utilization of the Marcus theory.

In chapter 3, we analyze computationally the behavior of the acetate ligand, in comparison with the chloro ligand, in the transformation of a Ru alkenyl complex to its alkynyl derivative. The active role of the acetate is found to be crucial to achieve the alkynyl complex. The mechanism is a variation of the previously reported ligand-assisted proton shuttle (LAPS). The proton is formally transferred between two mutually *trans* ligands. This work is a collaboration with the group of Prof. Sola (Universidad de Zaragoza).

Chapter 4 covers the computational elucidation of the complex electronic structure of different iron species such as $[Fe^{II}(N_2S_3)]^0$ and its redox partners. We then use this knowledge to unravel the mechanistic profile of the hydroboration of aldehydes catalysed by $[Fe^{II}(N_2S_3)]^0$. This work is a collaboration with the group of Prof. Baker (University of Ottawa).

In chapter 5, we have characterized the full catalytic cycle for the synthesis of indolines catalysed by a dual nickel/photoredox system. The nickel is found in a variety of oxidation states (from Ni(0) to Ni(III)) participating in the mechanism, each one playing a crucial role. The C—I bond activation runs through an halide abstraction mechanism involving a Ni(I) transient species. The formation of the indoline product is accomplished only after oxidation from Ni(II) to Ni(III) by the photoactive ruthenium species. All the reaction steps are computationally characterized and the barrier for the outer-sphere single electron transfer steps is estimated applying the Marcus theory. Finally, possible off-cycle reactions are studied.

UNIVERSITAT ROVIRA I VIRGILI
NON-INNOCENT LIGANDS: FROM PRO-TON SHUTTLE TO PHOTO-ACTIVATION
Adiran de Aguirre Fondevila

UNIVERSITAT ROVIRA I VIRGILI
NON-INNOCENT LIGANDS: FROM PRO-TON SHUTTLE TO PHOTO-ACTIVATION
Adiran de Aguirre Fondevila

Chapter 1

Introduction

1.1 Metal-ligand cooperativity

When we think about homogeneous catalysis, one of the first concepts that comes to mind is transition metal complexes. Historically, the introduction of transition metal catalysts in organic reactions greatly expanded the scope of their reactivity through the introduction of concepts such as oxidative addition, reductive elimination or β-hydride elimination.

In most classical examples of homogeneous catalysis, the focus resides on the metal centre, which is the one that carries out the reaction, while the ligands play mainly a spectator role. Thus, the initial approach applied to modify the reactivity of a system was the replacement of the metal. The approach was refined when a better understanding of the role of the ligands showed that they are able to alter the properties of the metal centre.[1] This has been the starting point of the majority of work in homogeneous organometallic catalysis. The tuning of the elec-

tronic or steric properties of the ligands affects the metal, and can have a huge impact on the reaction outcome such as higher yields, better selectivity or suppression of undesired side reactions. The concept has been taken one step further upon the realization that ligands may have a more active participation in the main steps of the catalytic cycle.[2] These ligands are known as non-innocent ligands owing to their reactive nature during a chemical process. This behaviour differs with and complements that of innocent ligands which "only" contribute through tuning of the metal.

This metal-ligand synergistic cooperation can be also found in Nature.[3] Some synthetic chemists have taken inspiration by natural enzymes to mimic and tune their intrinsical behaviour to produce novel processes.[4,5,6] For example, Rauchfuss and co-workers combined a redox-active ferrocenyl moiety and a pendant nitrogen base to mimic the key features of the [FeFe]-hydrogenase active site.[7] The amine pendant group aids on the heterolytic cleavage of H_2 (Scheme 1.1).

Scheme 1.1 a) Structure of the active site of the natural [Fe,Fe]-hydrogenase and b) Rauchfuss' biomimetic model complex bearing a pendant base and the redox-active moiety.

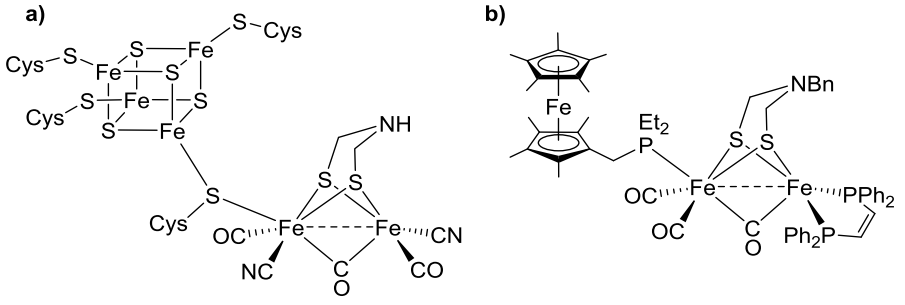

The term non-innocent ligand encompasses a wide variety of behaviours: from ligands that assist in the cleavage or formation of bonds to ligands capable of accepting or donating electrons from/to the metal center or from/to an external source. Given this wide variety of ligands

that are included under the label non-innocent, we will constraint the subsequent discussion to the following definition: non-innocent ligands are those ligands that are actively involved in a reaction through the addition or subtraction of "reactive force" to/from the metal center to which they are anchored, and that in the same process undergo some kind of transformation.

Metal-ligand cooperation (MLC) is a rapidly increasing field on homogeneous catalysis. In 2011, Crabtree classified cooperative ligands in five categories depending on their functionality/performance:[8]

1. Proton-responsive ligands; those with the ability to accept or donate protons.
2. Hydrogen-bonding ligands; those affecting the system through partial proton transfer or aiding substrate orientation via hydrogen bonding.
3. Electron-responsive ligands, also known as redox-active ligands; those capable of gaining or losing electrons.
4. Photo-responsive ligands; those capable of undergoing property changes after irradiation.
5. Ligands with molecular recognition functionality.

In the rest of this Introduction we will focus on proton-responsive ligands, redox-active ligands and photo-responsive ligands. They will be the subjects of the main chapters of this thesis. Redox-active and photo-responsive ligands will be discussed in the same subsection because they are closely related.

1.2 Proton-responsive ligands

Proton-responsive ligands are those that participate actively in bond breaking and forming steps by the acceptance or donation of a proton. The responsible of this reactivity are those atoms (normally N or O) that act as an internal base in the presence of protons. The first example of this reactivity was introduced by Shvo and co-workers, in 1985.[9,10]

In their original work, a cyclopentadienone-ruthenium complex, known as Shvo's catalyst, was able to activate dihydrogen through metal-ligand cooperativity (MLC). During this process, the dihydrogen molecule is broken heterolytically to form two new bonds, M—hydride and O—proton. The process is redox-neutral from the point of view of the metal, *i.e.*, the formal oxidation state on the ruthenium atom does not change. Instead, it is the cyclopentadienone ligand which undergoes a charge change from anionic to neutral, after the heterolytically breaking of the H_2 molecule. The complex resulting from the H_2 cleavage was active for the hydrogenation of ketones (Scheme 1.2).

Scheme 1.2 Classical Shvo mechanism for the hydrogenation of ketonic substrates.

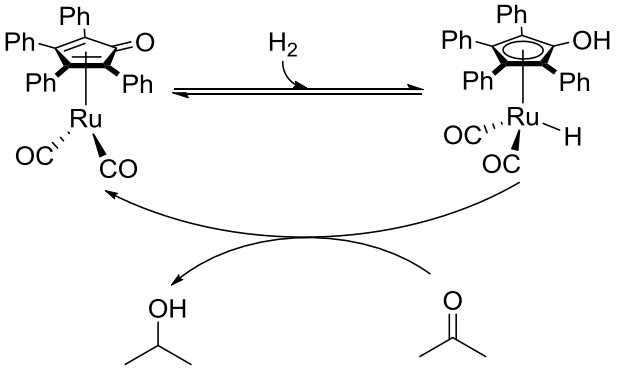

In 1995, an important breakthrough in the asymmetric hydrogenation of ketones was reported by Noyori and co-workers.[11,12,13] Several Ru(II)-diamine complexes were reported to bear an active Ru-hydride bond and an adjacent ligand-based electrophilic proton. The reaction was firstly described to follow a cyclic transition state, where the proton and the hydride are transferred simultaneously *via* an outer-sphere mechanism (Scheme 1.3a). Nevertheless, a recent revisitation of the mechanism governing this reaction catalyzed by the chiral complex *trans*-[$RuCl_2${(S)-binap}{(S,S)-dpen}], showed that the preferred mechanism is stepwise. The ligand stabilizes the transition state for the product formation through a N—H···O bond interaction (Scheme

1.3b).[14] This would change the classification of these ligands from proton-responsive to hydrogen-bonding ligands, according to the criteria explained above. In any case, the activation of the pre-catalysts by H_2 follows the same metal-ligand cooperation mechanism.

Scheme 1.3 a) Non-innocent and b) innocent ligand pathways for the hydrogenation of ketones catalyzed by Noyori's *trans*-[$RuCl_2${(S)-binap}{(S,S)-dpen}] catalyst.

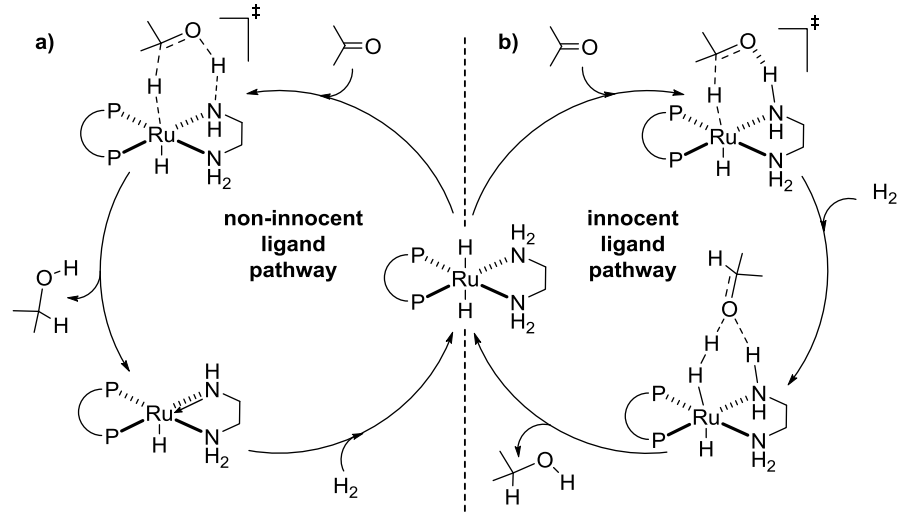

Since Noyori's discovery of metal-ligand cooperation catalysis, many effective bifunctional catalysts have been reported. In this context, tridentate chelating aliphatic ligands of the form PN^HP ($HN(CH_2CH_2PR_2)_2$) have been reported as effective metal-ligand cooperation catalysts for the hydrogenation of many C=O containing substrates as well as for transfer hydrogenation. Some exhaustive reviews have been published recently for this kind of systems [15,16,17] and will not be discussed further in this thesis. It is worth noting however, that during my short research stay in the group of Haijun Jiao, at the Leibniz Institute for Catalysis (LIKAT), we studied with DFT tools the dehydrogenation of methanol with well-defined PNP pincer Mn and Re complexes, in a collaboration with the experimental group of Beller. We found the same mechanism previously reported by Dub *et al*, where

the ligand does not transfer the proton attached on the N atom but helps the stabilization of the transition state for product formation.[18]

In 2006, Milstein and co-workers reported a new mode of metal-ligand cooperation based on aromatization-dearomatization of a PNP pincer system.[19] In contrast to the systems previously reported by Beller, the N atom is part of a lutidine moiety, and this provides different properties to the system. Scheme 1.4 shows the mechanism of the formation of the active species for this kind of complexes. The methylenic position of the ligand backbone in **1** is prone deprotonation in presence of a base, to form the active species **2**. Then, activation of different chemical bonds (Y—H = O—H, N—H, C—H, B—H, Si—H) by MLC, results in the re-aromatization of the ligand and the activation of the substrate, **3**. No formal change in the oxidation state of the metal center occurs during these steps.

Scheme 1.4 Aromatization-dearomatization and bond activation by lutidine-based pincer complex.

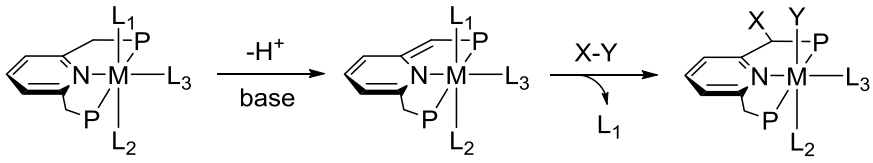

Several transition metal-based complexes bearing this kind of ligand scaffolds have been reported to be efficient in the catalytic activation of chemical bonds. The metals involved include Ru, Fe, Co, Ir, Ni, Pd, Pt, Mn and Re.[20,21,22,23,24] Other modifications of the ligand scaffold, such as substitution of the methylenic group by a NH group or replacement of one PR_2 arm by a nitrogen donor group, have been explored (Scheme 1.5).[25] An exhaustive review focusing on first-row transition metals based on functional pincer ligands has been recently published by Schneider and co-workers.[26] From a computational perspective, Li and Hall reviewed in 2015 all the computed mechanisms

involving pyridine- or acridine-based PNP and PNN pincer ligands following aromatization-dearomatization mechanism.[27]

Scheme 1.5 Selected aliphatic- (left) and lutidine-based (right) pincer ligands.

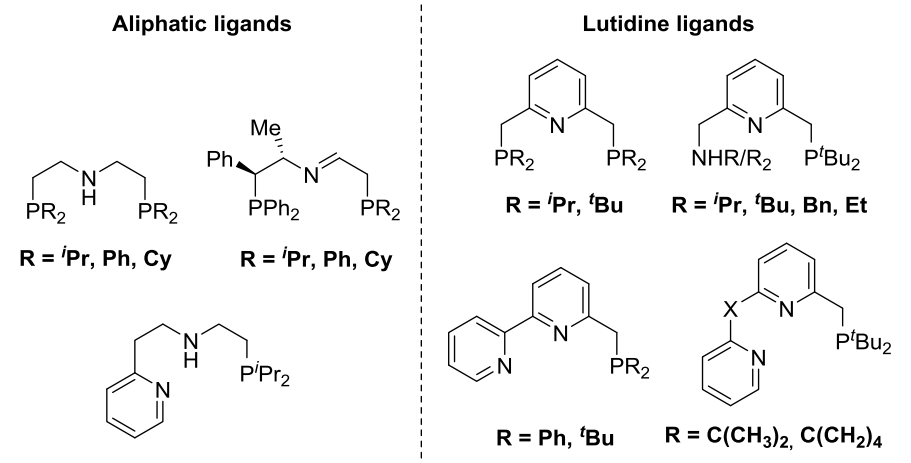

Another family of proton-responsive ligand that are well-established for the C—H activation of different substrates are carboxylate ligands.[28,29,30] The most famous and exploited method for the activation of a C—H bond on a substrate is the direct oxidative addition of this bond to the metal center.[31] This is the mechanism usually operating for late transition metals. This classical methodology has however some limitations. The metal center has to be in a low oxidation state because during the process it will get oxidized by two units.[32] In addition, it needs to have coordinative vacancies to allow the attachment of the incoming groups. Alternative methods for C—H activation can be achieved taking advantage of active ligands.

The electron pairs in ligands or in molecules in the metal coordination sphere can play a role in the activation of σ-bonds by saturated complexes. Some mechanisms using the electrons formally in the metal-ligands bonds (M—X bonds) are σ-bond metathesis (SBM) [33] and σ-complex assisted metathesis (σ-CAM).[34] Other mechanisms use directly lone pairs in ligands; examples of this type are electrophilic

aromatic substitution (S_EAr), base-assisted internal electrophilic substitution (BIES), concerted metalation deprotonation (CMD)[35] and ambiphilic metal ligand activation (AMLA).[36] A recent work by Macgregor and co-workers, suggests that all the latter mechanisms are essentially the same, especially when a carboxylate ligand is acting as internal base.[37] Hence, we will only introduce the CMD mechanism; a discussion of the similarities or differences between the proposed mechanism is out of the scope of this thesis.

Scheme 1.6 Common C-H activation mechanisms by transition metals.

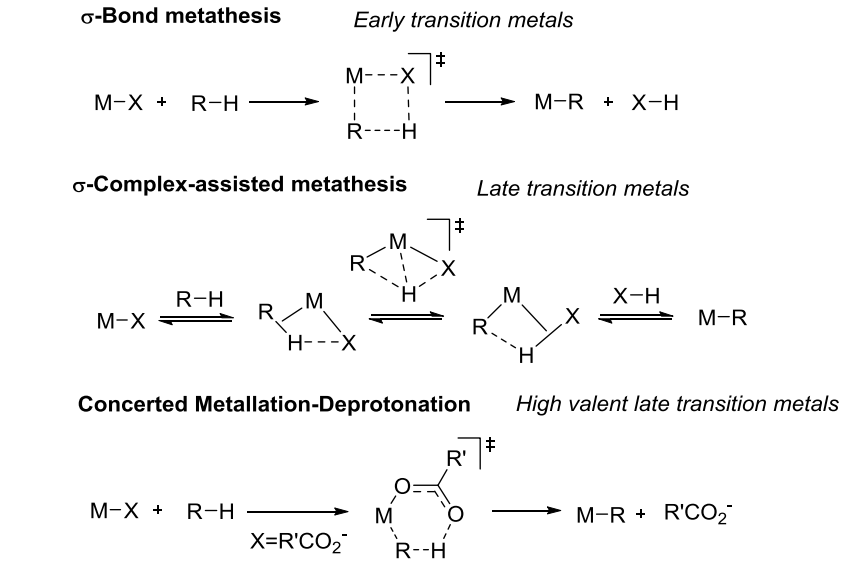

The σ-bond metathesis consists in the addition of a C—H bond to an activated M—X (X=halide, C or H) bond. This mechanism occurs via a concerted four-membered cyclic transition state, and is typically found on early transition metals, where oxidative addition is not a viable pathway due to the inaccessibility of higher oxidation states. On a similar way, σ-CAM occurs also via a four-membered concerted transition state. This mechanism involves discrete sigma complexes as intermediates before and after the transition state and the metal interacts with the transferred moiety during the event.[38] Concerted metalation-

deprotonation mechanism (CMD) is the most common pathway for a C—H activation in the presence of carboxylate ligands. This mechanism involves a six-membered ring transition state, where the C—H bond cleaves simultaneously to the M—C and O—H bond formation (Scheme 1.6).[39,40,41] A comprehensive review including all modes of C—H activation has been recently published by Bai and Lan.[42]

1.3 Electron- and photo-responsive ligands

Redox non-innocent ligands are those ligands capable of undergoing a change of properties through the gain or loss of one or more electrons.[43,44] These ligands have a unique ability to change the reactivity of the metal where they are attached through control of the release or gain of electrons. The complexes bearing these ligands can adopt different electronic structures. This has been key to achieve new types of reactivity.

Four principal strategies [45] can be observed in reactions involving redox active ligands:

(1) The ligand acts as an electronic mediator. It modifies and controls the Lewis acidity of the metal center by ligand reduction or oxidation. This directly affects the substrate affinity of the metal as well as the subsequent follow-up reaction steps (Scheme 1.7a).[46]
(2) The ligand acts as an electron-reservoir. It allows the metal to store or accept electron density to/from the ligand. This allows the avoidance of uncommon oxidation states on the metal (Scheme 1.7b).[47]
(3) The ligand is cooperatively active. It generates reactive ligand radicals during a catalytic cycle. The ligands following this strategy actively participate in the bond formation and breaking steps (Scheme 1.7c).[48]

(4) The ligand is directly involved in radical-type activation or chemical modifications of the substrate. This requires substrates prone to act as a redox non-innocent ligands themselves (Scheme 1.7d).[49]

Scheme 1.7 Different strategies using redox non-innocent ligands in catalysis.

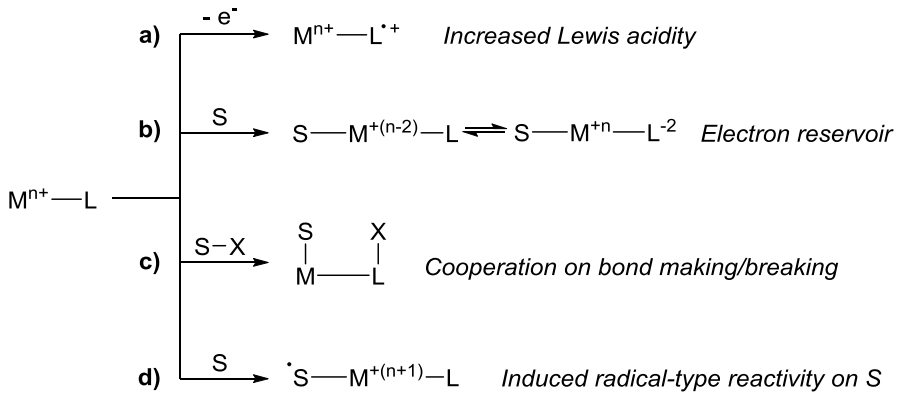

This can be summarized by saying that redox non-innocent ligands can participate in the reaction process by accepting/releasing electrons (strategies 1 and 2) or by forming/breaking chemical bonds of the substrate (strategies 3 and 4). A recent paper by van der Vlugt summarizes these reactivity modes as well as presents some catalytic examples.[50]

Photo-responsive ligands are extremely related to electron-responsive ligands. Their defining characteristic is the change of properties upon irradiation. Modern photocatalysis exploits the unique reactivity of metal-based complexes (photosensitizer) bearing ligands with high delocalized aromatic systems and low-lying π* orbitals. The most used ligand for this purpose is 2,2'-bipyridine (bpy). The mechanism behind this special reactivity is commonly attributed to a metal-to-ligand charge transfer (MLCT) promoted by the irradiation at a determined wavelength. This transition excites the whole complex to an excited singlet spin state where the metal is oxidized and the ligand is reduced by one unit each. From this point, multiple pathways are possible, commonly resumed in a Jablonski diagram (Figure 1.1).[51]

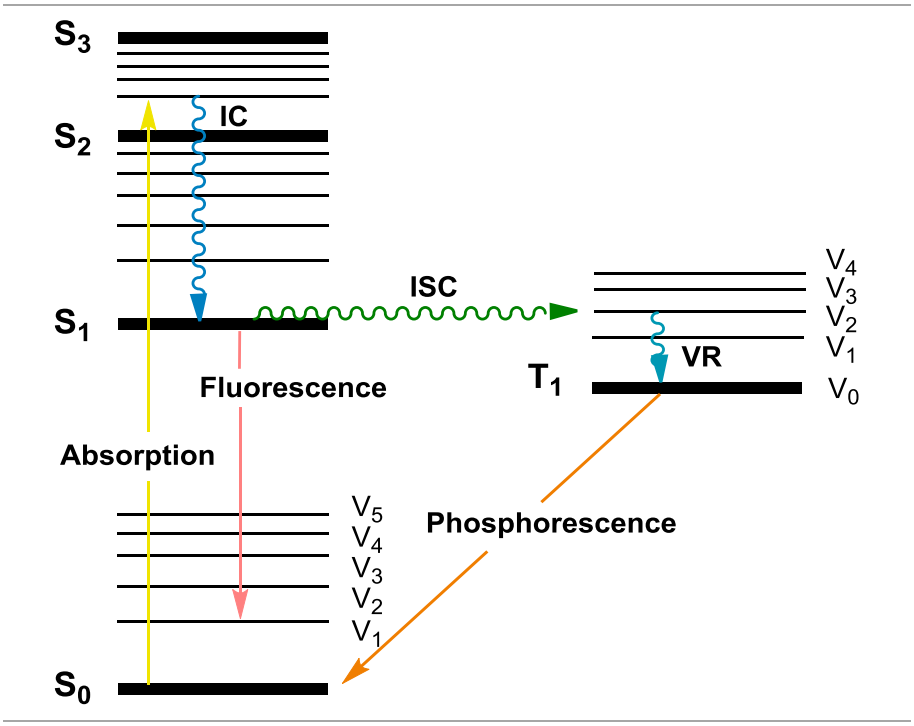

Figure 1.1 Jablonski diagram.

The first transition in a Jablonski diagram is the absorption of a photon from the singlet ground state $\mathbf{S_0}$ to a higher energy excited state with the same multiplicity $\mathbf{S_n}$. The identity of the $\mathbf{S_n}$ state is controlled by the photon energy, and by the overlap between the orbitals in a way that can be computed. The $\mathbf{S_n}$ excited molecule usually relaxes then *via* vibrational relaxation (VR), a non-radiative process, to a lower energy excited state, for instance $\mathbf{S_1}$. During vibrational relaxation, the excess energy is released away to other vibrational modes as kinetic energy, in a process that can be viewed as a fast relaxation of the molecule within the same electronic level. The excited state may also relax to other states of similar energy *via* intersystem crossing (ISC). Intersystem crossing may lead the system to a different multiplicity, for instance to the $\mathbf{T_1}$ state. In order for the molecule to be photochemically active, it has to stay some time in the excited state. Photochemical reactivity is always competing

with relaxation to the ground state S_0, which may occur through fluorescence ($\mathbf{S_1}$ to $\mathbf{S_0}$) or through phosphorescence ($\mathbf{T_1}$ to $\mathbf{S_0}$).

The photochemical process in most transition metal complexes takes place through a metal-ligand charge transfer excitation (MLCT). The MLCT process has an important connection to the LUMO-HOMO gap of the given complex. Each metal-based complex has its intrinsic electrochemical potential.[52] The selected photosensitizer for a given reaction has to be powerful enough to one-electron reduce or oxidize selectively the desired substrate, but also weak enough to preclude reaction with other species in the medium. This is the reason that so many photosensitizers have been developed, with different redox potentials. In addition, the redox potential of the metal-based photosensitizers can be tuned by modifying the substituents of the ligands, reducing the necessity for full replacement.[53] A more detailed introduction to the field of photochemistry will be presented in Chapter 5.

1.4 Objectives

Metal-ligand cooperation is an attractive field of research for many homogeneous computational groups. This is probably owing to the associated intrinsically complex reactivity. In addition, metal-ligand cooperation appeals for a more sustainable chemistry and the rationalization of the mechanism governing these transformations would provide more insights for a rational design of new catalysts.[54] The synergistic activity of both the metal and the ligand generates often different mechanisms, which require proper characterization.

The goal of this thesis is to improve our understanding on the mechanism of metal-ligand cooperation (MLC). We intend to reach this goal through standard Density Functional Theory (DFT) calculations on a series of specific processes, in many cases in collaboration with experimental groups.

The specific objectives we intend to achieve are the following.

Rationalization of the active role of the acetate ligand in the transformation of a Ru alkenyl complex to its alkynyl derivative upon addition of phenylacetylene. This work is a collaboration with the group of Prof. Sola (Universidad de Zaragoza).

Elucidation of the complex electronic structure of different iron species such as $[Fe^{II}(N_2S_3)]^0$ and its redox partners with the goal of applying this knowledge to the mechanistic understanding of their role as catalysts in the hydroboration of aldehydes. This work is a collaboration with the group of Prof. Baker (University of Ottawa).

Characterization of the mechanism for the photoactivated nickel-catalyzed synthesis of indoline products. The role of the ruthenium photosensitizer will be analysed and the origin of the high regioselectivity explored.

1.5 References

[1] Crabtree, R. H. *The Organometallic Chemistry of the Transition Metals*, 5th Edition, Wiley & Sons, Hoboken, NJ, **2009**.

[2] Ikariya, T.; Masakatsu, S. *Topics in Organometallic Chemistry, Bifunctional Molecular Catalysis*, Vol. 37, Springer-Verlag: Berlin Heidelberg, Germany, **2011**.

[3] van der Vlugt, J. I. *Eur. J. Inorg. Chem.* **2012**, 2012, 363-375.

[4] Gordon, J. C.; Kubas, G. J *Organometallics* **2010**, 29, 4682-4701.

[5] Dubois, M. R.; Dubois, D. L. *Acc. Chem. Res.* **2009**, 42, 1974-1982.

[6] Wodrich, M. D.; Hu, X. *Nat. Rev. Chem.* **2017**, 2, 0099.

[7] Camara, J. M.; Rauchfuss, T. B. *Nat. Chem.* **2012**, 4, 26-30.

[8] Crabtree, R. H. *New J. Chem.* **2011**, 35, 18-23.

[9] Blum, Y.; Czarkie, D.; Rahamim, Y.; Shvo, Y. *Organometallics* **1985**, 4, 1459-1461.

[10] Shvo, Y.; Czarkie, D.; Rahamim, Y.; Chodosh, D. F. *J. Am. Chem. Soc.* **1986**, 108, 7400-7402.

[11] Hashiguchi, S.; Fujii, A.; Takehara, J.; Ikariya, T.; Noyori, R. *J. Am. Chem. Soc.* **1995**, 117, 7562-7563.

[12] Yamakawa, M.; Ito, H.; Noyori, R. *J. Am. Chem. Soc.* **2000**, 122, 1466-1478.

[13] Ohkuma, T.; Muñiz, K.; Sandoval, C. A.; Noyori, R. *Philos. Trans. A Math. Phys. Eng. Sci.* **2005**, 363, 901-912.

[14] Dub, P. A.; Henson, N. J.; Martin, R. L.; Gordon, J. C. *J. Am. Chem. Soc.* **2014**, 136, 3505-3521.

[15] Bornschein, C.; Werkmeister, S.; Wendt, B.; Jiao, H.; Alberico, E.; Baumann, W.; Junge, H.; Junge K.; Beller, M. *Nat. Commun.* **2014**, 5, 4111.

[16] Junge, K.; Wendt, B.; Jiao H.; Beller, M. *ChemCatChem* **2014**, 6, 2810-2814.

[17] Chakraborty, S.; Blacque, O.; Fox T.; Berke, H. *Chem. - Asian J.* **2014**, 9, 328-337.

[18] Wei, Z.; de Aguirre, A.; Junge, K.; Beller, M.; Jiao, H. *Catal. Sci. Technol.* **2018**, 8, 3649-3665.

[19] Ben-Ari, E.; Leitus, G.; Shimon, L. J. W.; Milstein, D. *J. Am. Chem. Soc.* **2006**, 128, 15390-15391.

[20] van der Vlugt, J. I.; Lutz, M.; Pidko, E. A.; Vogt, D.; Spek, A. L. *Dalton Trans.* **2009**, 1016-1023.

[21] van der Vlugt, J. I.; Reek, J. N. H. *Angew. Chem. Int. Ed.* **2009**, 48, 8832-8846.

[22] Guananathan, C.; Milstein, D. *Science* **2013**, 341, 1229712.

[23] Zhang, L.; Zuo, Z.; Leng, X.; Huang, Z. *Angew. Chem. Int. Ed.* **2014**, 53, 2696-2700.

[24] T. Zell, D. Milstein, *Acc. Chem. Res.* **2015**, 48, 1979-1994.

[25] Khusnutdinova, J. R.; Milstein, D. *Angew. Chem. Int. Ed.* **2015**, 54, 12236-12273.

[26] Alig, L.; Fritz, M.; Schneider, S. *Chem. Rev.* **2019**, 119, 2681-2751.

[27] Li, H.; Hall, M. B. *ACS Catal.* **2015**, 5, 1895-1913.

[28] Ackermann, L. *Chem. Rev.* **2011**, 111, 1315-1345.

[29] Ackermann, L. *Acc. Chem. Res.* **2014**, 47, 281-295.

[30] Davies, D. L.; Macgregor, S. A.; McMullin, C. L. *Chem. Rev.* **2017**, 117, 8649-8709.

[31] Gandeepan, P.; Müller, T.; Zell, D.; Cera, G.; Warratz, S.; Ackermann, L. *Chem. Rev.* **2019**, 119, 2192-2452.

[32] Jones, W. D. *Inorg. Chem.* **2005**, *44*, 4475-4484.

[33] Waterman, R. *Organometallics* **2013**, 32, 7249-7263.

[34] Perutz, R. N.; Sabo-Etienne S. *Angew. Chem. Int. Ed.* **2007**, 46, 2578-2592.

[35] Gorelsky, S. I.; Lapointe, D.; Fagonu, K. *J. Am. Chem. Soc.* **2008**, 130, 10848-10849.

[36] Sajjad, M. A.; Harrison, J. A.; Nielson, A. J.; Schwerdtfeger, P. *Organometallics* **2017**, 36, 4231-4237.

[37] Alharis, R. A.; McMullin, C. L.; Davies, D. L.; Singh, K. Macgregor, S. A. *J. Am. Chem. Soc.* **2019**, 141, 8896-8906.

[38] Li, Y.; He, G.; Kantchev, E. A. B. *Phys. Chem. Chem. Phys.* **2014**, 16, 24250-24255.

[39] Lapointe, D.; Fagnou, K. *Chem. Lett.* **2010**, *39*, 1118-1126.

[40] García-Cuadrado, D.; Braga, A. A. C.; Maseras, F.; Echavarren, A. M. *J. Am. Chem. Soc.* **2006**, *128*, 1066-1067.

[41] García-Cuadrado, D.; de Mendoza, P.; Braga, A. A. C.; Maseras, F.; Echavarren, A. M. *J. Am. Chem. Soc.* **2007**, *129*, 6880-6886.

[42] Shan, C.; Zhu, L.; Qu, L.-B.; Bai, R.; Lan, Y. *Chem. Soc. Rev.* **2018**, 47, 7552-7576.

[43] Kaim, W. *Coord. Chem. Rev.* **1987**, 76, 187-235.

[44] Kaim. W.; Schwederski, B. *Coord. Chem. Rev.* **2012**, 254, 1580-1588.

[45] Lyaskovskyy, V.; de Bruin, B. *ACS Catal.* **2012**, 2, 270-279.

[46] a) Ringenberg, M. R.; Kokatam, S. L.; Heiden, Z. M.; Rauchfuss, T. B. *J. Am. Chem. Soc.* **2008**, 130, 788-789. b) Paretzki, A.; Bubrin, M.; Fiedler, J.; Záliš, S.; Kaim, W. *Chem. Eur. J.* **2014**, 20, 5414-5422.

[47] Curcio, M.; Pankhurst, J. R.; Sproules, S.; Mignard, D.; Love, J. B. *Angew. Chem. Int. Ed.* **2017**, 56, 7939-7943.

[48] Ouch, K.; Mashuta, M. S.; Grapperhaus, C. A. *Inorg. Chem.* **2011**, 50, 9904-9914.

[49] a) Wang, Y.; Wen, X.; Cui, X.; Zhang, X. P. *J. Am. Chem. Soc.* **2018**, 140, 4792-4796. b) Kuijpers, P. F.; van der Vlugt, J. I.; Schneider, S.; de Bruin, B. *Chem. Eur. J.* **2017**, 23, 13819-13829.

[50] van der Vlugt, J. I. *Chem. Eur. J.* **2019**, 25, 2651-2662.

[51] Frackowiak, D. J. *Photochem. Photobiol. B* **1988**, 2, 399-402.

[52] DiRocco, D. "Electrochemical Series of Photocatalysts and Common Organic Compounds", **2014**, (Mercks).

[53] Arias-Rotondo, D. M.; McCusker, J. K. *Chem. Soc. Rev.* **2016**, 45, 5803-5820.

[54] Dub, P. A.; Matsunami, A.; Kuwata, S.; Kayaki, Y. *J. Am. Chem. Soc.* **2019**, 141, 2661-2677.

Chapter 2

Theoretical Background

Dealing with newly developed transformations, for example photoactivated reactions, compels the computational chemistry to use non frequent techniques. In this chapter we will discuss the less-common methodologies applied during this thesis. In contrast, although density functional theory is used profusely in the thesis, we will not present its main principles because they are already summarized in many other thesis and books on the literature.[1] Terms like dispersion interactions [2,3] or implicit solvation models [4] will not be discussed because of the same reason, although they were used during the calculations of this thesis.

2.1 Theoretical Methods

Open-shell systems with DFT

Usually in reactions involving single electron transfer events, species and intermediates with unpaired electrons can be found during the reaction

pathways. DFT methods are not multiconfigurational: only one Slater determinant is used. Therefore, these electronic states, where not all electrons of opposite spin are paired (open-shell electronic systems) or with unpaired number of electrons (*e.g.* triplet spin state) are not accurately described. A proper description of these electronic states can be achieved using high level multiconfigurational methods.

Yet, realistic energies can be obtained with the unrestricted Kohn-sham (UKS) formalism. Unrestricted stands for a major flexibility of the α and β orbitals, since they are not forced to be the identical. This generates a formally incorrect spin description of the electronic structure for singlet states, as the resulting KS orbitals obtained from an unrestricted calculation are not eigenfunctions of the spin operator. The orbitals obtained with this approach do not constrain the spin symmetry and hence, the solution leads to a broken symmetry spin states which are usually contaminated by higher multiplicity spin states. However, this is the most simple way to deal with open-shell singlets within DFT, and provides reasonable descriptions in many cases. A comprehensive review was published a few years ago by Jacob and Reiher on the basis of the broken-symmetry approach.[5]

Yamaguchi spin correction

When dealing with open-shells molecules, for example singlet biradicaloids (*i.e.*, open-shell singlet molecules) the electronic state can be contaminated with higher spin states. As explained in the previous section, this occurs when an unrestricted form of the orbital description is used, so the α and β spin-orbitals are not forced to be the same. The amount of contamination can be tracked by analyzing the expectation value of operator S^2, which is provided by most computational chemistry codes. For instance, the expected S^2 value for a doublet spin state is 0.75. Nevertheless, when working with complex electronic structures, the calculated value could differ severely from that number. This is in-

dicative of the apparition of extra open shells on the electronic structure of a given doublet (S=½) molecule. This spin contamination is directly reflected in the calculated energy. Therefore, a correction to this energy is necessary to obtain the "real" energy for the pure state.

Yamaguchi *et al.*[6,7] developed a methodology to account for this spin contamination and correct the spin-contaminated energies, $E_{corr.}$. The Yamaguchi spin correction formula for a given S spin is shown in equation (1):

$$E_{corr.} = \frac{E_{cont.} - a_1 E_{S+1}}{1 - a_1} \quad (1)$$

where E_{S+1} is the energy for the first subsequent spin state $(S+1)$; $E_{cont.}$ is the spin-contaminated energy and a_1 is the fraction of the spin contamination, which can be obtained following equation (2):

$$a_1 = \frac{\langle S^2 \rangle_{cont.} - S(S+1)}{\langle S^2 \rangle_{S+1} - S(S+1)} \quad (2)$$

where $\langle S^2 \rangle_{cont.}$ and $\langle S^2 \rangle_{S+1}$ are the S^2 spin operators of the contaminated and the subsequent unpaired spin states $(S+1)$, respectively. This equation is only valid if the successive spin state $(S+1)$ is not contaminated (*i.e.* the contaminated energy for an open-shell singlet can be corrected with equation (1) and (2) if the triplet spin state is a pure state). If this is not the case, the next higher spin states must also be corrected with a different set of equations (3-6).[8] The labels of each term in equations (3-6) follow the same legend as for equation (1-2) and thus, will not be explained in detail.

$$E_{corr.} = \frac{E_{cont.} - a_2 E_{(corr,S+1)}}{1 - a_2} \quad (3)$$

$$a_2 = \frac{\langle S^2 \rangle_{cont.} - S(S+1)}{(S+1)(S+2) - S(S+1)} \quad (4)$$

$$E_{(corr,S+1)} = \frac{E_{(cont.S+1)} - a_3 E_{S+2}}{1 - a_3} \quad (5)$$

$$a_3 = \frac{\langle S^2 \rangle_{S+1} - (S+1)(S+2)}{\langle S^2 \rangle_{S+2} - (S+1)(S+2)} \quad (6)$$

Accordingly, the energy for a pure state when the next higher spin states $(S+1)$ is also contaminated can be corrected considering the pure energy of the $(S+2)$ state. This methodology have been demonstrated to reproduce experimental results upon correction of the spin-contaminated energies.[9,10]

Minimum Energy Crossing Point

A common pathway in reactions involving excited electronic states is its conversion to a more stable spin state. This mechanism is known as intersystem crossing (ISC) and can be defined as a nonradiative transition between two electronic states of different multiplicity.[11] This type of processes have been found to be crucial in many areas of chemistry. For instance, in photochemistry, the ISC between the photoexcited singlet and the triplet excited state governs the decay rate and the lifetime of the triplet state.[12,13,14] Intersystem crossing is also found on thermally activated reactions, *i.e.*, the ISC is not exclusive of the photogenerated excited states.[15,16]

Each electronic spin state has its corresponding *n*-dimensional potential energy surface (PES). The intersection of the two energy surfaces would generate a seam of *n*-1 dimensions. The lowest energy point on the *n*-1-dimensional surface is known as Minimum Energy Crossing Point (MECP) and can be seen as an analog of a transition state in reactions involving more than one electronic state (Figure 2.1).

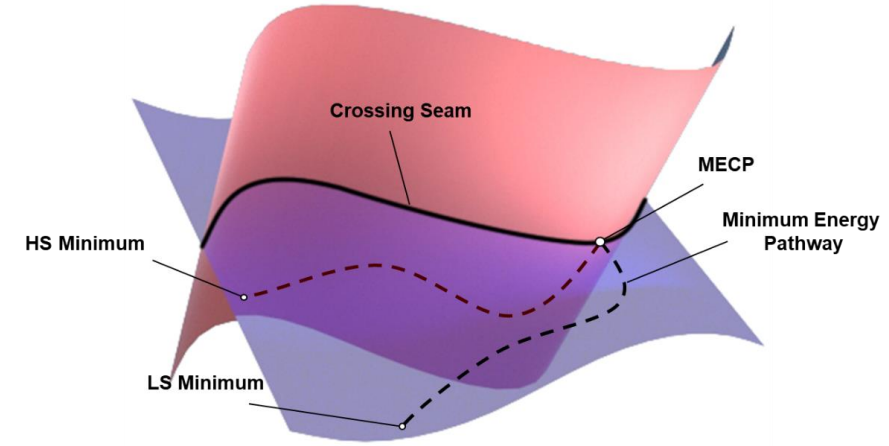

Figure 2.1 Three-dimensional representation of the intersection between two potential energy surfaces (PESs) with the crossing seam (solid black line) and MECP labeled. The dashed line traces the minimum energy path through the MECP from the high-spin (HS) to low-spin (LS) minimum.

Formally, spin transitions are forbidden because of the orthogonality of the spin part of the wavefunction. However, intersystem crossing can occur thanks to the relativistic effects such as spin-orbit coupling (SOC), or through collisions with solvent molecules. The strength of the spin-orbit coupling in the vicinity of areas where the two PESs cross, determines the probability and the rate of the ISC. As the spin-orbit coupling is a relativistic property, it is stronger on heavier atoms and weaker in light atoms.

In the work presented in this thesis (plus also for all the works carried out during the doctorate program) we used the MECP to estimate the energy barrier of the spin-transitions. The methodology chosen to compute it was firstly introduced by Harvey and co-workers [17] which is a variation of the algorithm previously reported by Schlegel and co-workers.[18] We will not enter here on the explanation on the technical features of this methodology, which can be executed in a reasonable simple way through a code freely provided by Harvey to be applied together with the Gaussian package. A thorough review has been

published recently by Varganov and co-workers on the basis of intersystem crossing.[19]

Marcus theory

Many photochemical processes run through single electron transfer (SET) steps. This reactivity is complementary to the more classical two-electrons transfers.[20] Thus, novel and extraordinary transformations have been developed in the last decades following this approach.[21,22]

From a computational point of view, we must differentiate between two possible pathways for the single electron transfer events, the inner and outer-sphere mechanism. The first scenario needs a transitory linkage between the redox centers to allow the electron "jumping" from one to another. In addition, this process can be described with classical transition state theory.[23,24,25] Conversely, in the outer-sphere scenario, the two redox centers are not connected between them and the electron "hops" through space from one redox partner to the other. A clear example of an outer-sphere SET mechanism is the reduction or oxidation of a given species by means of a photoredox catalysts, which has been demonstrated as cornerstone of recent developments in photocatalysis.[26]

A brilliant approach to address these outer-sphere electron transfer events was developed by Rudolph Marcus in the 1950s.[27,28] By applying this methodology, the activation barrier of an outer-sphere SET step between two redox partners can be estimated. Although the theory was developed many decades ago, its application to transition metal catalyzed reactions is still scarce. Marcus theory states that the activation barrier for an outer-sphere SET step between two redox partners can be estimated as the crossing point between the reactants and products potential energy wells. In contrast to transition state theory, these potential energy wells are not only associated to the structure rearrangement of the redox partners but also with the changes on the solvation cage sur-

rounding each complex. The barrier is then estimated by considering the crossing between parabolic curves associated with the energies of both reactants and products.

The estimated activation barrier calculated with the Marcus theory has a strong relation with the thermodynamics of the reaction. In general, the more exergonic the reaction, the lower the barrier for the electron transfer step. If the intersection point between the two potential energy wells is at the equilibrium coordinate of the reactant surface (green line, Figure 2.2), the reactions is barrierless (*i.e.*, no thermal activation is necessary). When the intersection point between the product and reactants wells is at some point previous to the equilibrium coordinate of the reactants, the activation barrier for the SET process increases, since we are in the so-called Marcus inverted region (purple line, Figure 2.2). This may happen when a given reactions is extremely exergonic. Figure 2.2 shows the three possible scenarios proposed by Marcus theory.

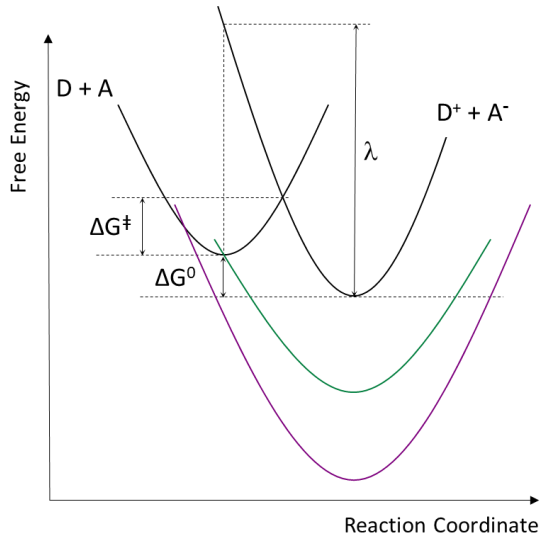

Figure 2.2 Schematic representation of the three possible scenarios in Marcus theory. Black line = common reaction. Green line = barrierless reaction. Purple line = Marcus inverted region.

To calculate the energy barrier $\Delta G^{\ddagger}$, we follow equation (7). ΔG^{0} is the free energy difference between reactants and products, *i.e.,* the standard free energy of the reaction of the SET step. λ is the reorganization parameter including all the nuclei and solvent molecules involved in the SET step. The reorganization parameter can be separated in two components: λ_N and λ_S; each one accounts for the nuclear and the solvent rearrangement, respectively.

$$\Delta G^{\ddagger} = \frac{(\lambda + \Delta G^{0})^{2}}{4\lambda} \tag{7}$$

The nuclear reorganization parameter λ_N is obtained by calculating the energy difference between the reactants and products structures of each species, in gas phase. This term displays the energy required to distort the equilibrium structure to achieve the proper geometry enabling the electron transfer event. This is numerically shown in equation (8), where D and A are the donor and acceptor redox species, superscripts I and F refer to the initial and final structure, respectively; and α and β represents the electronic state of each complex at the equilibrium geometry.

$$\lambda_N = \mathrm{D^F}\alpha + \mathrm{A^F}\beta - \mathrm{D^I}\alpha - \mathrm{A^I}\beta \tag{8}$$

The solvent reorganization parameter λ_S can be calculated using the continuum solvent model. This term relates the energy input necessary to reorganize the solvent cage when the equilibrium geometry of the redox partners is distorted to facilitate the electron transfer. The formula to calculate λ_S is shown in equation (9). In this case, we maintain the same geometry for both species ($\mathrm{D^I}$ and $\mathrm{A^I}$), and we compare the energy of the solvation cage between the final and the initial electronic states([α]−[β] and [δ]−[ω], respectively) for each species involved in the SET step. This methodology to compute the solvent parameter has been previously demonstrated to reproduce experimental results.[29,30]

Marcus theory also states that the solvent rearrangement is usually the larger parameter, as it involves the reorganization of the solvent molecules surrounding each redox partner.

$$\lambda_S = D^I[\delta] + A^I[\omega] - D^I[\alpha] - A^I[\beta] \quad (9)$$

It is worth mentioning that in this simple approach to estimate the activation barrier for an outer-sphere SET step there is no information on the actual distance between the donor and the acceptor. It is assumed to be quite long, as otherwise the inner-sphere mechanism would likely dominate.[31]

Case example of the Marcus theory

Recently, we [32,33] and others [34] groups have successfully applied this methodology to estimate the activation barriers for the outer-sphere SET step in different reactions. Particularly, we applied the Marcus theory to reconsider the electron transfer steps in a well-defined homogeneous Cu-catalysts for the water oxidation reaction (Figure 2.3).[35] The results of this investigation will be presented in what follows.

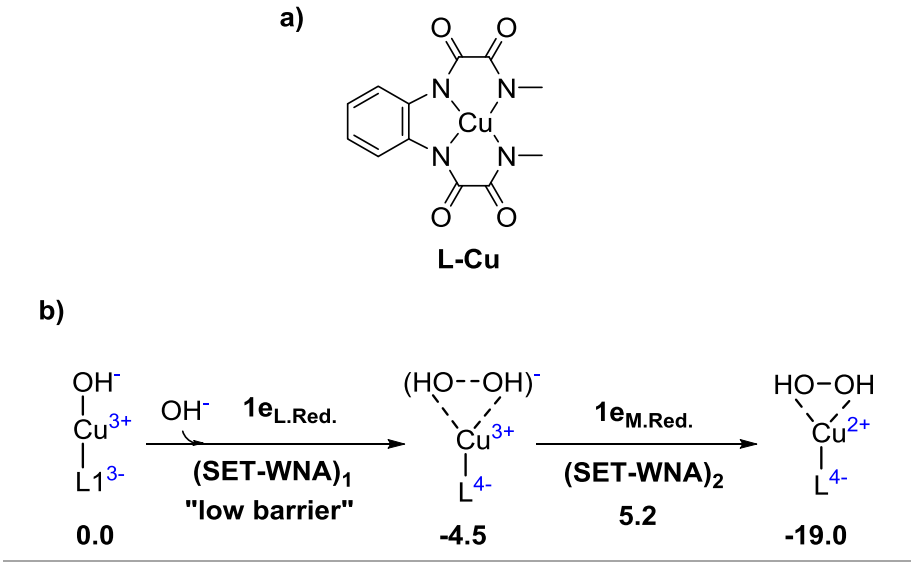

Figure 2.3 a) Cu catalysts for the water oxidation reaction studied with Marcus theory. b) Single-electron transfer-water nucleophilic attack (SET-WNA) mechanism previously reported by our group.[36] Black numbers correspond to free energies in kcal·mol^{-1}.

For the first electron transfer step, two models were considered. In the first model (Figure 2.4a), the electron transfer departs from an **OH$^-$** moiety (donor) to complex **1 (D)** (acceptor). The associated activation barrier for the outer-sphere SET was found at 23.0 kcal·mol^{-1}, **SET 1-2**. The products generated in this step would consist of a radical ·OH moiety and the one-electron reduced complex **2 (S)**, in the singlet spin state. This reduced intermediate is found at 8.3 kcal·mol^{-1} from **1 (D)**. Finally, intermediate **2 (S)** would evolve to its triplet spin state via **MECP 2-3 (S-T)** in a barrierless step. Intermediate **3 (T)** was found 3.2 kcal·mol^{-1} below the singlet state.

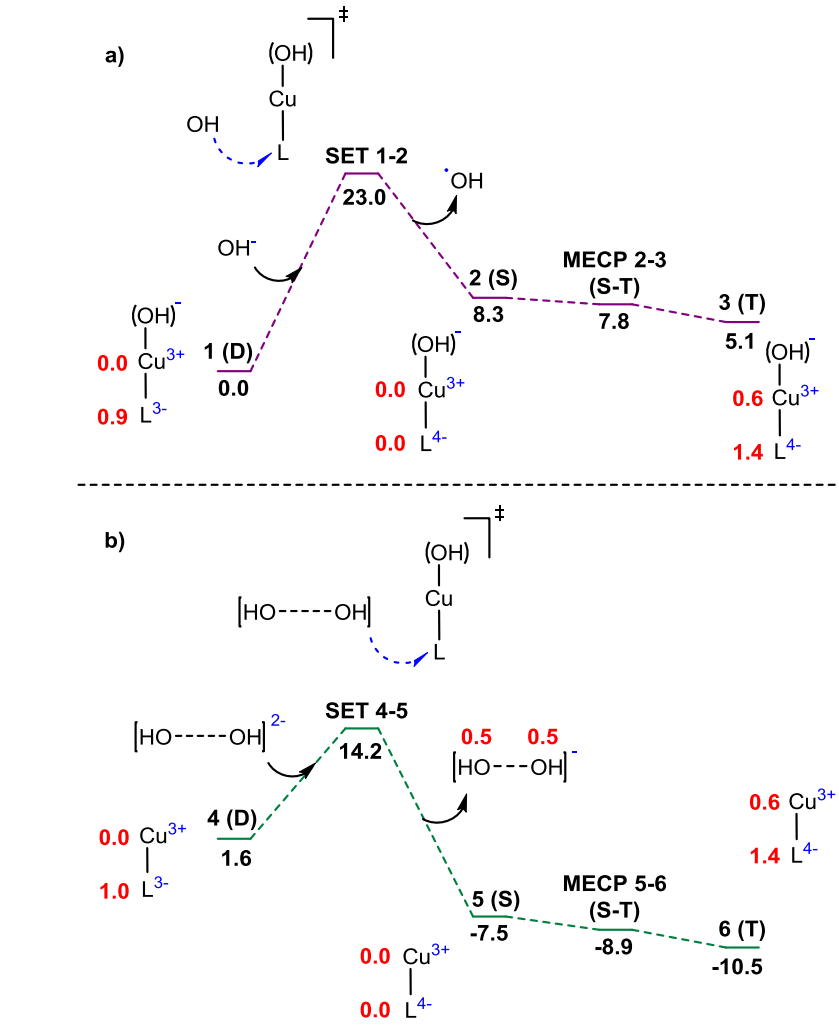

Figure 2.4 a) Model A for the study of the outer-sphere SET from a OH^- moiety to complex **1** applying Marcus theory. b) Model B for the study of the outer-SET from a cluster of two OH^- molecules to complex **4**. Energies are free energies in kcal·mol^{-1}. Red numbers correspond to the spin population. (D), (S) and (T) correspond to the doublet, singlet and triplet, respectively, multiplicity of each complex.

The second model that we envisaged involves the electron transfer from a cluster of two OH^- groups to complex **4 (D)** (Figure 2.4b). The OH cluster is generated after the release of the hydroxyl ligand from the complex, with a low free energy cost of 1.6 kcal·mol^{-1}. The estimated activation barrier for this model is 12.6 kcal·mol^{-1}, **SET 4-5**. Again, after

the electron transfer step, the system evolves to the triplet spin state through a barrierless step, **MECP 5-6 (S-T)**. The final product **6 (T)** following this model was found at 12.1 kcal·mol^{-1} below the initial reactants.

Interestingly, comparing the results for these two models we can visualize the connection between the thermodynamics of the reaction and the kinetic barrier. Model A is endergonic by 8.3 kcal·mol^{-1}, while model B is exergonic by 9.1 kcal·mol^{-1}. The activation barrier for the outer-sphere SET for both models are 23.0 and 12.6 kcal·mol^{-1}, respectively. These values agree with the expected dependence of the kinetic barrier on the thermodynamics of the reaction. A reduction around ~17.0 kcal·mol^{-1} on the reaction thermodynamics, reduces the activation barrier by *ca.* 10 kcal·mol^{-1}.

The calculated values for nuclei and solvent rearrangement parameters for each model are shown in Table 2.1. As expected, the solvent reorganization terms are much larger than the nuclear reorganization terms.

Table 2.1 Parameters calculated by Marcus theory for each model of the first SET step. Energies in kcal·mol^{-1}.

STEP	λ_S	λ_N	ΔG^0	$\Delta G^{\ddagger}$
SET 1-2	74.4	0.1	8.3	23.0
SET 4-5	61.9	5.4	-9.1	12.6

For the second electron transfer step, only model B was studied because model A would form a double oxidized OH species without chemical sense. The results for model B are depicted in Figure 2.5.

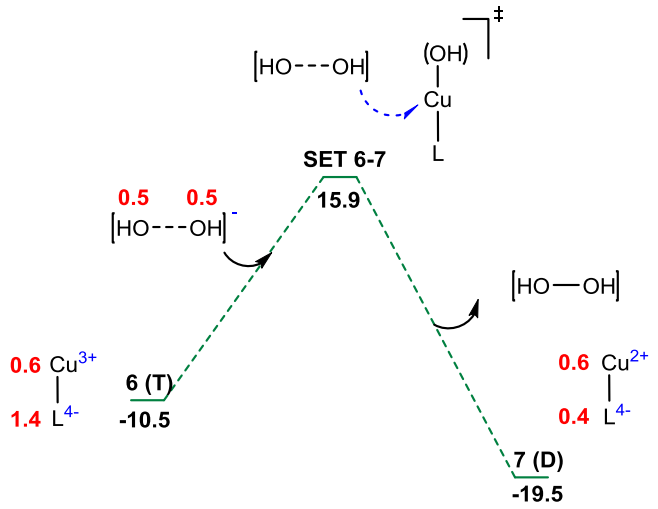

Figure 2.5 Free energy profile for the second SET step on model B applying Marcus theory. Red numbers correspond to the spin population. Energies are free energies in kcal·mol^{-1}.

The activation barrier estimated with the Marcus theory for the second electron transfer step was 26.4 kcal·mol^{-1}, **SET 6-7**, while the overall step was exergonic by 9.0 kcal·mol^{-1}. The energy barrier found is counterintuitive with the thermodynamics of this reaction step. For this reason, we decided to check the calculated parameters for the nuclei and solvent rearrangements in this SET step. The results are summarized in Table 2.2.

Table 2.2 Marcus theory-calculated values for the second SET step. Energies in kcal·mol^{-1}.

STEP	λ_S	λ_N	ΔG^0	$\Delta G^‡$
SET 6-7	62.1	60.9	-9.0	26.4

We can clearly see that the contribution of nuclei reorganization terms is large and almost equal to the solvent reorganization. This high value can be attributed to the energy difference between the [HO···OH] cluster before and after the electron transfer event. Indeed, dividing the nuclear term arising from each redox partner, the contribution coming from the [HO···OH] cluster is 59.7 kcal·mol^{-1}, while for the Cu catalyst

it is only 1.2 kcal·mol^{-1}. This directly affects to the kinetic barrier, making the reaction not feasible through this mechanism. Instead, we found that the reaction takes place through an inner-sphere mechanism, but this is not the topic of this chapter.

To sum up, Marcus theory allows us to compute the energy barrier for an outer-sphere single electron transfer process using simple density functional theory (DFT) tools. This approach permits the estimation of the barrier in a straightforward manner, avoiding the use of more expensive molecular dynamic methodologies.[37,38]

Mössbauer calculations

Mössbauer spectroscopy [39] has become a very powerful characterization tool in different fields of chemistry. It provides useful information on the electronic structure, geometry and magnetic properties, of chemical compounds. Although the Mössbauer effect can be observed for more than 80 elements including tin, gold, or mercury,[40,41] the most extended application of this technique is for the characterization of ^{57}Fe-containing systems. This is due to the large number of iron-bearing systems that have been investigated, for example, in the fields of transition metal and bioinorganic chemistry. [42,43] An attractive attribute of this technique is that it can be used on paramagnetic or diamagnetic molecules, while electron paramagnetic resonance (EPR) or magnetic circular dichroism (MCD) spectroscopy are limited to paramagnetic species.

The two principal parameters from the Mössbauer spectra are the isomer shift (δ) and the quadrupole splitting (ΔE_Q) of a given center. Both terms are strongly related to the total electron density and can provide information on the oxidation state, spin state and coordination number of the metal center. In particular, the isomer shift is known to be directly proportional to the total electron density at the center. On the other hand, the quadrupole splitting is proportional to the electric

field gradient on the metal center and it is relatively easy to calculate with molecular orbital (MO) theory.[44]

The interpretation of the experimental Mössbauer spectra is not straightforward. For this reason, computational chemistry has been shown essential to understand the measured information. Particularly, density functional theory (DFT) calculations have been found to accurately reproduce or predict the Mössbauer parameters for a given structure.[45,46,47] The calculations of the isomer shift are rather problematic due to the dependence of the electron density of the metal center on the DFT methodology used. For this reason, for each DFT method a correlation between the experimental isomer shift and the computed electronic density must be generated. The computed isomer shift is obtained from the introduction of the calculated parameter into an empirically determined equation, generally with the form of a lineal fit, which is specific for a set of computational parameters (functional, basis set, inclusion of solvent effects).[48,49]

In chapter 4 we have calculated the ^{57}Fe Mössbauer parameters for different iron species. Although we have used different DFT methods for both projects, the values for the calculated isomer shift were obtained using the linear equation (10):

$$\delta = \alpha(\rho - C) + \beta \qquad (10)$$

where α, β and C are empirical parameters specific for the DFT methodology used and were extracted from the calibrated results of Neese et. al.[50] The values for ρ in equation (10) and for the quadrupole splitting were directly obtained by using the ORCA (version 4.0) package.[51]

2.2 References

[1] Jensen, F. *Introduction to Computational Chemistry*, 2nd Edition, Wiley & Sons, Ltd.: Chichester, England, **2007**.

[2] Becke, A. D.; Johnson, E. R. *J. Chem. Phys.* **2005**, *123*, 154101.

[3] Grimme, S.; Antony, J.; Ehrlich, S.; Krieg, H. *J. Chem. Phys.* **2010**, *132*, 154104.

[4] Tomasi, J.; Mennucci, B.; Cammi, R. *Chem. Rev.* **2005**, *105*, 2999-3094.

[5] Jacob, C. R.; Reiher, M. *Int. J. Quantum Chem.* **2012**, *112*, 3661-3684.

[6] Yamaguchi, K.; Jensen, F.; Dorigo, A.; Houk, K. N. *Chem. Phys. Lett.* **1988**, 149, 537-542.

[7] Yamanaka, S.; Kawakami, T.; Nagao, H.; Yamaguchi, K. *Chem. Phys. Let.* **1994**, 231, 25-33.

[8] Swart, M.; Guell, M.; Josep M. Luis, J. M.; Sola, M. *J. Phys. Chem. A* **2010**, 114, 7191-7197.

[9] Radoń, M. *Phys.Chem.Chem.Phys.* **2019**, 21, 4854-4870.

[10] Postils, V.; Rodríguez, M.; Sabenya, G.; Conde, A.; Díaz-Requejo, M. M.; Pérez, J. P.; Costas, M.; Solà, M.; Luis, J. M. *ACS Catal.* **2018**, 8, 4313-4322.

[11] Marian, C. M. *WIREs Comput Mol Sci* **2012**, 2, 187-203.

[12] McCusker, J. K.; Vlček A. *Acc. Chem. Res.* **2015**, 48, 1207-1208.

[13] Maeda, S.; Taketsugu, T.; Ohno, K.; Morokuma, K. *J. Am. Chem. Soc.* **2015**, 137, 3433-3445.

[14] Zhang, W.; Alonso-Mori, R.; Bergmann, U.; Bressler, C.; Chollet, M.; Galler, A.; Gawelda, W.; Hadt, R. G.; Hartsock, R. W.; Kroll, T.; Kjær, K. S.; Kubičeck, K.; Lemke, H. T.; Liang, H. W.; Meyer, D. A.; Nielsen, M. M.; Purser, C.; Robinson, J. S.; Solomon, E. I.; Sun, Z.; Sokaras, D.; van Driel T. B.; Vankó, G.; Weng, T. C.; Zhu, D.; Gaffney, K. J. *Nature* **2014**, 509, 345-348.

[15] Harvey, J. N. *WIREs Comput Mol Sci* **2014**, 4, 1–14.

[16] Harvey, J. N.; Poli, R.; Smith, K. M. *Coord. Chem. Res.* **2003**, 238-239, 347-361.

[17] Harvey, J. N.; Aschi, M.; Schwarz, H.; Koch, H. *Theor. Chem. Acc.* **1998**, 99, 95-99.

[18] Bearpark, M. J.; Robb, M. A.; Schlege, H. B. *Chem. Phys. Lett.* **1994**, 223, 269-274.

[19] Lykhin, A. O.; Kaliakin, D. S.; dePolo, G. E.; Kuzubov, A. A.; Varganov, S. A. *Int. J. Quantum Chem.* **2016**, 116, 750-761.

[20] Sameera, W.M.C.; Maseras, F. *WIREs Comput. Mol. Sci.* **2012**, 2, 375-385.

[21] Shaik, S.; Kumar, D.; de Visser, S.P.; Altun, A.; Thiel, W. *Chem. Rev.* **2005**, 105, 2279-2328.

[22] Ye, S.; Geng, C.-Y.; Shaik, S.; Neese, F. *Phys. Chem. Chem. Phys.* **2013**, 15, 8017-8030.

[23] Funes-Ardoiz, I.; Nelson, D. J.; Maseras, F. *Chem. Eur. J.* **2017**, 23, 16728-16733.

[24] Nelson, D. J.; Maseras, F. C*hem. Commun.* **2018**, 54, 10646-10649.

[25] Truhlar, D. G.; Garrett, B. C.; Klippenstein, S. J. *J. Phys. Chem.* **1996**, 100, 12771-12800.

[26] Prier, C. K.; Rankic, D. A.; MacMillan, D. W. C. *Chem. Rev.* **2013**, 113, 5322-5363.

[27] Marcus, R. A. *J. Chem. Phys.* **1956**, *24*, 966-978.

[28] Marcus, R. A. *Angew. Chem. Int. Ed. Engl.* **1993**, 32, 1111-1121.

[29] Moia, D.; Vaissier, V.; Lopez-Duarte, I.; Torres, T.; Nazeeruddin, M. K.; O'Regan, B. C.; Nelson, J.; Barnes, P. R. F. *Chem. Sci.* **2014**, 5, 281-290.

[30] Vaissier, V.; Barnes, P.; Kirkpatrick, J.; Nelson, J. *Phys. Chem. Chem. Phys.* **2013**, 15, 4804-4814.

[31] Kuss-Petermann, M.; Wenger, O. S. *Angew. Chem. Int. Ed.* **2016**, 55, 815-819.

[32] Fernandez-Alvarez, V. M.; Maseras, F. *Org. Biomol. Chem.* **2017**, 15, 8641-8647.

[33] de Aguirre, A.; Funes-Ardoiz, I.; Maseras, F. *Angew. Chem. Int. Ed.* **2019**, 131, 3938-3942.

[34] Qi, Z.-H.; Ma, J. *ACS Catal.* **2018**, 8, 1456-1463.

[35] de Aguirre, A.; Funes-Ardoiz, I.; Maseras, F. *Inorganics* **2019**, 7, 32.

[36] Funes-Ardoiz, I.; Garrido-Barros, P.; Llobet, A.; Maseras, F. *ACS Catal.* **2017**, 7, 1712-1719.

[37] Difley, S.; Wang, L.-P.; Yeganeh, S.; Yost, S. R.; Voorhis, T. V. *Acc. Chem. Res.* **2010**, 43, 995-1004.

[38] Vazquez-Duhalts, R.; Aguila, S. A.; Arrocha, A. A.; Ayala, M. *ChemElectroChem* **2014**, 1, 496-513.

[39] Mössbauer, R. L. *Z. Phys.* **1958**, 151,124-143.

[40] Gütlich, P.; Bill, E.; Trautwein, A. X. *Mössbauer Spectroscopy and Transition Metal Chemistry: Fundamentals and Applications*, Springer-Verlag: Berlin, **2011**.

[41] Shenory, G. K.; Wagner F. E. *Mössbauer Isomer Shifts*, Amsterdam, New York: North-Holland Pub. Co., **1978**.

[42] Martinho, M.; Münck, E. *^{57}Fe Mössbauer Spectroscopy in Chemistry and Biology. In Physical Inorganic Chemistry: Principles, Methods and Models*, Wiley & Sons, Inc., **2010**. Pages 39−67.

[43] Münck, E.; Stubna, A. *Mössbauer Spectroscopy: Bioinorganic. In Comprehensive Coordination Chemistry II*, Vol. 2, Pergamon: Oxford, **2003**. Pages 279−286.

[44] Salzmann, R.; McMahon, M. T.; Godbout, N.; Sanders, L. K.; Wojdelski, M.; Oldfield, E. *J. Am. Chem. Soc.* **1999**, 121, 3818-3828.

[45] Gubler, J.; Finkelmann, A. R.; Reiher, M. *Inorg. Chem.* **2013**, 52, 14205-14215.

[46] Borowski, T.; Noack, H.; Radoń, M.; Zych, K.; Siegbahn, P. E. M. *J. Am. Chem. Soc.* **2010**, 132, 12887-12898.

[47] Bochevarov, A. D.; Friesner, R. A.; Lippard, S. J. *J. Chem. Theory Comput.* **2010**, 6, 3735-3749 .

[48] Pápai, M.; Vankó, G. *J. Chem. Theory Comput.* **2013**, 9, 5004-5020.

[49] McWilliams, S. F.; Brennan-Wydra, E.; MacLeod, K. C.; Holland, P. L. *ACS Omega* **2017**, 2, 2594-2606.

[50] Römelt, M.; Ye, S.; Neese, F. *Inorg. Chem.* **2009**, 48, 784-785.

[51] (a) Neese, F. *WIREs Comput Mol Sci* **2012**, 2, 73-78. (b) Neese, F. *WIREs Comput Mol Sci* **2018**, 8, e1327.

Chapter 3

Ligand assisted proton shuttle

3.1 Background

General introduction

As we mentioned in Chapter 1, some electron poor complexes do not activate given C-X bond (X=heteroatom or H) by oxidative addition. An alternative activation process is based in the use of lone electron pairs in ligands in the first or second coordination sphere of the metal.[1] This subclass of metal-ligand cooperativity (MLC) has been of significant interest in recent years to facilitate the activation of these bonds.[2,3,4]

The ligands used for this purpose are often hemilabile. They show chelating properties but can switch their denticity to liberate a coordina-

tion position on the metal center for the incoming substrate. Carboxylate ligands are frequently used for this purpose because they present the perfect features of hemilability.[5,6] They have been extensively used in C—C bond forming reactions catalyzed by Pd complexes via direct arylation.[7,8]

Carboxylate complexes have been used in a wide range of stoichiometric or catalytic C—H bond activation and functionalization reactions.[9] The role of the carboxylate ligand during the C—H activation step has been deeply analyzed.[10] The operating mechanism has been labeled as concerted metalation deprotonation (CMD) or ambiphilic metal-ligand activation (AMLA) mechanisms.[11,12] This mechanism assumes that the resulting carboxylic acid (or the protonated ligand) decoordinates from the metal center and then transfers the proton to a sacrificial base.[13] A variation exists where the protonated ligand remains bound to the metal center where, acting as an intramolecular acid, can transfer the proton to a basic site on the substrate. This variation is known as ligand-assisted proton shuttle (LAPS) [14] mechanism and has been recognized, for instance, in the regioselective catalytic hydrations of terminal alkenes via ligand-assisted vinylidene tautomerizations (Scheme 3.1).[15] There are however scarce examples in the literature of systems following this mechanism.[16,17]

Scheme 3.1 Selected examples for the ligand assisted vinylidene tautomerization of terminal alkynes.

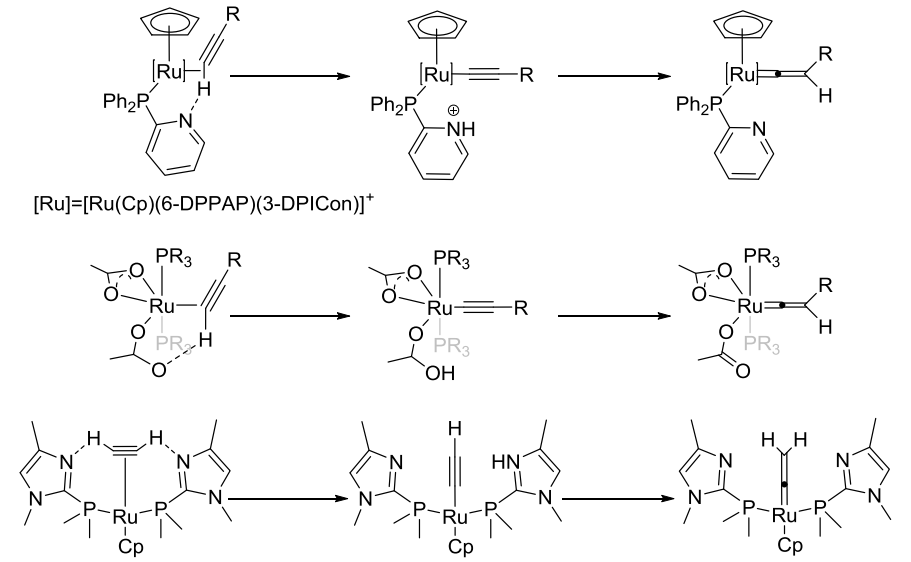

This LAPS reactivity is not exclusive of the carboxylate groups. Recently, Slattery and co-workers reported a thorough computational study on an unsaturated Ir(III) phosphoramidate complex able to activate 1-alkynes *via* metal-ligand cooperativity in a regio- and O-selective manner.[18] In the original experimental work, the Ir(III) complex $[Cp^*Ir(\kappa^2\text{-N,O-Xyl(N)P(O)(OEt)}_2)]^+$ (Xyl = 2,6-$Me_2C_6H_3$) was reported to react quickly and selectively with terminal alkynes to yield (E)-vinyloxyirida(III)cycles.[19] Slattery's group calculated all the possible C—H activation pathways, assisted or not by the phosphoramidate ligand: O-protonation, N-protonation, Cp*-protonation, direct oxidative addition and 1,2-hydrogen shift. They found that the most kinetically favored pathway was the activation of the C—H bond by the P=O group of the ligand following a CMD mechanism with a six-membered ring transition state structure. The resulting acetylide complex could then transfer the proton (*via* LAPS) from the P—OH group to the β carbon of the acetylide group forming a vinylidene complex. Finally, the O atom attacks the alpha carbon of the vinylidene group leading to the

experimentally observed product of the reaction (Scheme 3.2). Overall, the work highlights the ability of 1,3-heterobidentate chelating ligands to act as proton shuttle moiety and hence, promoting new transformations via MLC.[20]

Scheme 3.2 Schematic representation of the O-protonation pathway for the alkyne C—H activation bond *via* non-innocent ligand.

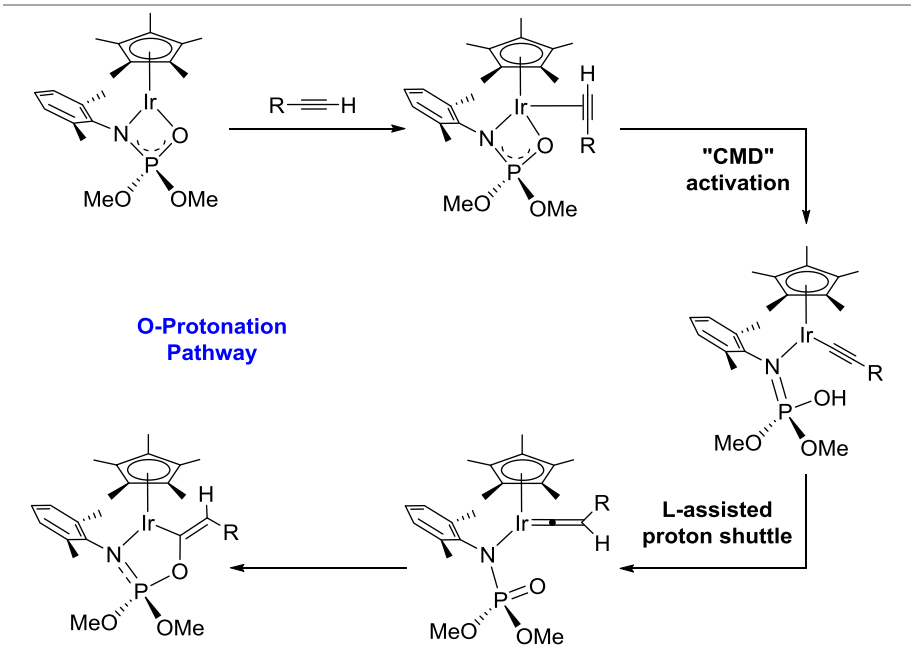

Besides the options mentioned above, other destinations for the proton are possible. For instance, its transfer to a neighbor ligand could unlock new reaction processes and trigger more elaborate catalytic transformations. In addition, the "re-use" of the transient carboxylic acid or protonated ligand, avows for a more atom-economically process.

Following our interest in homogeneous transformations with, *a priori*, out of the ordinary mechanisms, we started a collaboration with the experimental group of Prof. Sola (Zaragoza). They have a large experience in octahedral Ru(II) complexes bearing carboxylates ligands.[21,22] We were particularly interested in the experimental observation that the six-

coordinated Ru(II) hydride complex [Ru(OAc)H(CO)(P*i*Pr$_3$)$_2$] (**1**) is able to form the alkenyl (**2**) and alkynyl (**3**) derivatives upon addition of phenylacetylene.[23,24,25] In contrast, the five-coordinated chloro analog [Ru(Cl)H(CO)(P*i*Pr$_3$)$_2$] (**5**) is only observed to form the alkenyl derivative (**6**) even in the presence of excess alkyne at high temperature, as shown in Scheme 3.3.[26] The different behavior is counterintuitive, as one would expect the five-coordinate complex to be more reactive, and is likely related to a specific role for the acetate ligand.

Scheme 3.3 Reactivity of Ru(II) acetate (top) and chloro (bottom) complexes towards addition of different equivalents of phenylacetylene.

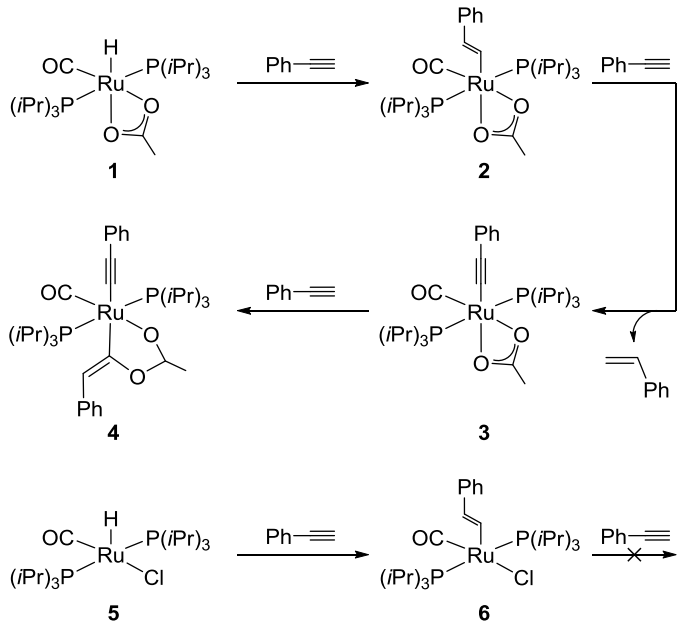

Experimental overview

The formation of the alkenyl complex [Ru(OAc)(E-CH=CHPh)(CO)(P*i*Pr$_3$)$_2$] (**2**) from the hydride complex [Ru(OAc)H(CO)(P*i*Pr$_3$)$_2$] (**1**) and its consumption to form the alkynyl derivative [Ru(OAc)(E-C≡CPh)(CO)(P*i*Pr$_3$)$_2$] (**3**) was followed by ^{31}P NMR in a toluene-d_8 solution. It was observed that both transformations occur at comparable rates. Figure 3.1 show the kinetic analysis

of the later transformation. The results were consistent with the expected second-order reaction between the alkenyl complex and the alkyne substrate. The kinetic experimental data was obtained in a range of temperatures (from 313 to 343 K) and by changing the initial concentration of phenylacetylene (from 0.73 to 2.19 M). As a result, experimental values for $\Delta H^{\ddagger}$ and $T\Delta S^{\ddagger}$ were obtained applying the Eyring equation, 16.2 (±1.3) and 7.1 (±0.8) kcal·mol^{-1}, respectively.

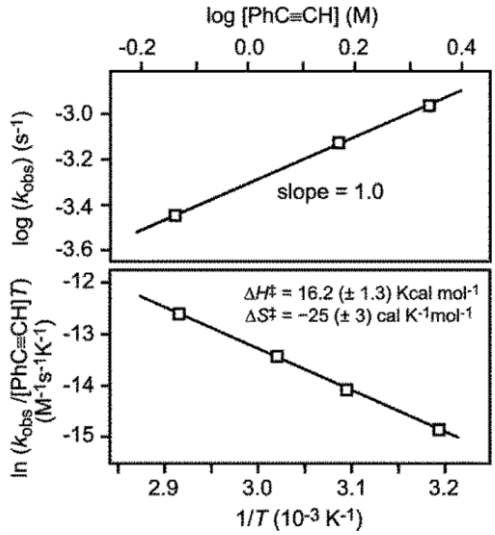

Figure 3.1 (above) Relation between pseudo-first-order rate constants (k_{obs}) and concentration of phenylacetylene for the transformation of **2** into **3**. (below) Eyring analysis of the second-order rate constants.

Further addition of phenylacetylene to the complex **3** accomplishes the formation of the alkenyl ester complex **4**. This transformation was observed to be slow, taking several days at room temperature. The hydride → alkenyl → alkynyl sequence shown in Scheme 3.3 is rather frequent in ruthenium chemistry and usually ends in butenynyl complexes as a result of the coupling of two alkyne groups.[27,28] Indeed, the analogue of complex **6** bearing PPh_3 instead of P*i*Pr$_3$ ligands was found to form the butenynyl derivative under forced conditions.[29] More recently, other complexes based on Fe,[30] Pd,[31] Rh [32] and Ru

containing different ligands,[33,34] have been reported to bear this scaffold group during the dimerization of terminal alkynes (Scheme 3.4).[35]

Scheme 3.4 Isolable complexes (left) and reaction intermediates (right) for the dimerization of alkynyl reaction.

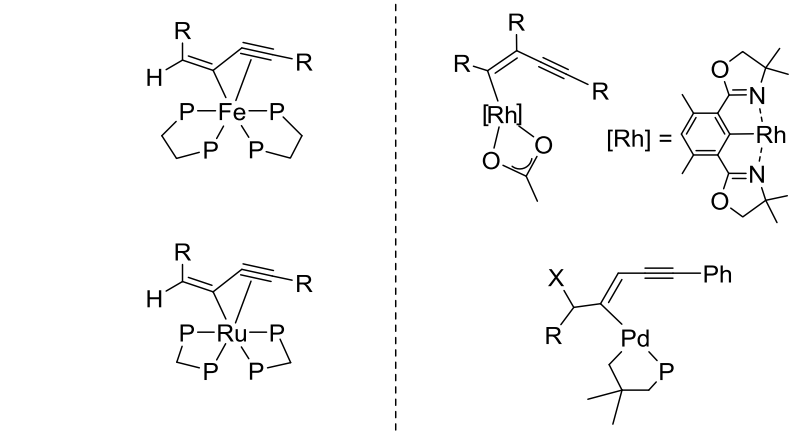

3.2 Computational details

Computational method

All the calculations in this chapter were carried out using the Gaussian09 (revision D.01) package.[36] The ωB97X-D functional (which includes atom-atom dispersion corrections) was used for all calculations.[37] All geometries were optimized without symmetry restrictions and the experimental solvent (toluene: ε = 2.3741) was implicitly considered in all the calculations through the SMD solvation model.[38] Vibrational frequency calculations for all stationary points were computed to establish their nature as minima (zero imaginary frequencies) or as transition states (one imaginary frequency). All the reported energies in this chapter are free energies in solution at 298.15 K and 1 atm, including zero point energy corrections (ZPE).

In order to reduce the basis set superposition error (BSSE), energies were further refined through single point calculations with an extended basis set. In a first set of calculations, all the structure optimization and frequency calculations were computed with the 6-31+G(d) basis set [39] for H, C, P, O and Cl atoms and SDD and its corresponding pseudopotential was selected for the Ru atom.[40] The potential energies were refined in a second set of calculations consisting of single point calculations in solution for the previously optimized geometries using the triple-zeta 6-311++G(d,p) basis set for H, C, P, O and Cl atoms.[41]

All the 3D structures shown in this chapter were drawn with the CYLview program,[42] using the following legend of colors for each atom: white for H, grey for C, red for O, orange for P, light green for Cl and dark green for Ru.

Computational model

In the first part of this work, we replaced the P*i*Pr$_3$ ligands on the complexes by smaller PMe$_3$ phosphines. This change was done to reduce the computational cost of the systems and to avoid possible conformational issues that could arise from the substituents of the P*i*Pr$_3$ phosphine. This modification should not significantly affect the electronic effects, although the reduced steric hindrance generated by the PMe$_3$ could affect in association-dissociation steps. Because of this, in a final set of calculations, the real system (P*i*Pr$_3$) was applied to evaluate all the possible mechanisms that could not be discarded with the model system (PMe$_3$).

3.3 Reaction mechanism

We ran several DFT calculations to elucidate the mechanisms governing the transformations with the chloro and the acetate complexes. The hydride to alkenyl reaction was first studied. Then, the direct H transfer from a second equivalent of phenylacetylene to the alkenyl complex was

analyzed for both systems with the model phosphine PMe_3. Even if there is no experimental evidence for the chloride system to further react with a second molecule of substrate, we checked this hypothetic pathway for comparison. This direct pathway would follow a ligand-to-ligand hydrogen transfer (LLHT) mechanism.[43] Finally, the calculations for the hydride to alkenyl reaction were repeated with the $P\textit{i}Pr_3$ real phosphine. In addition, the ligand-assisted proton shuttle (LAPS) mechanism was calculated for both systems.

Alkenyl complex formation with the model system

The first reaction to be analyzed is the insertion of the phenylacetylene substrate into the Ru—H bond of the model five-coordinated chloro complex **5m** (the m label refers to the model system). The preferred coordination position for the incoming acetylene substrate is in the *trans* position to the CO ligand. This had been previously rationalized by Eisenstein, Caulton and coworkers for this kind of complexes.[44] The complex has to distort its square-pyramidal geometry to allow the coordination of the phenylacetylene in *cis* position to the hydride ligand. The formation of the intermediate **I5m** is achieved *via* **TS 5m-I5m** with an activation barrier of 9.6 kcal·mol^{-1}. The next step of this transformation is the insertion of phenylacetylene into the Ru—H bond. The reaction evolves trough **TS I5m-6m**, 9.2 kcal·mol^{-1}, to form intermediate **6m**, 24.5 kcal·mol^{-1} below the initial reactants (Figure 3.2, green)

The alkenyl complex formation profile for the model acetate analog **1m** follows a qualitatively similar path. The relative energies for the acetylene coordination, intermediate **I1m** and subsequent insertion into the Ru—H bond, are higher by about 5-8 kcal·mol^{-1} in comparison with those of the chloro analogue. The coordination of phenylacetylene is the highest point of the profile for the formation of the alkenyl complex, **TS 1m-I1m**. The activation barrier is 16.2 kcal·mol^{-1}, still entirely affordable at room temperature (Figure 3.2, purple). The different relative

energies obtained for both systems can be explained by two reasons. First, the six-coordinate Ru(II) complex is quite more stable than the five-coordinate species. Second, the decoordination of one oxygen of the acetate ligand to open a vacancy for the incoming acetylene is more energy demanding than the distortion of the square-pyramidal geometry for the chloride complex.

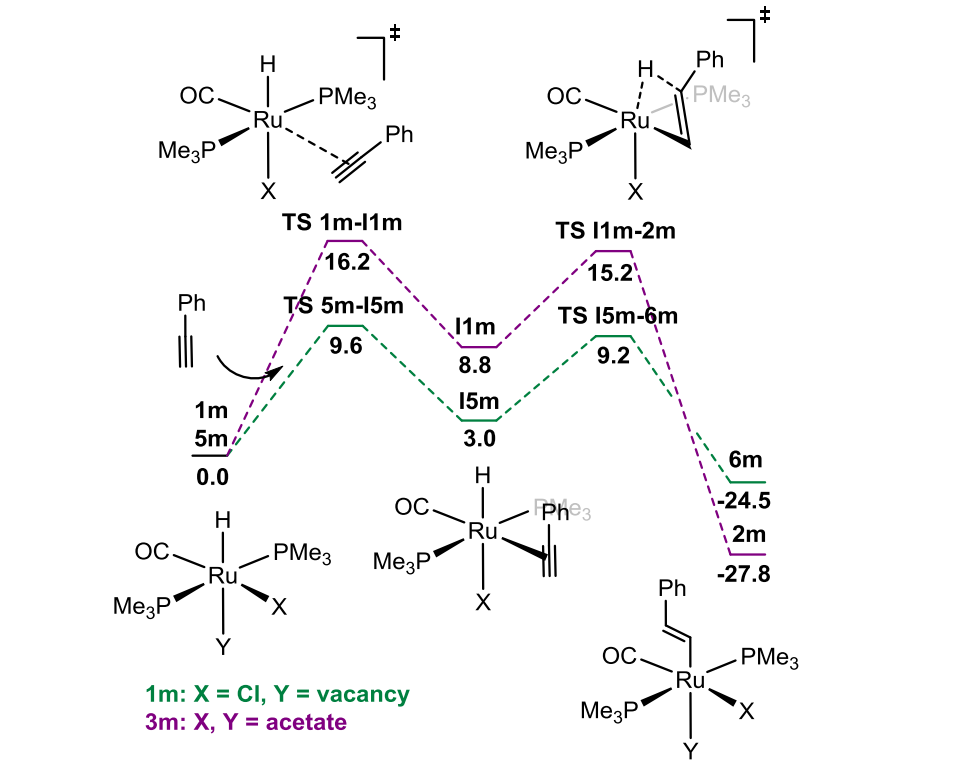

Figure 3.2 Free energy profile for hydride-to-alkenyl transformation with the PMe_3 model system. The chloro analog in green and the acetate complex in purple. Energies in kcal·mol^{-1}.

It is worth mentioning that possible isomers were checked for the coordination of the phenylacetylene for both chloro and acetate complex but were found higher in energy and thus not included on the discussion.

Alkynyl complex formation with the model system *via* LLHT

The reaction could continue with addition of extra phenylacetylene. As mentioned in the introduction section of this chapter, the chloro analog is not able to further react forming the alkynyl complex. In any case, we calculated the profile for both chloro and acetate model systems. First, we studied a non-ligand directed pathway where the Cl and OAc ligands just play a mere observer role and do not directly contribute on the reaction outcome. We label this mechanism as ligand-to-ligand hydrogen transfer (LLHT). The hydrogen bond of the second phenylacetylene substrate is transferred to the alkenyl moiety while a new Ru—C bond and a styrene molecule are formed (Figure 3.3).

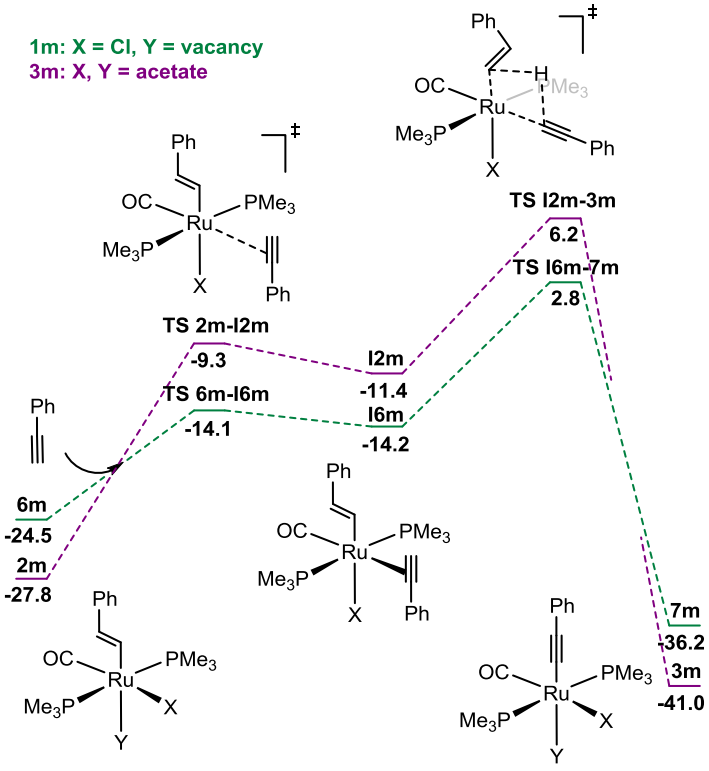

Figure 3.3 Free energy profile for alkenyl-to-alkynyl transformation with the PMe_3 model system, following the ligand-to-ligand hydrogen transfer (LLHT) mechanism. Chloro complexes in green and acetate complexes in purple. Energies in kcal·mol^{-1}, relative to the respective hydride complexes **1m** and **5m**.

The calculated profiles for both chloro and acetate model system follow the same steps (Figure 3.3). The coordination of the new phenylacetylene takes place in the position *trans* to the CO ligand. The barriers for this step are comparable to the hydride-to-alkenyl transformation presented previously, 10.4 and 18.5 kcal·mol^{-1}, for the chloro and acetate system, respectively. The highest energy point of this transformation is the transition state specifically associated to the LLHT step. The hydrogen transfer **TS I6m-7m** for the chloro model system has an activation barrier of 27.3 kcal·mol^{-1}. This value is in the upper limit for what is accepted for a step to be kinetically affordable at room temperature. In addition, the real system, which is more sterically hindered, would increase the barrier for this transition state. In a similar way, the calculated activation energy following the same mechanism for the acetate analog is as high as 34.0 kcal·mol^{-1} from intermediate **2m** to **TS I2m-3m**. The optimized structures of both transition states are shown in Figure 3.4.

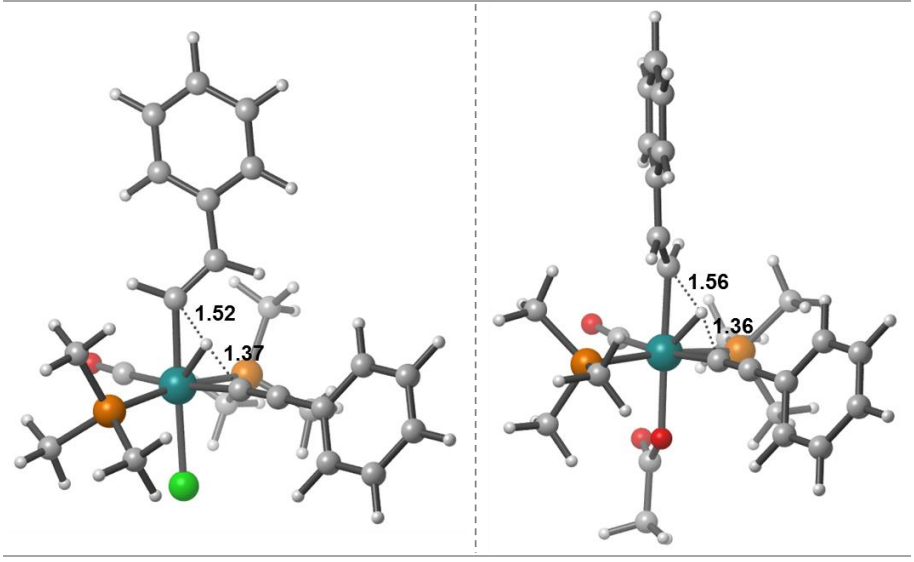

Figure 3.4 3D structures of **TS I2m-3m** (left) and **TS I6m-7m** (right). Selected bond distances in Å.

The direct pathway following the LLHT mechanism for the alkenyl-to-alkynyl reaction with the acetate system is thus, discarded due to the high barrier found for this mechanism.

Acetate, real system

From this point, we decided to switch to the real P*i*Pr$_3$system. The hydride-to-alkenyl reaction is essentially the same. The reaction starts with the coordination of the alkyne *trans* to the CO ligand. The associated transition state **TS 1-I1** for this coordination has a relative free energy of 21.7 kcal·mol^{-1}. Intermediate **I1** is formed after the first step and was found at 20.8 kcal·mol^{-1} above the initial complex **1**. Finally, the system evolves *via* alkyne insertion into Ru—H bond, **TS I1-2**, with an energy barrier of 23.2 kcal·mol^{-1}, to form the final alkenyl acetate complex **2**. The overall reaction is exergonic by 19.0 kcal·mol^{-1}. The relative energies for all the intermediates in this profile (Figure 3.5) are quite higher than that for the model system (Figure 3.2). This can be rationalized by the different size of the phosphine used for the model and the real system. The P*i*Pr$_3$ ligand generates a much more encumbered system and this has a destabilizing effect on the intermediates, which are more crowded than the reactants. For instance, the approximation of the phenylacetylene substrate to the initial complex **1** is more difficult due to the steric hindrance generated by the *i*Pr groups of the phosphine.

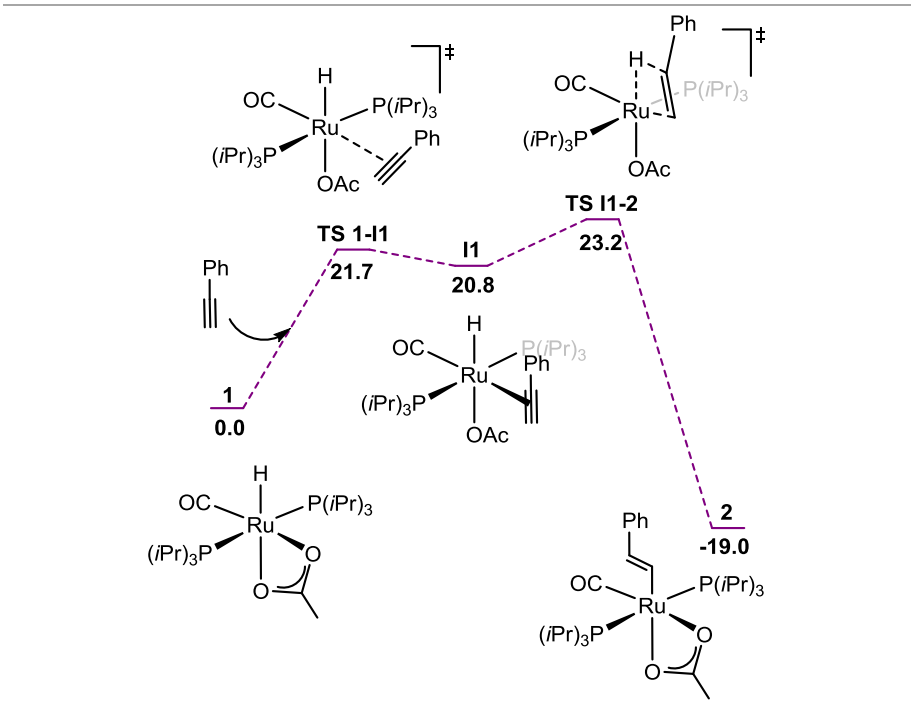

Figure 3.5 Free energy profile for the hydride-to-alkenyl reaction with the six-coordinated acetate complex, with the real system (P*i*Pr$_3$). Energies in kcal·mol^{-1}.

We then moved to the alkenyl-to-alkynyl reaction. As we mentioned before, we have discarded the direct mechanism for the model system where the acetate ligand had a mere observer role. For this reason, we decided to study a mechanism in which the acetate could act as a non-innocent ligand, and directly participate in the C—H activation step. This behavior would also explain the different reactivity between the chloro and the acetate alkenyl complexes towards the reaction with a phenylacetylene molecule.

In this alternative ligand assisted mechanism, the initial alkyne coordination can now take place at the most accessible position of intermediate **2**, *trans* to the alkene ligand (Figure 3.6). The transition state associated to the coordination, **TS 2-I2**, was found at 18.2 kcal·mol^{-1} from **2**. After the coordination, intermediate **I2** is formed which rapidly evolves to the alkenyl-alkynyl complex **I3**, *via* concerted

metalation deprotonation (CMD) mechanism. The associated transition state, **TS I2-I3**, is found only at 19.1 kcal·mol^{-1} from initial complex **2**.

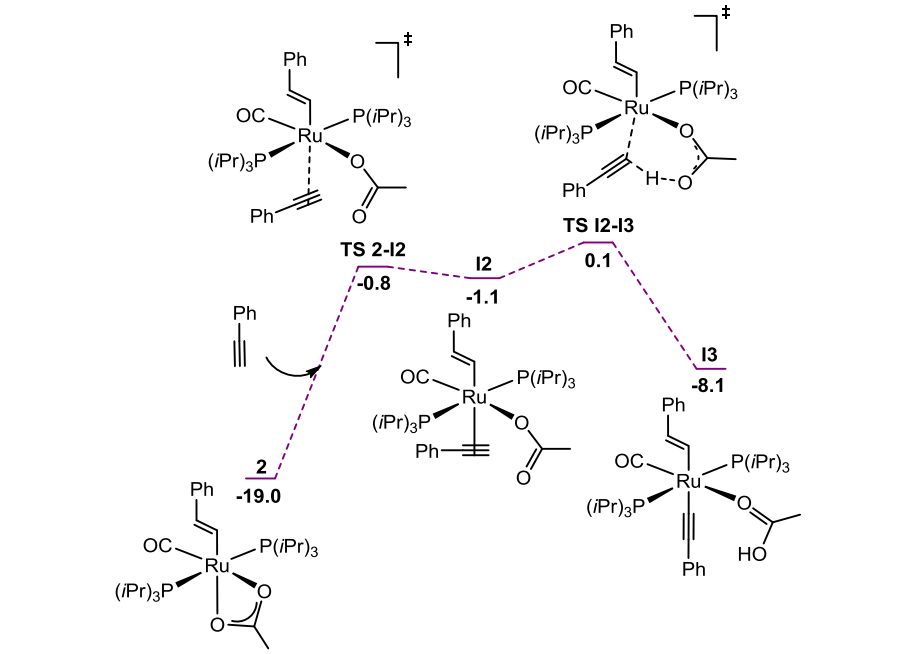

Figure 3.6 Free energy profile for the first part of the alkenyl-to-alkynyl transformation with the six-coordinated acetate complex, following a concerted metalation deprotonation (CMD) mechanism. Real system (P*i*Pr$_3$). Energies in kcal·mol^{-1}, relative to the precursor hydride complex **1**.

The optimized structure of **TS I2-I3** is shown in Figure 3.7. **TS I2-I3** displays a quasilinear alkynyl ∠C−C−C angle (175°), but the ∠Ru−C−C angle is smaller (144°), with the structure being reminiscent of an alkyne C−H σ-complex.[45] Moreover, the hydrogen atom is found at very similar distances between the C and the O atoms, 1.29 and 1.31 Å, respectively.

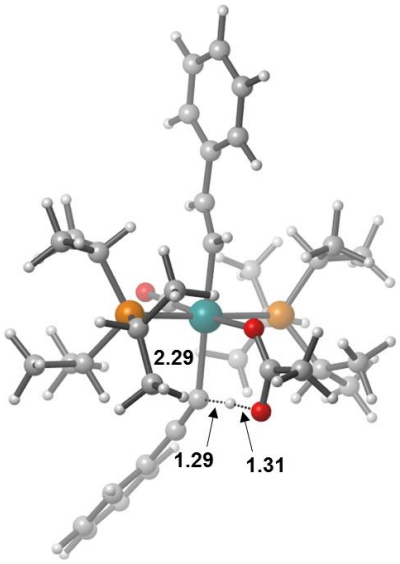

Figure 3.7 3D structure of **TS I2-I3**. Selected bond distances in Å.

From intermediate **I3**, the system can release acetic acid to form the five-coordinated **I4** complex. Then, the system evolves through **TS I4-I5** recoordinating the acetic acid in the proper manner to deliver its proton to the vinylic group. Finally, the final alkynyl complex **3** and a styrene molecule are formed *via* **TS I5-3**. This transfer is formally similar to previously reported examples of ligand-assisted proton shuttle (LAPS) mechanism. Interestingly, in this case, the proton transfer connects different ligands of the system, instead of different carbon centers of the same ligand (Figure 3.8). To the best of our knowledge, this is the first time that the LAPS mechanism promotes the proton transfer between different ligands.

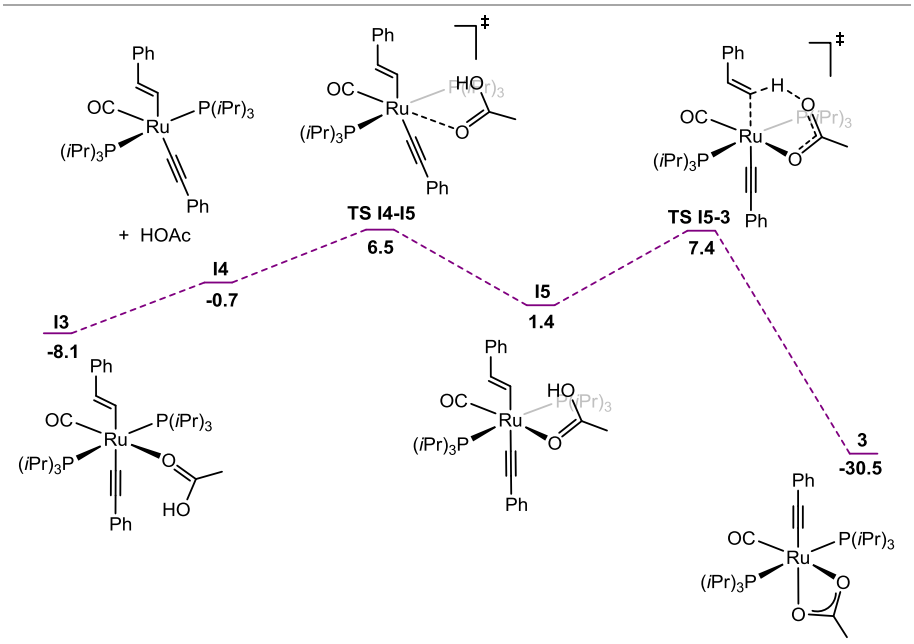

Figure 3.8 Free energy profile for the final part of the alkenyl-to-alkynyl reaction with the acetate complex, via ligand-assisted proton shuttle (LAPS) mechanism. Real system (P*i*Pr$_3$). Energies in kcal·mol^{-1}, relative to hydride complex **1**.

The free energy profile in Figure 3.8 shows two high lying transition states, **TS I4-I5** and **TS I5-3**, with similar activation barriers of 25.5 and 26.4 kcal·mol^{-1}, respectively, from complex **2**. These activation barriers are slightly higher than the experimental estimation of the barrier for this process, 23.7 (±2.1) kcal·mol^{-1}. Thus, both transition states are good candidates for the rate-limiting step. The decomposition of the free energy in the entropic and enthalpic terms, suggest that both transition states are equally compatible with the experiments. The experimental values are 16.2 (±1.3) and 7.1 (±0.8) for the enthalpic ($\Delta H^{\ddagger}$) and the entropic ($T\Delta S^{\ddagger}$) term, respectively. While the respective calculated parameters are 12.0 and 13.5 kcal·mol^{-1} for **TS I4-I5** and 12.8 and 13.6 kcal·mol^{-1} for **TS I5-3**. Evidently, the entropic effects are overestimated in the calculations, although the signs of the contributions are correct. The optimized geometries of both transition states are shown in Figure 3.9.

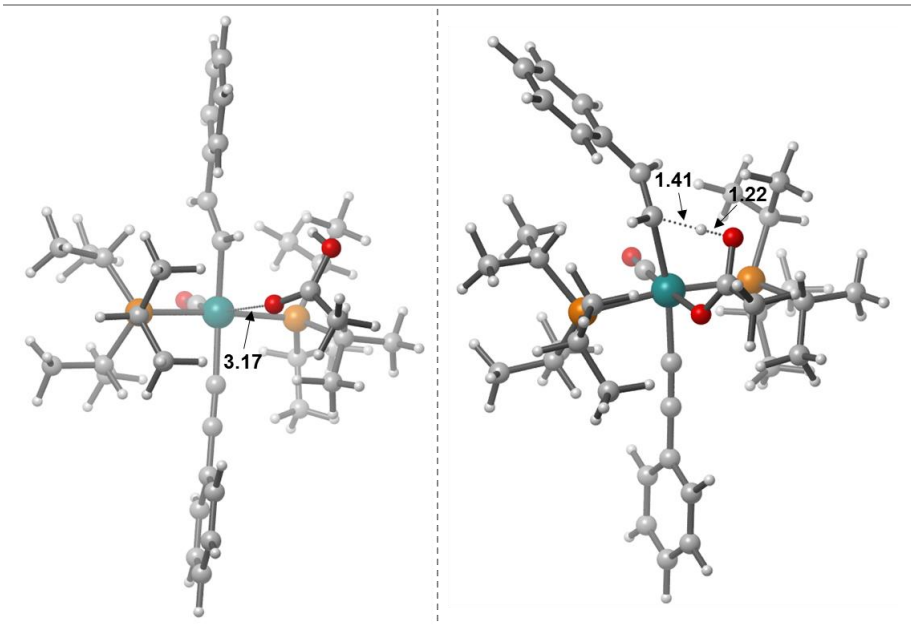

Figure 3.9 3D structure of **TS I4-I5** (left) and **TS I5-3** (right). Selected bond distances in Å.

We could finally identify the rate-determining step by examining the experimental kinetic isotopic effect (KIE). Experiments observed a KIE value of 1.6 using PhC≡CD as reagent. This value, relatively close to 1, indicates that the rate-limiting step does not involve C—H or O—H bond breaking process.[46] **TS I5-3** is thus discarded, especially after confirming that its geometry is not particularly early (Figure 3.9, right).[47] Accordingly, the joint consideration of experimental (KIE) and computational (geometry) results point to **TS I4-I5** as the highest energy point of the mechanism.

Chloride, real system

We recomputed the hydride-to-alkenyl reaction with the real system (P*i*Pr3) for the chloro analog following the same scheme showed above for the acetate system. We also explored the possible existence of the CMD/LAPS sequence with complex **6** (Figure 3.11).

The profile for the hydride-to-alkenyl transformation accomplished by complex **5** is depicted in Figure 3.10. As for the acetate system, going from the model to the real system, increases the activation barrier for the alkyne insertion into the Ru—H bond by *ca.* 10 kcal·mol^{-1}. Nevertheless, the higher point on this profile is 20.6 kcal·mol^{-1} for **TS I6-6**. Thus, the reaction would proceed smoothly towards the formation of the alkenyl complex **6**.

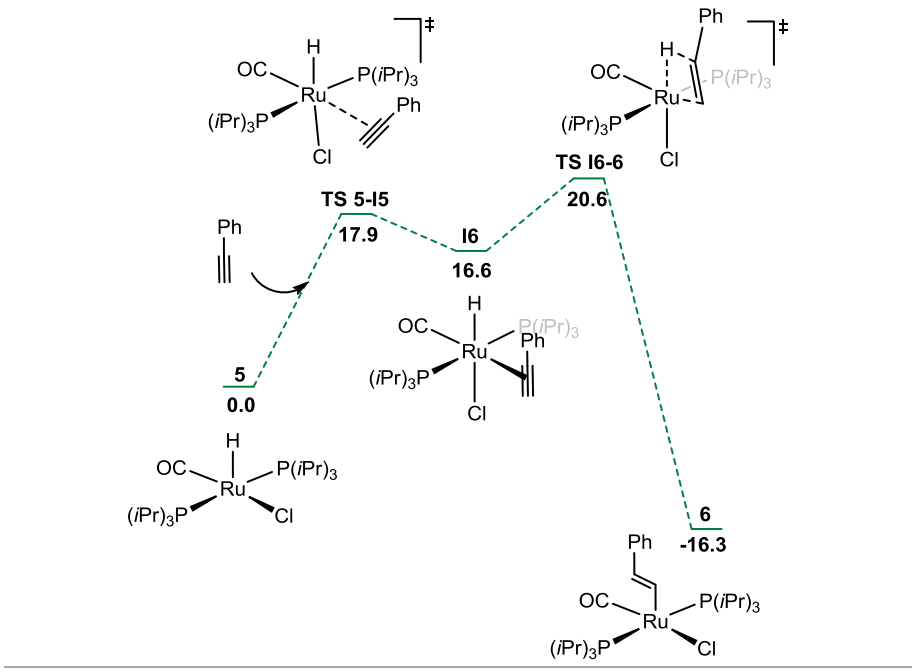

Figure 3.10 Free energy profile for the hydride-to-alkenyl reaction with the five-coordinated chloro complex, with the real system (P*i*Pr$_3$). Energies in kcal·mol^{-1}.

Next, we computed the possible assistance of the Cl ligand towards the activation of the C—H bond of a second molecule of phenylacetylene. As expected from the experimental reactivity, the transition state **TS I7-I8** to achieve intermediate **I8**, which is the chloro analog of **I3** intermediate, is prohibitively high, 34.8 kcal·mol^{-1}. The chloride ligand is much less basic than acetate, and thus less efficient as proton acceptor. In addition, the final complex after the CMD mechanism, **I8**, is much less stable than its acetate analog **I3** (20.8 vs 10.9 kcal·mol^{-1}, respective-

ly). This raises the energy of the previous transition state and effectively prevents the alkenyl-to-alkynyl transformation.

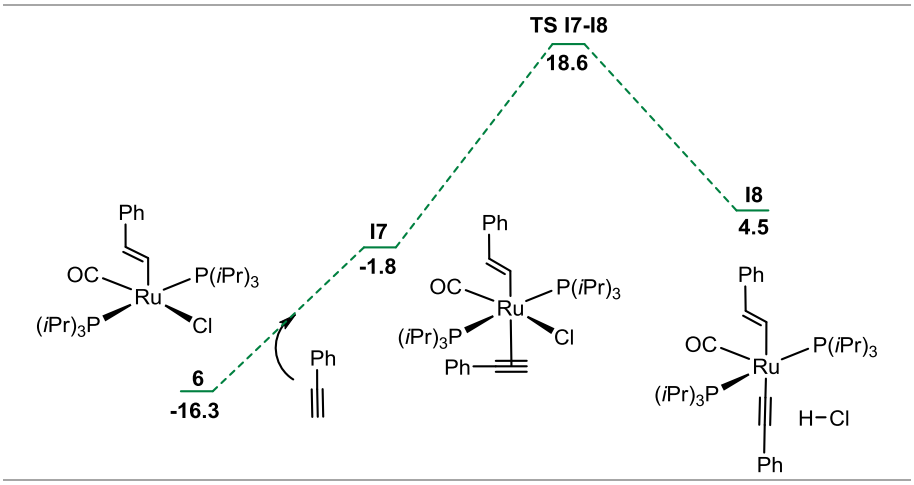

Figure 3.11 Free energy profile for the experimentally not-observed alkenyl-to-alkynyl transformation with the chloro complex, following a concerted metalation deprotonation (CMD) mechanism. Real system ($P\textit{i}Pr_3$). Energies in kcal·mol^{-1}, relative to the precursor hydride complex **5**.

The different stabilities of **I3** and **I8** can be rationalized by looking at the optimized structures of these intermediates. **I3** is a six-coordinated complex thanks to the ability of the generated acetic acid to coordinate to the metal center by the carboxylic oxygen. In contrast, the generated acid chloride does not interact with the metal center, but it generates a Cl—H···π interaction with the alkynyl ligand. However, this interaction is not as stabilizing as the instability generated by the formation of a five-coordinated complex. The optimized structures of both chloro and acetate analogs are shown in Figure 3.12.

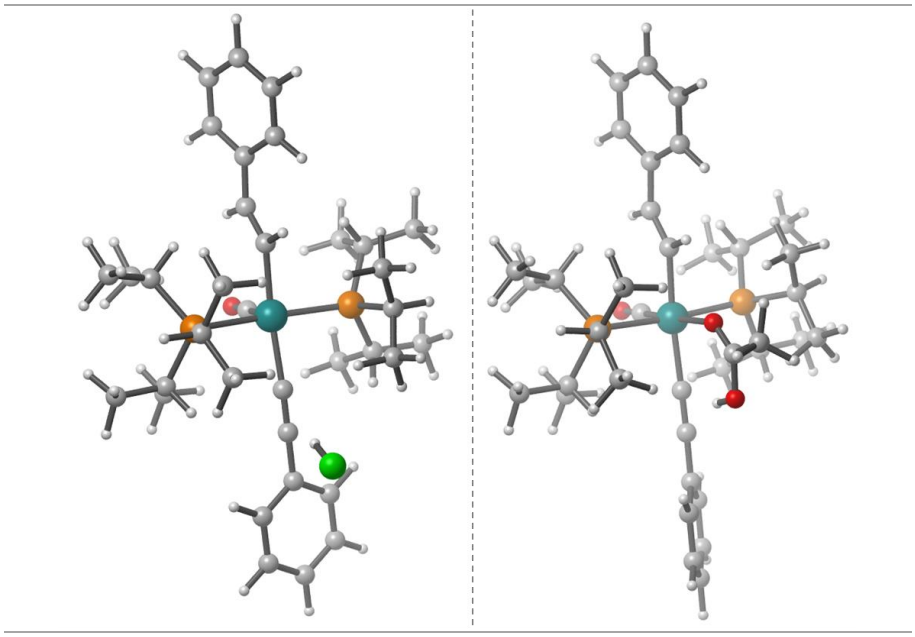

Figure 3.12 3D structure of intermediates **I8** (left) and **I3** (right).

3.4 Conclusions and extrapolation to other systems

In this chapter we have rationalized the different reactivity of the chloro and acetate ligands in [Ru(X)H(CO)(P*i*Pr$_3$)$_2$] (X= Cl or OAc) complexes toward the activation of phenylacetylene molecules. The chloro system is able to react with one molecule of phenylacetylene to complete the hydride-to-alkenyl transformation. The acetate system can react further with a second equivalent of phenylacetylene to achieve the alkenyl-to-alkynyl reaction. The culprit of this enhanced reactivity is the acetate ligand. Our calculations shown that it is able to assist on the C—H bond activation step, *via* concerted metalation deprotonation (CMD), and also subsequently deliver the H atom to a different part of the complex, following a variation of the well-known ligand-assisted proton shuttle (LAPS) mechanism. In this particular case, the acetate transfers a proton from two *trans* ligands. This behavior emerges as a simple paradigm to circumvent the ubiquitous energy consuming distortions

required to accommodate reactive ligands in relative *cis* positions of catalytically active complexes.

Scheme 3.5 Catalytic cycles for the synthesis of dehydrogenative silylations and hydrosilylation products.

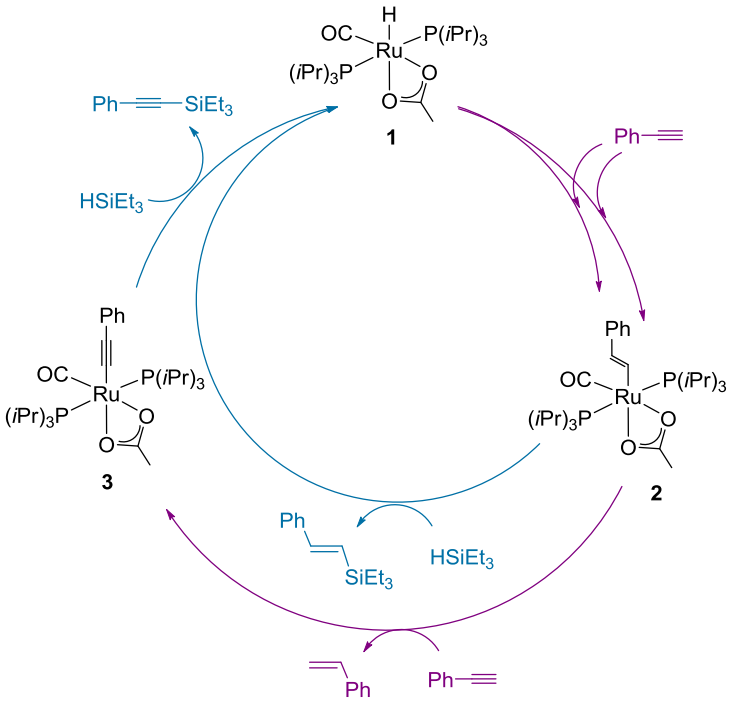

Consequences of this non-innocent activation mode by the acetate ligand can be inferred from the reported catalytic behavior of this kind of complexes in the hydrosilylation reactions of 1-alkynes.[48,49] The replacement of chloride by acetate in the $[Ru(X)H(CO)(PPh_3)_n]$ catalyst was observed to change the chemoselectivity in the addition of triethylsilane to phenylacetylene, favoring dehydrogenative silylations products ($PhC{\equiv}CSiEt_3$ and styrene) over those of hydrosilylation (Z- and E-alkenylsilanes) (Scheme 3.5).[22] This selectivity variation is in agreement with the mechanism proposed in this chapter where the non-innocent acetate ligand can promote the alkenyl-to-alkynyl transformation. The reaction produces styrene together with alkynyl complexes, which were found key intermediates in dehydrogenative silylations.[50]

As final remark, the study of this sophisticated and non-conventional mechanism can have implications for the rational design of new active complexes which could affect to the discovery of novel transformations.

3.5 References

[1] Bercaw, J. E.; Labinger, J. A. *Proc. Natl. Acad. Sci. U. S. A.* **2007**, 104, 6899-6900 and references therein.

[2] Davies, D. L.; Donald, S. M. A.; Al-Duaij, O.; Macgregor, S. A.; Pölleth, M. *J. Am. Chem. Soc.* **2006**, 128, 4210-4211.

[3] Qi, X.; Li, Y.; Bai, R.; Lan, Y. *Acc. Chem. Res.* **2017**, 50, 2799-2808.

[4] Eisenstein, O.; Milani, J.; Perutz, R. N. *Chem. Rev.* **2017**, 117, 8710-8753.

[5] Ackermann, L. *Chem. Rev.* **2011**, 111, 1315-1345.

[6] Ackermann, L. *Acc. Chem. Res.* **2014**, 47, 281-295.

[7] Cho, S.-H.; Kim, J. Y.; Kwak, J.; Chang, S. *Chem. Soc. Rev.* **2011**, 40, 5068-5083.

[8] Lyons, T. W.; Sanford, M. S. *Chem. Rev.* **2010**, 110, 1147-1169.

[9] Crabtree, R. H. *The Organometallic Chemistry of the Transition Metals*, 4th ed.; John Wiley & Sons, Inc.: Hoboken, NJ, **2005**.

[10] Davies, D. L.; MacGregor, S. A.; McMullin, C. L. *Chem. Rev.* **2017**, 117, 8649-8709.

[11] Lapointe, D.; Fagnou, K. *Chem. Lett.* **2010**, 39, 1118-1126.

[12] Boutadla, Y.; Davies, D. L.; Macgregor, S. A.; Poblador-Bahamonde, A. I. *Dalton Trans* **2009**, 5887-5893.

[13] Lafrance, M.; Fagnou, K. *J. Am. Chem. Soc.* **2006**, 128, 16496-16497.

[14] Johnson, D. G.; Lynam, J. M.; Slattery, J. M.; Welby, C. E. *Dalton Trans.* **2010**, 39, 10432-10441.

[15] Breit, B.; Gellrich, U.; Li, T.; Lynam, J. M.; Milner, L. M.; Pridmore, N. E.; Slattery, J. M.; Whitwood, A. C. *Dalton Trans.* **2014**, 43, 11277-11285.

[16] Welby, C. E.; Eschemann, T. O.; Unsworth, C. A.; Smith, E. J.; Tatcher, R. J.; Whitwood, A. C.; Lynam, J. M. *Eur. J. Inorg. Chem.* **2012**, 1493-1506.

[17] Arita, J. A.; Cantada, J.; Grotjahn, D. B.; Cooksy, A. L. *Organometallics* **2013**, 32, 6867-6870.

[18] Leeb, N. M.; Drover, M. W.; Love, J. A.; Schafer, L. L.; Slattery, J.M. *Organometallics* **2018**, 37, 4630-4638.

[19] Drover, M. W.; Love, J. A.; Schafer, L. L. *J. Am. Chem. Soc.* **2016**, 138, 8396-8399.

[20] Drover, M. W.; Love, J. A.; Schafer, L. L. *Chem. Soc. Rev.* **2017**, 46, 2913-2940.

[21] Sola, E.; García-Camprubí, A.; Andres, J. L.; Martín, M.; Plou, P. *J. Am. Chem. Soc.* **2010**, 132, 9111-9121.

[22] Martin, M.; Sola, E.; Lahoz, F. J.; Oro, L. A. *Organometallics* **2002**, 21, 4027-4029.

[23] Esteruelas, M. A.; Werner, H. *J. Organomet. Chem.* **1986**, 303, 221-231.

[24] Werner, H.; Esteruelas, M. A.; Otto, H. *Organometallics* **1986**, 5, 2295-2299.

[25] Esteruelas, M. A.; Lahoz, F. J.; López, A. M.; Oñate, E.; Oro, L. A. *Organometallics* **1994**, 13, 1669-1678.

[26] Esteruelas, M. A.; Herrero, L. A.; Oro, L. A. *Organometallics* **1993**, 12, 2377-2379.

[27] El Guaouzi, M.; Yáñez, R.; Ros, J.; Alvarez-Larena, A.; Piniella, J. F. *Inorg. Chem. Commun.* **1999**, 2, 288-291.

[28] Bassetti, M.; Marini, S.; Tortorella, F.; Cadierno, V.; Díez, J.; Gamasa, M. P.; Gimeno, J. *J. Organomet. Chem.* **2000**, 593-594, 292-298.

[29] Santos, A.; López, J.; Matas, L.; Ros, J.; Galán, A.; Echavarren, A. M. *Organometallics* **1993**, 12, 4215-4218.

[30] Field, D. L.; Magill, A. M.; Pike, S. R.; Turnbull, A. J.; Dalgarno, S. J.; Turner, P. Willis, A. C. *Eur. J. Inorg. Chem.* **2010**, 2406-2414.

[31] Lauer, M. G.; Headford, B. R.; Gobble, O. M.; Weyhaupt, M. B.; Gerlach, D. L.; Zeller, M.; Shaughnessy, K. H. *ACS Catal.* **2016**, 6, 5834-5842.

[32] Ito, J.-I.; Kitase, M.; Nishiyama, H. *Organometallics*, **2007**, 26, 6412-6417.

[33] Eaves, S. G.; Yufit, D. S.; Skelton, B. W.; Lynam, J. M.; Low, P. J. *Dalton Trans.* **2015**, 44, 21016-21024.

[34] Salvio, R.; Juliá-Hernández, F.; Pisciottani, L.; Mendoza-Meroño, R.; García-Granda, S.; Bassetti, M. *Organometallics* **2017**, 36, 3830-3840.

[35] Trost, B. M.; Masters, J. T. *Chem. Soc. Rev.* **2016**, *45*, 2212-2238.

[36] Frisch, M. J.; Trucks, G. W.; Schlegel, H. B.; Scuseria, G. E.; Robb, M. A.; Cheeseman, J. R.; Scalmani, G.; Barone, V.; Mennucci, B.; Petersson, G. A.; Nakatsuji, H.; Caricato, M.; Li, X.; Hratchian, H. P.; Izmaylov, A. F.; Bloino, J.; Zheng, G.; Sonnenberg, J. L.; Hada, M.; Ehara, M.; Toyota, K.; Fukuda, R.; Hasegawa, J.; Ishida, M.; Nakajima, T.; Honda, Y.; Kitao, O.; Nakai, H.; Vreven, T.; Peralta, J. E., Jr; Ogliaro, F.; Bearpark, M.; Heyd, J. J.; Brothers, E.; Kudin, K. N.; Staroverov, V. N.; Kobayashi, R.; Normand, J.; Raghavachari, K.; Rendell, A.; Burant, J. C.; Iyengar, S. S.; Tomasi, J.; Cossi, M.; Rega, N.; Millam, J. M.; Klene, M.; Knox, J. E.; Cross, J. B.; Bakken, V.; Adamo, C.; Jaramillo, J.; Gomperts, R.; Stratmann, R. E.; Yazyev, O.; Austin, A. J.; Cammi, R.; Pomelli, C.; Ochterski, J. W.; Martin, R. L.; Morokuma, K.; Zakrzewski, V. G.; Voth, G. A.; Salvador, P.; Dannenberg, J. J.; Dapprich, S.; Daniels, A. D.; Farkas, O.; Foresman, J. B.; Ortiz, J. V.; Cioslowski, J.; Fox, D. J. Gaussian 09, revision D.01; Gaussian Inc.: Wallingford, CT, **2013**.

[37] Chai, J. D.; Head-Gordon, M. *Phys. Chem. Chem. Phys.* **2008**, 10, 6615-6620.

[38] Marenich, A. V.; Cramer, C. J.; Truhlar, D. G. *J. Phys. Chem. B* **2009**, 113, 6378-6396.

[39] Francl, M. M.; Pietro, W. J.; Hehre, W. J.; Binkley, J. S.; Gordon, M. S.; DeFrees, D. J.; Pople, J. A. *J. Chem. Phys.* **1982**, 77, 3654-3665.

[40] Bergner, A.; Dolg, M.; Kuechle, W.; Stoll, H.; Preuss, H. *Mol. Phys.* **1993**, 80, 1431-1441.

[41] Krishnan, R.; Binkley, J. S.; Seeger, R.; Pople, J. A. *J. Chem. Phys.* **1980**, 72, 650-654.

[42] Legault, C. Y. CYLview, 1.0b; Université de Sherbrooke: Quebec, Montreal, Canada, **2009**; www.cylview.org

[43] Guihaumé, J.; Halbert, S.; Eisenstein, O.; Perutz, R. N. *Organometallics* **2012**, 31, 1300-1314.

[44] Marchenko, A. V.; Gérard, H.; Eisenstein, O.; Caulton, K. G. *New J. Chem.* **2001**, 25, 1244-1255.

[45] Cowley, M. J.; Lynam, J. M.; Slattery, J. M. *Dalton Trans.* **2008**, 4552-4554.

[46] Gómez-Gallego, M.; Sierra, M. A. *Chem. Rev.* **2011**, 111, 4857-4963.

[47] Algarra, A. G.; Cross, W. B.; Davies, D. L.; Khamker, Q.; Macgregor, S. A.; McMullin, C. L.; Singh, K. *J. Org. Chem.* **2014**, 79, 1954-1970.

[48] Zaranek, M.; Marciniec, B.; Pawluc, P. *Org. Chem. Front.* **2016**, 3, 1337-1344.

[49] Gao, R.; Pahls, D. R.; Cundari, T. R.; Yi, C. S. *Organometallics* **2014**, 33, 6937-6944.

[50] Esteruelas, M. A.; Olivan, M.; Oro, L. A. *Organometallics* **1996**, 15, 814-822.

UNIVERSITAT ROVIRA I VIRGILI
NON-INNOCENT LIGANDS: FROM PRO-TON SHUTTLE TO PHOTO-ACTIVATION
Adiran de Aguirre Fondevila

Chapter 4

Redox active ligands

4.1 Background

General introduction

Iron complexes bearing N- and S-donor ligand have received increased interest in recent years. This is in part due to their impressively diverse structural features and interesting reactivity, as well as the role that these Fe—N or Fe—S ligand motifs play in biological catalysis.[1,2,3,4,5,6] Several well characterized examples of these scaffolds are present in enzymatic catalysts for many different reactions. For example, dinuclear iron cluster with bridging sulfur atoms have been found in the active site of [FeFe]-hydrogenase metalloenzymes. These enzymes can catalyze the formation of dihydrogen from electrons and protons in a reversible manner.[7,8] Another example is the nitrogenase enzyme, which contains a [Fe—S] cluster in its active site, and is able to effectively catalyze the biological reduction of N_2 to ammonia.[9,10] In general, it has been

reported that the structural and dynamic features of these [Fe—S] cores (*e.g.,* the [4Fe-3S] cluster on the [Ni—Fe]-hydrogenase, which is able to work under aerobic conditions), are especially important for the catalytic activities of these enzymes.[11,12,13] This has attracted many interest in the scientific community, in order to mimic their features and apply them to new transformations.

In this regard, several dinuclear iron complexes of the type $[Fe_2(\mu\text{-}S)_2(CO)_{6-x}L_x]$ and $[Fe_2(\mu\text{-}SR)_2(CO)_{6-x}L_x]$ (L = CN, NO, P-donor ligands, etc.) have been developed as synthetic hydrogenase imitators as well as potential electrocatalysts for hydrogen evolution (Scheme 4.1).[14,15,16,17] Kinoshita and co-workers reported in 2014, a new class of C- and S-bridged dinuclear iron carbonyl complexes bearing an unsymmetrical $S^-C^-N^R$ pincer ligand that can serve as electrocatalysts for proton reduction.[18]

Scheme 4.1 (A) Active center of [FeFe]-hydrogenase enzyme. (B-D) Complexes inspired on hydrogenases active center.

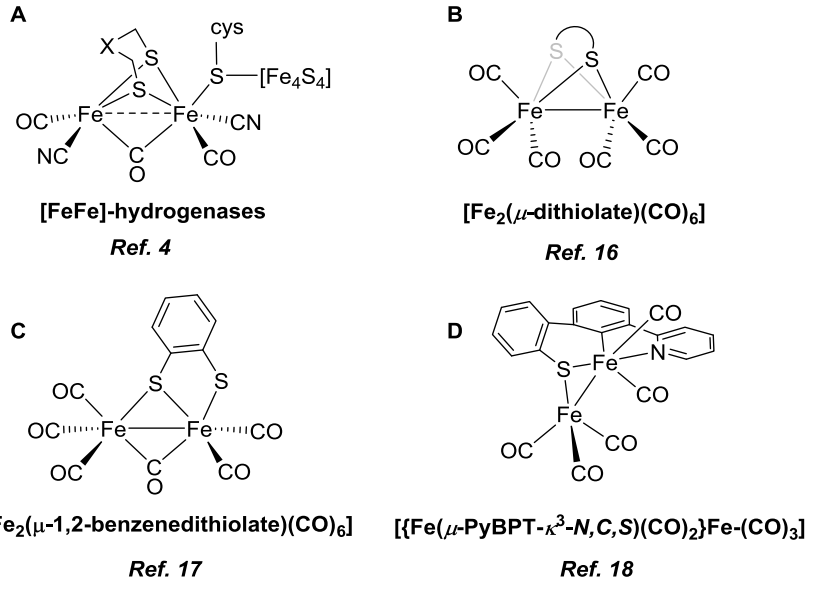

Nonheme iron enzymes such as nitrile hydratase [19,20,21] or superoxide reductases,[22] contain mononuclear iron-bound thiolates with N-

donor ligands in their active sites. These enzymes can catalyze many biologically relevant reactions, for instance, hydration of nitriles to the corresponding amides, reduction of superoxide to hydrogen peroxide, and oxidation of L-cysteine to cysteine sulfinic acid. In this context, Goldberg *et al.* reported two mononuclear iron complexes bearing thiolate- (N_3PyS^-) and thioether- (N_3PyS^R) scaffolds. These complexes function as biomimetic replicas, mimicking the structural and practical features of nonheme iron enzymes.[23,24]

The huge interest for this kind of ligand motifs can be easily rationalized. The combination of multidentate ligands featuring hard and soft donor centers, provides access to many complexes with new and different reactivity. Thioether ligands generally form weak bonds with first-row transition metals [25,26,27,28] and their hemilability has already been extensively demonstrated.[29,30,31,32] On the other hand, thiolate groups typically bind more strongly to metals, in a terminal or bridging manner, which gives access to the formation of mononuclear or multimetallic complexes, respectively. In addition, the lone pair electrons of the thiolate groups are reactive toward bifunctional substrate activation. Similarly, for the nitrogen part of the ligand, imine (neutral) or amido (charged) groups can also be found in this type of scaffolds. Their properties are similar than those explained above for the S-donor moieties.

Another important feature of these ligands is the ability to stabilize different oxidation states on the iron center.[33,34,35] This enhanced stabilization also promotes obtaining interesting magnetic properties in these complexes, and therefore, exciting reactivity.[36,37]

A wide diversity of tridentate mixed-donor ligands bearing N and S groups are known. For instance, [$S^RN^-S^R$],[38,39,40] [$S^-N^-S^-$],[41] [$S^RN^-O^-$],[42] [$S^-N^-N^R$],[43] and [$N^-S^R\ N^-$] [25,33] complexes have been reported (Scheme 4.2). Remarkably, almost all these sulfur-based amido ligands have been studied in iron complexes. But only in rare

cases its catalytic activity has been tested. Nevertheless, some examples exist on the literature, for instance, ruthenium,[39] chromium,[29] zinc [44] and iron complexes bearing this kind of ligands,[44] where their catalytic activity have been measured for a given reaction. Interestingly, some of the complexes mentioned above display hemilabile character, especially those containing pincer ligands with thioether arms.[28,31,32]

Scheme 4.2 Sulfur-based amido ligands.

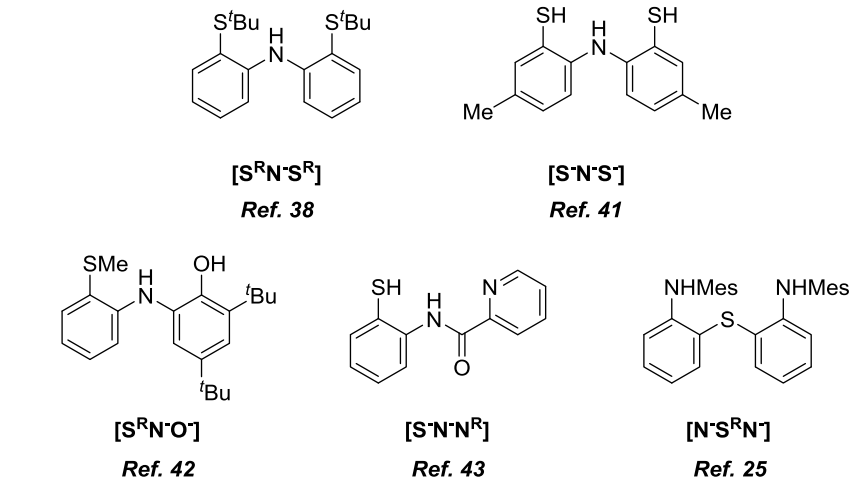

In 1998, Bouwman *et al.* reported the easy coupling of a thio-functionalized aldehyde and an aminothiol molecule for the synthesis of a [$S^{t\text{-}Bu}N^{H}S$] heterocycle. An equilibrium between the closed and the open chain imine isomer of the heterocyclic molecule is observed when it is introduced in chloroform solution. The treatment of this compound with nickel acetate achieved a mononuclear Ni(II) complex where the open chain isomer is coordinated in a tridentate manner to the metal center. Interestingly, the reaction of the [$S^{t\text{-}Bu}N^{H}S$] heterocycle with nickel tetrafluoroborate, yielded a dinuclear [$S^{-}NS^{-}$]-ligated Ni(II) complex. A remarkable feature of this system is that the *tert*-butyl substituents of the thioether group have been released and the subsequent thiolate group is linking the two nickel centers (Scheme 4.3).[45]

Scheme 4.3 Ni(II) complexes reported by Bouwman upon addition of different nickel salts to [$S^{t\text{-}Bu}N^{H}S$].

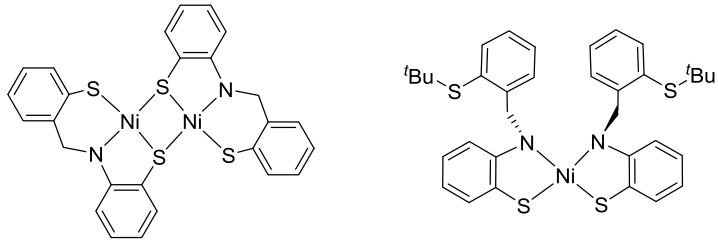

$[Ni_2(SNS)_2]$ **$[Ni(^tBuSN)_2]$**

With all of this in hand, Baker and co-workers reported in 2016, the synthesis of a new [$S^{Me}N^{H}S$] ligand. This ligand was very similar to that reported by Bouwman before, but the *tert*-butyl group was replaced by a methyl group. This modification gives rise to a more stable version of the ligand. In addition, its synthesis can be achieved in high yield from commercially available materials in a single step (Scheme 4.4).[46]

Scheme 4.4 Synthesis of [$S^{Me}N^{H}S$] from commercially available starting materials.

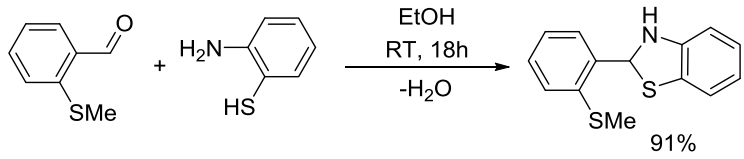

Addition of the [$S^{Me}N^{H}S$] ligand to the $Fe(OTf)_2$ salt in the presence of base (NaO^tBu) and in acetonitrile solvent, afforded a trinuclear iron complex $[Fe_3(\mu_2\text{-}S^{Me}NS^{-})_4](OTf)_2$ (**1**). This complex was fully characterized by structural and spectroscopic methods. The combination of spectroscopic techniques (UV-vis, Mössbauer, NMR), magnetic measurements (in solution and solid state) and computational (DFT) studies, revealed that the central Fe(II) atom is a high-spin (S =2) center, while the peripheral Fe(II) centers are both low-spin (S = 0).

Complex **1** is able to react further with excess of a variety of ligands such as L = $PMePh_2$, CNxylyl (2,6-dimethylphenyl isocyanide), or

$P(OMe)_3$ in CH_3CN to form the respective dinuclear Fe(II) complexes, $\{[Fe(\mu\text{-}S^{Me}NS^{-})L_2]_2\}(OTf)_2$ (**2−4**). All these dinuclear complexes were also fully characterized and found to be diamagnetic, with two thiolate groups linking both metal centers (Scheme 4.5).

Scheme 4.5 Synthesis of iron trinuclear (**1**) and dinuclear complexes (**2-4**).

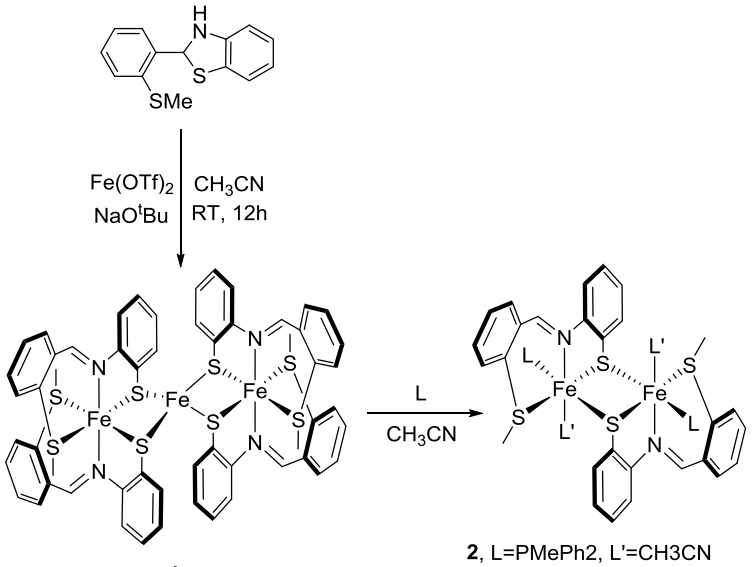

In a different report, Baker and co-workers shown that treatment of two equivalents of the aforementioned $[S^{Me}N^{H}S]$ ligand with a low-coordinated iron complex $Fe\{N(SiMe_3)_2\}_2$, in THF at room temperature, afforded a new dimeric complex **5** with the form $[Fe(N_2S_2)]_2$ in 92% yield (Scheme 4.6).[47] This new complex **5** was characterized by ^1H NMR, UV-vis spectroscopy, ESI-MS and single-crystal X-ray diffraction. It was found to be a paramagnetic species. The structure of this dimeric iron complex shown the thiolate groups linking both iron centers (*i.e.*, one of the two thiolate groups in each monomer binds to the iron center in the other, connecting both monomers). In addition, the imine groups of each tridentate ligand were transformed into a diamido unit, creating a new C—C bond between initial $[S^{Me}N^{H}S]$ ligands. As

result, a new redox-active $(N_2S_2)^{2-}$ ligand with two uncoordinated thioether groups was formed (Scheme 4.6)

Scheme 4.6 Synthesis of dimeric complex **5** in solid state (left) and its monomeric form obtained in solution **6** (right).

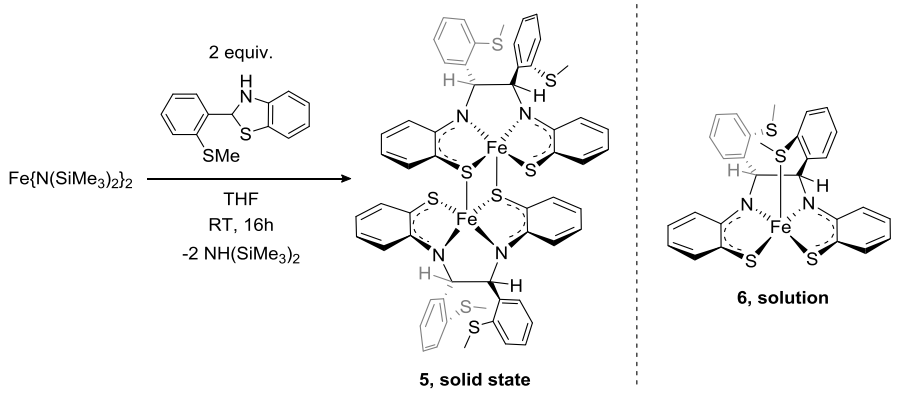

Complex **5** is a dimer in the solid state, but a new monomeric species **6** is obtained in solution (CD_2Cl_2, THF-d_8 and C_6D_6). The monomeric form of **5** retains the square pyramidal coordination and the magnetic properties on the metal, due to the coordination of the thioether group to the paramagnetic iron center (Figure 4.1).

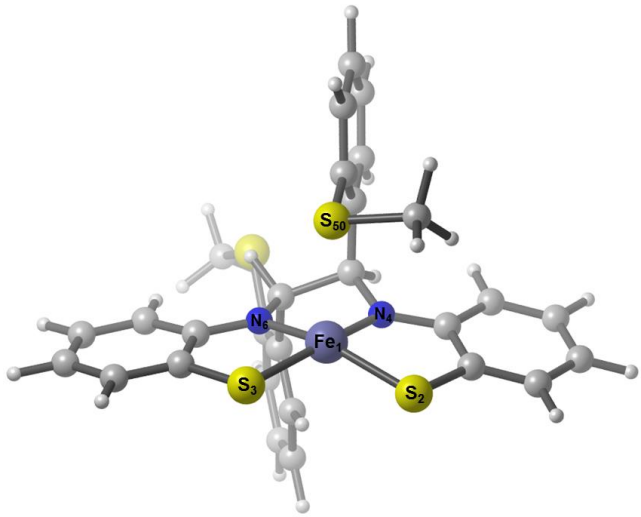

Figure 4.1 X-ray structure of complex **6**. Labels indicated for selected atoms.

The dimeric structure **5** is not observed in any solvent. Complex **6** is able to react upon addition of $P(OMe)_3$ or CO. In the first case, the iron center coordinates the new ligand in the axial position by decoordinating the thioether group. Consequently, the new complex $[Fe(N_2S_2)P(OMe)_3]$ (**7**) becomes diamagnetic. In the second case, the coordination of the CO generates a new unexpected complex **8** (Scheme 4.7). The X-ray data for this transformation showed that carbonylation of monomeric complex **6**, cleaves the diamido C—C bond, generating an octahedral iron complex [Fe(κ^3 -SNS)(κ^2 -SNS)CO] (**8**) (Scheme 4.7).[47] This new complex **8** is diamagnetic in CD_2Cl_2 but, interestingly, the ^{1}H NMR spectrum also shows the signals for the paramagnetic complex **6.** This is indicative of an equilibrium between **6** and **8** upon addition of the CO ligand.

Scheme 4.7 Reactivity of complex **6** upon addition of different coordinating ligands ($P(OMe)_3$, left and CO, right).

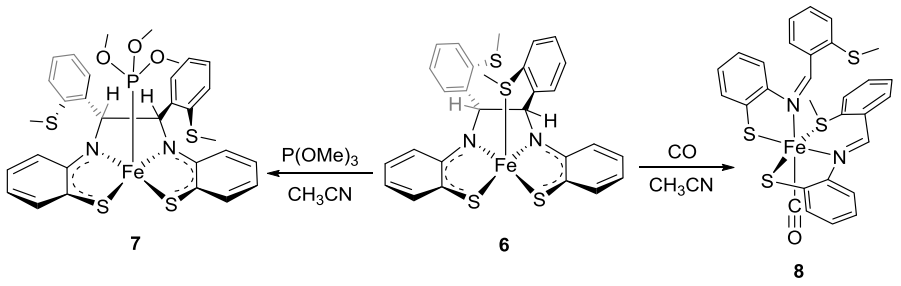

Complex **6** was then tested for the catalytic hydroboration of aldehydes.[47] Hydroboration of carbonyl compounds can be achieved with several transition metal-based complexes (Ti,[48,49] Mo,[50] Fe,[51] Ru,[52] Co,[53] and Cu[54]). Main group metals (Li,[55] Mg,[56,57] Ca,[58] Al,[59,60] Ga,[61] Zn,[62,63] and Sn [64]) and main groups elements (P),[65] are also known to catalyze this reaction. However, the selective hydroboration of aldehydes over ketones has only few examples in the literature.[51,52,60,65] In this regard, Baker and co-workers reported that complex **6** is able to selectively catalyze the hydroboration of aldehydes at low catalysts loading (0.1 mol%) at room temperature

using HBpin as boron source. In addition, the reaction tolerates a wide range of functionals groups including nitriles, amines, alkenes, halides and ketones, even at higher temperatures.

In this chapter 4, we will present the computational work carried out in a collaboration with Baker's group in the University of Ottawa. The chapter is divided in two main sections. The first one (section 4.3) focuses on the elucidation of the intrinsic electronic structure of complex **6** and its cationic $\mathbf{6}^{+}$ and anionic $\mathbf{6}^{-}$ analogues. Our efforts will be focused on the analysis of the redox non-innocent character of the $(N_2S_2)^{2-}$ ligand. In addition, the results for the DFT characterization of complex **7** and **8** will be discussed. The other section will be dedicated to the computational elucidation of a possible mechanism for the hydroboration of aldehydes carried out by complex **6**.

Characterization of transition metal complexes is an important tool in chemistry. It can give knowledge and understanding on the intrinsic features of the complexes and hence, on methods to improve their performance towards a particular transformation. With computational tools we can examine in depth the electronic structure of complexes bearing non-innocent ligands which directly affect the redox properties of the whole complex.

Overview of the experimental data

In this section, we present the experimental characterization by Baker and co-workers of the neutral Fe(II) complex **6**, together with their anionic $\mathbf{6}^{-}$ and cationic $\mathbf{6}^{+}$ analogues. The X-ray crystal structure obtained for complex **6** is presented in Figure 4.1. The structure shows the imine coupled through a C—C bond with one thioether group coordinated to the iron center on an axial position. The measured solid-state 80 K Mössbauer parameters for complex **6** are 0.15 mm/s for the isomer shift (δ) and 2.83 mm/s for the quadrupole splitting (ΔE_Q) (Figure 4.2). These values are consistent with a high spin Fe(II) species. In addition,

the solution magnetic moment measured by the Evans method [66] is 2.7 μ_B, consistent with two unpaired electrons.

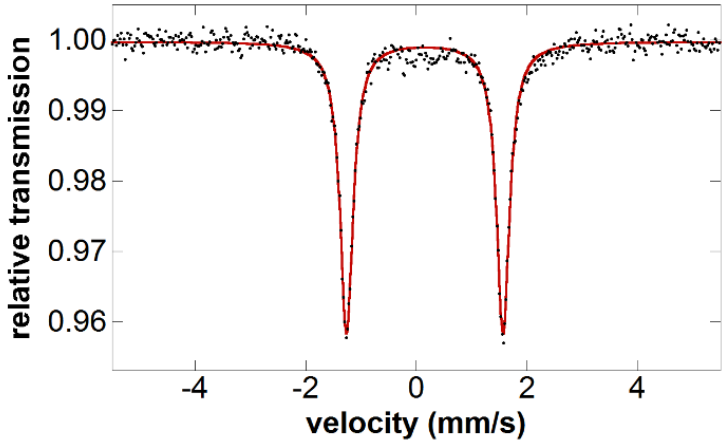

Figure 4.2 ^{57}Fe Mössbauer spectrum of complex **6**.

Electrochemical studies were then performed on complex **6**. Similar ligand frameworks are known to act as redox non-innocent ligands by accepting or donating electrons.[67,68] Thus, complex **6** was subjected to detailed electrochemical analysis in THF. The cyclic voltammetry showed two important potential waves for the one-electron reduction and oxidation processes. The waves were found at $E_{1/2}^{1}$ = -0.60 V and $E_{1/2}^{2}$ = 0.05V, respectively. In addition, the reversibility found for both waves indicated that the chemical environment remains intact after reduction or oxidation of the complex. No chemical transformation occurs after the redox processes.

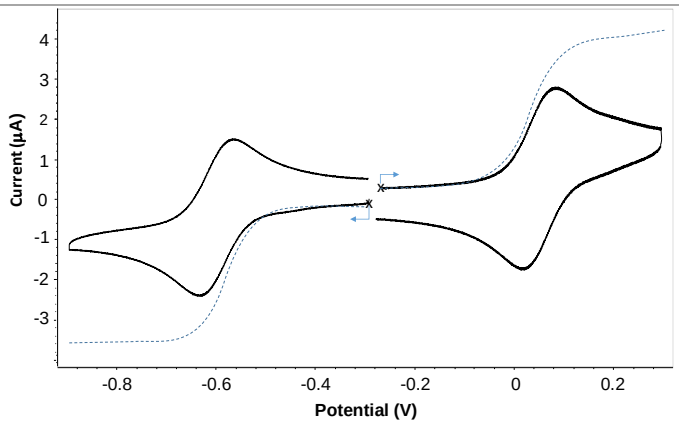

Figure 4.3 Cyclic voltammetry curves recorded under argon atmosphere for complex **6** ($1 \cdot 10^{-3}$ M in THF + 0.1 M NBu_4PF_6) at (solid line) a stationary vitreous carbon working electrode (Ø = 3 mm, E vs Ag/Ag^+ (10^{-2} M), v = 0.1 $V \cdot s^{-1}$) and (dotted line) at a rotating carbon disk electrode (Ø = 3 mm, v = 0.01 $V \cdot s^{-1}$, 550 rd/min).

Further electrochemical experiments such as electrolysis or spectroelectrochemistry were performed in order to gain more insight on the redox processes of complex **6**. Electrolysis of the cationic and anionic form showed a remarkable stability of both complexes under exhaustive potentials. On the other hand, the interconversion of **6** to $\mathbf{6}^-$ or $\mathbf{6}^+$ was followed by UV-vis spectra during the electrolysis of the complexes (Figure 4.4).

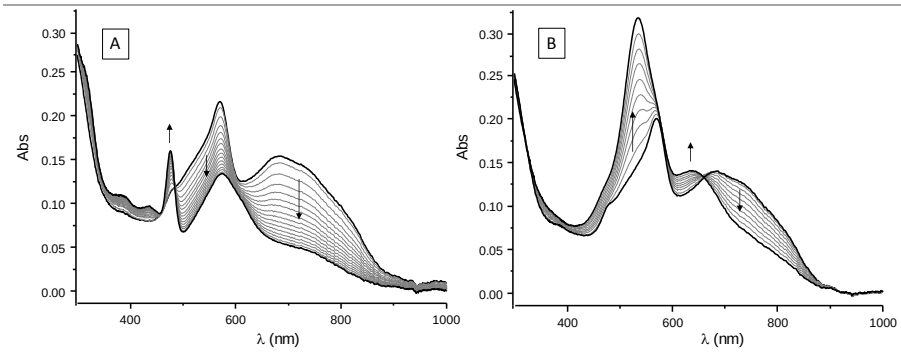

Figure 4.4 UV/Vis spectra recorded during the electrolysis (one electron per molecule) of **6** (x mol L^{-1}) at A) E_{app} = — 1V and B) E_{app} = +0,5V in THF (0.1 M TBAP) (working electrode : Pt, l = 1 mm).

Complex **6** and its redox partners **6**$^{-}$ and **6**$^{+}$ were also characterized by EPR spectroscopy. The iron complex **6** was found to be EPR silent. The results for complex **6**$^{-}$ showed a weak signal at g= 5.1, suggesting the presence of traces of a high-spin iron(I) species.[69] Figure 4.5 presents the X-band EPR spectrum of complex **6**$^{+}$. The results are consistent with a low-spin (S=½) Fe(III) species, with three intense signals at g= 2.191, 2.075 and 2.021. In addition, the simulated spectrum of the cationic complex **6**$^{+}$ was obtained using easyspin [70] and an excellent agreement was found with the experimental signals (Figure 4.5 in red).

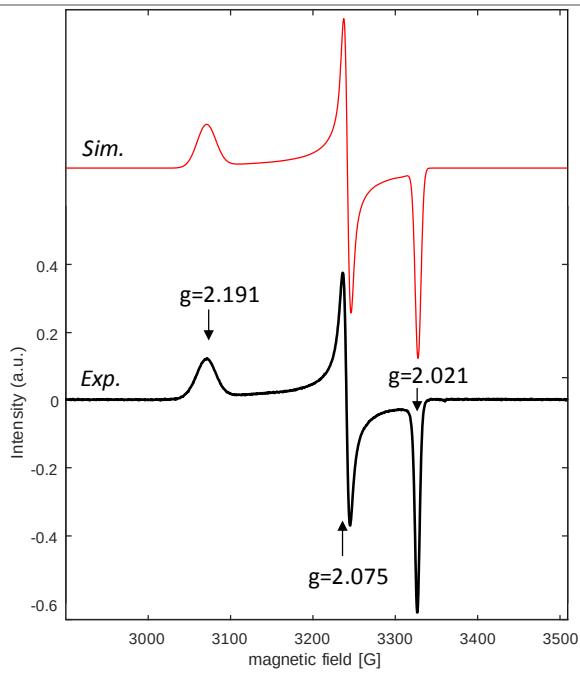

Figure 4.5 Simulated (red) and experimental EPR spectrum of complex 6+ recorded at 110 K (microwave power; 6mW; modulation amplitude; 2G).

Each redox partner of complex **6** was then synthetized independently in order to further investigate their intrinsic characteristics. Electrochemical potentials found for the reduction/oxidation of **6**, helped to choose which oxidant o reductant reagent was appropriate to achieve its

redox partners. Thus, a solution of sodium napthalenide (NaNp) in THF was added to a solution of complex **6**. The proper choose of the sodium cation was key to successfully achieve the X-ray quality crystals of the reduced complex **6**$^-$. As expected, the structure of the complex remains the same as in complex **6,** with the thioether coordinated to the metal center (Scheme 4.8). The effective magnetic moment of **6**$^-$ measured by the Evans method reports a value of 3.5 μ_B. This value is consistent with a quartet (S = 3/2) Fe(I) species with 3 unpaired electrons.

Scheme 4.8 Synthesis of anionic complex **6**$^-$, $[Fe(N_2S_3)]^-$.

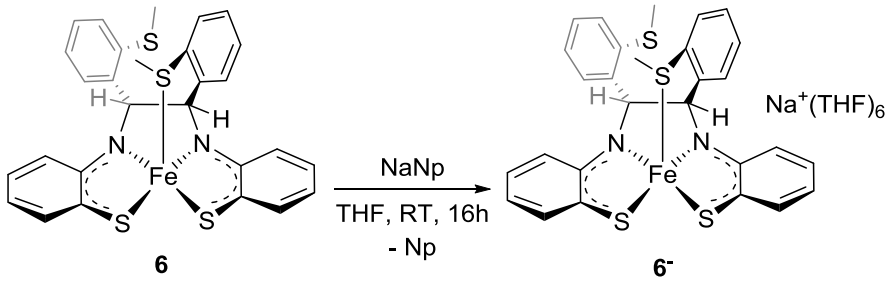

Lastly, the synthesis of the cation **6**$^+$ was found to be much more problematic. All the first attempts to synthesize this complex gave multiple products on the ^{1}H NMR spectrum and Evans method measurements, consistent with the apparition of impurities or incomplete oxidation. Several oxidizing agents were tested such as silver salts, aminium cations or copper triflate in a variety of solvents. Finally, the addition of stochiometric $NOBF_4$ to complex **6** in CH_2Cl_2, afforded the desired complex in 24 hours (Scheme 4.9). The Evans method showed a value of 1.5 μ_B for the effective magnetic moment of complex **6**$^+$, indicating the presence of a doublet Fe(III) species (S = ½).

Scheme 4.9 Synthesis of anionic complex $\mathbf{6^+}$, $[Fe(N_2S_3)]^+$.

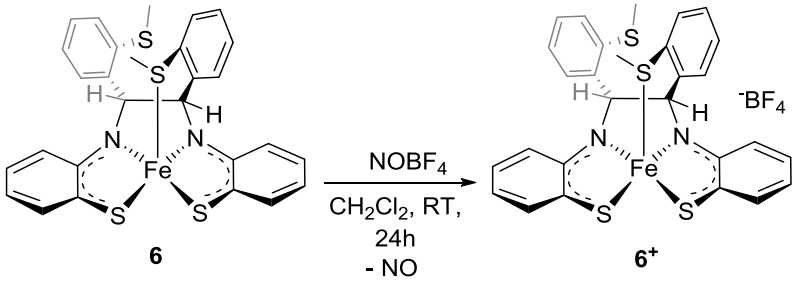

As mentioned in the previous subsection, complex **6** was able to effectively catalyze the hydroboration of several aldehydes.[47] Here, we will introduce the more interesting results as well as the experimental insight on a plausible mechanism. The optimal reaction conditions were found to involve a 0.1 mol% of complex **6** as catalyst in C_6D_6 solvent, with one equivalent of HBpin for the hydroboration of benzaldehyde. The hydroborated product was achieved in quantitatively yields within 0.5 hours at room temperature (Table 4.1). Interestingly, while the purple solution of **6** was unchanged upon addition of benzaldehyde, once HBpin was added, the color changed quickly to light beige or colorless. This demonstrates that HBpin activates the catalysts and complex **6** is a mere precatalyst of the reaction.

Several alternative Fe(II) complexes were tested (e.g. $FeCl_2$, $Fe(OTf)_2$, or $Fe\{N(SiMe_3)_2\}_2$), although they gave lower yields together with the formation of a dark precipitate. Replacement of benzaldehyde by acetophenone afforded less than 5% of the hydroboration product, indicating the high selectivity of **6** towards aldehydes. This was further confirmed when using 4-acetylbenzaldehyde as reactant. Only the aldehyde group became hydroborated with excellent yields (>99).

Table 4.1 Optimization of reaction conditions for the hydroboration of benzaldehyde.

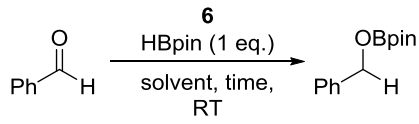

catalyst (mol %)	solvent	time (h)	yield (%)
6 (0.1)	C_6D_6	0.5	>99
$FeCl_2$ (0.5)	C_6D_6	0.5	35
$Fe(OTf)_2$ (0.5)	C_6D_6	0.5	51
$Fe\{N(SiMe_3)_2\}_2$ (0.5)	C_6D_6	0.5	20
6 (0.1)	THF-d_8	0.5	95
6 (0.1)	CD_3CN	0.5	>99

Regarding the possible mechanism, kinetic studies to identify the resting state and substrate dependence were performed. 4-methylbenzaldehyde was selected to run the measurements because it is a less reactive aldehyde. Unfortunately, these studies were not very informative, as no resting states or intermediates could be observed. However, some information could be extrapolated from the kinetic results. The results suggest a positive order in both reactants (aldehyde and HBpin). The precise order could not be determined because the progress of the reaction changes dramatically when changing to excess (red and yellow dots, in Figure 4.6) or equimolar starting materials (blue dots in Figure 4.6).

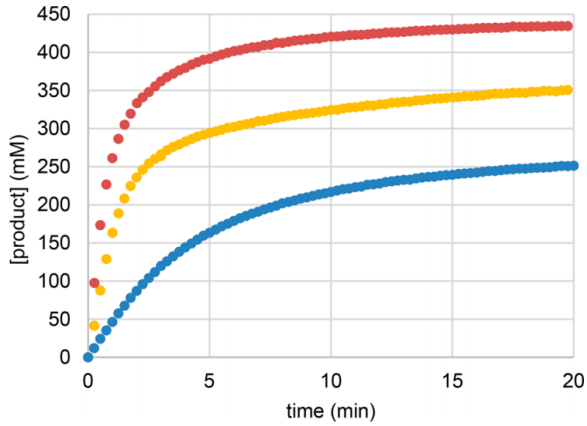

Figure 4.6 Effect of the concentration on the formation rate of product in the hydroboration of 4-methylbenzaldehyde catalyzed by **6**. ([**6**] = 0.44 mM, RT, C_6H_6; in blue [CHO] = [HBpin] = 450 mM; in red [CHO] = 450 mM and [HBpin] = 675 mM; in yellow [CHO] = 675 mM and [HBpin]) 450mM). From ref [47].

The concentration of each reactant was monitored during the catalysis (Figure 4.7). The consumption rate of HBpin was found to be higher than that for the aldehyde. However, no obvious byproducts were found accounting for the extra consumption of the HBpin. This suggest that HBpin first activates the precatalyst **6**, in agreement with the color change found upon addition of it to the iron complex.

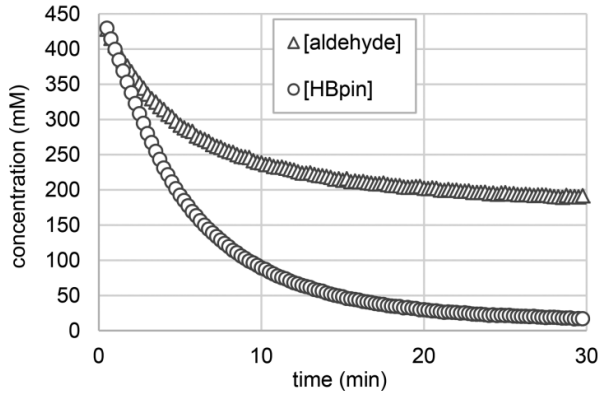

Figure 4.7 Rates of consumption for aldehyde and HBpin in the hydroboration of *p*-methylbenzaldehyde catalyzed by **6** ([**6**] = 0.44 mM, RT, C_6H_6, [CHO] = [HBpin] = 450 mM). From ref [47].

4.2 Computational details

Computational method

All the energy and structural calculations reported in this chapter were carried out with the Gaussian09 (rev. D.01) package [71] using density functional theory (DFT). For section 4.3 and 4.4 the B3LYP-D3 level of theory was selected.[72] D3 stands for Grimme-D3 dispersion correction.[73] This functional was chosen after an extensive benchmarking in order to determine which one could reproduce better the relative energies and the X-ray structure for the different complexes under study. The results of this benchmark will be detailed in the next subsection.

Experimental solvents (benzene: ε=2.2706 and acetonitrile: 35.688, the later for the calculations on complex **8**), were introduced implicitly in all the calculations through the SMD model.[74] All the structures were optimized without symmetry restrictions. 6-31+G(d) basis set for light atoms (C, H, N, S, B, O, P) [75] and LANL2DZ [76] and its corresponding pseudopotential for Fe atoms were used for optimizations and frequency calculations.

The nature of the stationary points was assigned to a minima (zero imaginary frequencies) or transition states (one imaginary frequency) by vibrational frequency calculations. All the reported energies in section 4.3 are potential energies in solution, as they correspond to a discussion on electronic states. The energies shown in section 4.4 are free energies in solution (unless otherwise noted) calculated at 298.15 K and 1 atm in $kcal \cdot mol^{-1}$, as they correspond to chemical reactions.

Some calculations showed spin contamination for the optimized structure. The Yamaguchi spin correction formula was applied in all the calculations in section 4.3 to account for this spin contamination (see Chapter 2).[77]

Mössbauer parameters were calculated for complexes **6**, **6**$^{-}$ and **6**$^{+}$, using the ORCA (version 4.0) package [78] with the B3LYP-D3 level of theory.[72,73] The Mössbauer parameters were obtained by approximating the solid-state effects by modeling methanol (ε=32.613) with CPCM as implicit solvent model.[79] This is a common approach for modeling the effect of the condensed phase of the molecular environment.[80] The basis set def2-TZVPP together with the core properties basis set CP(PPP) was employed to increase the radial integration accuracy for the iron atom.[81] The computed isomer shift (δ) were obtained using the linear equation $\delta = \alpha(\rho - C) + \beta$.[82]

All the 3D structures on section 4.3 and 4.4 were drawn with CYLview program,[83] and the orbital representations on section 4.3 were drawn with Chemcraft program.[84] The coloring criteria for atoms is always the same: white for H, grey for C, yellow for S, blue for N, red for O, orange for P, pink for B and purple for Fe.

Benchmarking of the computational method

The selection of the adequate functional for DFT calculations is a key point in a computational study. The selection of an inappropriate functional for a given problem, could lead to a miss-matching between experimental and computational results. This is especially tricky when different spin states may be involved. Because of this, an extensive benchmarking of DFT functionals was carried out.

We selected B3LYP-D3,[72] M06-L-D3,[85] M06-D3,[85] M06-2X-D3,[85] OPBE,[86] ωB97xD,[87] and BP86.[88] Several electronic spin states were calculated (closed-shell singlet, open-shell singlet, triplet and quintet) to compare the results with the experimental magnetism reported. We chose complexes **6**, **7** and **8** to perform the benchmark calculations. In order to not encumber this section with too many tables, only the results for complex **6** will be shown, as they are representative.

Table 4.2 Potential energies for different spin states of complex **6** with several DFT functionals. Energies are in kcal·mol^{-1}.

Functional	Closed-shell singlet	Open-shell singlet	Triplet	Quintet
B3LYP-D3	0.0	-5.0	-12.1	-4.3
M06-L-D3	0.0	-22.3	-29.8	-23.2
M06-D3	0.0	-30.0	-49.0	-40.3
M06-2X-D3	0.0	-	-78.6	-43.9
OPBE	0.0	-	-2.2	8.8
ωB97X-D	0.0	-	-18.3	-12.0
BP86	0.0	-	-0.2	12.5

The results for the energy comparison between the four different spin states of complex **6** are shown in Table 4.2. For some functionals we were not able to find the open-shell singlet structure. In those cases, all our attempts fell to the closed shell singlet spin state. We covered an extensive range of functionals including different levels of HF exchange. All the results point towards the triplet spin state as the ground state which agrees with the experimental data. Two functionals with no HF exchange (OPBE and BP86) seem to underestimate the stability of the triplet state, as they place the singlet state almost equal in energy. In contrast, the M06-L-D3 functional finds the triplet state almost 30.0 kcal·mol^{-1} lower than the closed-shell singlet state. Hybrids functionals report a higher energy difference between the triplet and the singlet spin states. The results with the functionals in the M06 family confirm the well-known relationship between the % of HF exchange and the stabilization of the triplet spin state. However, for this particular system, the M06 family favors very much the triplet state with respect to the singlet. For instance, M06-D3 has a similar exact HF exchange to B3LYP-D3 (27% and 22%, respectively), but the relative energies found for both functionals differ by more than 30.0 kcal·mol^{-1}. ωB97X-D and B3LYP-D3 produce quite similar results although the dispersion term used in each functional is different (ωB97X-D uses the D2 version of Grimme's dispersion).[89] This suggest that the dispersion terms do not have a

huge impact on the energy calculation for these systems. We have to admit in any case that the comparison of the relative energies is not conclusive on functional quality, as all of them predict a triplet ground state, in agreement with experiment.

We next analyzed the optimized structures with each functional, for all the spin states, and we compared it with the experimental X-ray values for complex **6**. The results are summarized in Table 4.3.

Table 4.3 Selected bond distances for the comparison between the experimental values and the DFT optimized values for all the functionals included in the benchmark. Labels correspond to those on Figure 4.1. Distances in Å.

		d(Fe_1-S_{50})	**d(Fe_1-S_2)**	**d(Fe_1-S_3)**	**d(Fe_1-N_4)**	**d(Fe_1-N_6)**
Experimental		2.5267	2.2319	2.2287	1.8635	1.8657
B3LYP-D3	css	2.2477	2.2396	2.2497	1.8563	1.8652
	oss	2.4225	2.2733	2.2825	1.8873	1.8962
	t	2.6075	2.2458	2.2774	1.8446	1.8835
	q	2.7020	2.2925	2.2795	1.9082	1.8887
M06-L-D3	css	3.5087	2.1865	2.1843	1.8062	1.7955
	oss	2.2368	2.2268	2.2364	1.8507	1.8693
	t	2.6217	2.2385	2.2398	1.8557	1.8674
	q	2.2622	2.2613	2.2642	1.8839	1.8885
M06-D3	css	2.1950	2.2008	2.2096	1.8323	1.8435
	t	2.6004	2.2183	2.2475	1.8332	1.8835
	q	2.6227	2.2166	2.2909	1.8394	1.9368
M06-2X-D3	css	3.5256	2.2362	2.2494	1.8352	1.8330
	t	2.5640	2.4756	2.4682	2.1104	2.1329
	q	2.6563	2.3098	2.3038	1.9011	1.9023
OPBE	css	2.1369	2.1637	2.1725	1.8157	1.8376
	t	2.5843	2.1919	2.1928	1.8218	1.8407
	q	2.5912	2.2316	2.2365	1.8593	1.8669
ωB97X-D	css	2.2387	2.2131	2.2225	1.8313	1.8412
	t	2.5742	2.2838	2.2247	1.8910	1.8339
	q	2.6052	2.2333	2.3117	1.8302	1.9462
BP86	css	2.1962	2.2093	2.2217	1.8526	1.8662
	t	2.5618	2.2193	2.2247	1.8414	1.8510
	q	2.5994	2.2555	2.2574	1.8776	1.8846

The best agreement for the three complexes included on the benchmark (**6**, **7** and **8**) was found with the B3LYP-D3 functional. We have to admit that the agreement is not excellent, in particular for the Fe—S distances.

Computational model

For some calculations in section 4.4, we used a smaller model of the system in order to reduce the computational cost. Thanks to the characterization of the system, we could design the model in a rational manner where the intrinsic electronic structure was not altered. The modification will be addressed in due time during section 4.4.

4.3 Characterization

$[Fe(N_2S_3)]^0$ complex and its redox partners

We started our DFT investigation with the study of complex **6**. As mentioned in the introduction of this chapter, the experimental data propose this complex to be a paramagnetic Fe(II) species, with two unpaired electrons. We ran geometry optimizations for the different spin states: closed shell singlet, open shell singlet, triplet and quintet spin states. The computed energies are summarized in Table 4.4.

Table 4.4 Corrected potential energies (in kcal·mol^{-1}) for the different spin states considered for complex **6**.

Spin state	Corrected Pot. Energy
Closed-shell singlet	0.0
Open-shell singlet	12.0
Triplet	-11.4
Quintet	-4.3

The triplet spin state was found as the ground state 11.4 kcal·mol^{-1} below the closed shell singlet state after applying the Yamaguchi spin correction formula. The open shell singlet and the quintet state were

found to lie at 12.0 and -4.3 kcal·mol^{-1}, respectively, from the closed shell singlet state.

In order to analyze the spin distribution of the complex in each spin state, we decided to divide it into the three fragments shown in Figure 4.8. The three fragments are: the metal center (in black), the right-hand side of the ligand (L1(SNS), in green) and the left-hand side of the ligand (L2(SN), in purple). We then added up the Mulliken spin population in the atoms of each fragment. This separation helped as to localize the spin population in different parts of the molecule and hence, to gain more information on the electron distribution.

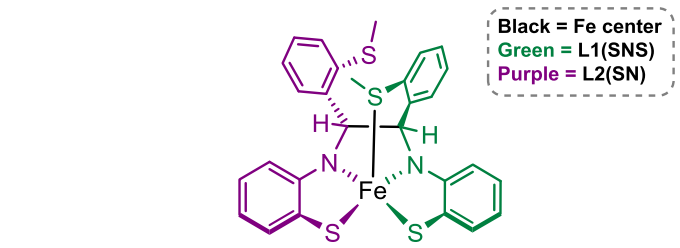

Figure 4.8 Fragments considered to analyze the spin density of **6** and its redox partners.

The results of the Mulliken spin distribution analysis are summarized in Table 4.5. Remarkably, for the ground state triplet the results show more than two open shells. Two alpha electrons are localized in the metal center, with an extra alpha electron delocalized between L1(SNS) and the Fe center, with a greater contribution on the metal center. In addition, a beta electron is mostly localized on the L2(SN) fragment of the complex (-0.70).

Table 4.5 Spin density values obtained for each fragment in different spin calculations for complex **6**.

Spin density	Open-shell singlet	Triplet	Quintet
Fe	1.64	2.54	2.40
L1(SNS)	-0.86	0.16	0.80
L2(SN)	-0.78	-0.70	0.80

We also carried a comparison between the optimized structure and the experimentally obtained X-ray structure. Results are summarized in Table 4.6. The parameter presenting the larger discrepancies from one spin state to the other is the Fe_1-S_{50} distance, with a range from 2.2477 Å in the closed-shell singlet to 2.7020 Å in the quintet. The experimental value 2.5267 Å is closer to the value for the triplet, 2.6075 Å. We consider this as further proof of the correctness of the description for this system.

Table 4.6 Experimental and calculated selected bond distances (in Å) for complex **6**. Labels correspond to those shown in Figure 4.1.

	X-ray values	Calculated			
Bond		**Closed-shell singlet**	**Open-shell singlet**	**Triplet**	**Quintet**
d(Fe_1-S_{50})	2.5267	2.2477	2.4225	2.6075	2.7020
d(Fe_1-S_2)	2.2319	2.2396	2.2733	2.2458	2.2925
d(Fe_1-S_3)	2.2287	2.2497	2.2825	2.2774	2.2795
d(Fe_1-N_4)	1.8635	1.8563	1.8873	1.8446	1.9082
d(Fe_1-N_6)	1.8657	1.8652	1.8962	1.8835	1.8887

The next complex studied in our DFT characterization was the reduced species $\mathbf{6}^-$. We followed the same methodology. In this case, three different spin states were considered: doublet, quartet and sextet. The relative potential energies for these states are summarized in Table 4.7. The quartet spin state was found to be the ground state for complex $\mathbf{6}^-$, with the doublet and the sextet at 8.0 and 6.2 kcal·mol^{-1}, respectively, above it.

Table 4.7 Corrected potential energies (in kcal·mol^{-1}) for the different spin states considered for complex **6**$^{-}$.

Spin state	Corrected Pot. Energy
Doublet	0.0
Quartet	-8.9
Sextet	-2.7

The analysis of the spin distribution for the different spin states of complex **6**$^{-}$ is shown in Table 4.8. For the quartet ground state, the results reveal three alpha electrons mostly localized on the Fe center. One electron is a little delocalized among both sides of the ligand, 0.13 and 0.16 spin density on L1(SNS) and L2(SN), respectively. The comparison between the spin density distribution of the ground states of **6** and **6**$^{-}$ shows that the reduction from **6** to **6**$^{-}$ is mostly ligand based. The Fe center remains almost with the same spin density before (2.71) and after (2.54) the reduction process, but the L2(SN) side of the ligand changes from -0.70 to 0.16. The added electron is thus placed in the L2(SN) fragment of the ligand. This is a computational confirmation of the redox non-innocent nature of the ligand.

Table 4.8 Spin density values obtained for each fragment in different spins states for complex **6**$^{-}$.

Spin density	Doublet	Quartet	Sextet
Fe	1.03	2.71	3.95
L1(SNS)	-0.09	0.13	0.47
L2(SN)	0.05	0.16	0.58

The results for the experimental/computational structure comparison for complex **6**$^{-}$ are shown in Table 4.9. As for complex **6**, the larger discrepancy between spin states is found for the distance Fe_1-S_{50}. In this case, the best agreement for this particular distance is found for the sextet state instead of the ground state. Nevertheless, the selected distances point toward the correct assignment of quartet spin state as the ground state because it better reproduces the whole complex. The sextet spin

state shortens the Fe—S distance on the axial position, as expense of enlarging the Fe—S and Fe—N distances on the equatorial positions and moving them far from the experimental values.

Table 4.9 Experimental and calculated selected bond distances (in Å) for complex $\mathbf{6}^{-}$. Labels correspond to those shown in Figure 4.1.

	X-ray values	Calculated		
Bond		**Doublet**	**Quartet**	**Sextet**
d(Fe-S_{50})	2.5601	2.2731	2.6508	2.5956
d(Fe-S_2)	2.2267	2.2882	2.2855	2.4148
d(Fe-S_3)	2.2261	2.2899	2.2809	2.4171
d(Fe-N_4)	1.8590	1.8760	1.8670	1.9945
d(Fe-N_6)	1.8762	1.8829	1.8725	1.9943

Finally, we studied the electronic structure of the cationic complex $\mathbf{6}^{+}$. We found the doublet spin state to be the ground state. The quartet and sextet spin states were found at 14.8 and 27.4 kcal·mol^{-1}, respectively, from the doublet state, after applying the Yamaguchi spin correction formula. These results agree with the experimental Evans method measurements which suggest the formation a doublet (S = ½) ground state for complex $\mathbf{6}^{+}$. The potential energies for each spin state are shown in Table 4.10.

Table 4.10 Corrected potential energies (in kcal·mol^{-1}) for the different spin states considered for complex $\mathbf{6}^{+}$.

Spin state	**Corrected Pot. Energy**
Doublet	0.0
Quartet	14.8
Sextet	27.4

The spin distribution of the spin states under study for complex $\mathbf{6}^{+}$ is shown in Table 4.11. The doublet ground state shows approximately three alpha electrons on the iron center (2.54). In addition, each side of the ligand presents negative spin density which can be attributed as one beta electron in each fragment of the ligand (-0.74 and -0.79, for

L1(SNS) and L2(SN), respectively). Again, the comparison between the spin density distribution of complexes **6** and **6**$^{+}$ suggests that the oxidation from **6** to **6**$^{+}$ is ligand based. The Fe center keeps the same spin density after the oxidation process (2.54 for both redox states), while the spin density on the L1(SNS) fragment changes from 0.16 to -0.74, indicating the loss of one electron on this side of the ligand.

Table 4.11 Spin density values obtained for each fragment in different spins states for complex **6**$^{+}$.

Spin density	Doublet	Quartet	Sextet
Fe	2.54	2.69	2.92
L1(SNS)	-0.74	-0.62	1.11
L2(SN)	-0.79	0.93	0.97

The selected bond distances obtained on the geometry optimizations calculations for the different spin states of complex **6**$^{+}$ are summarized in Table 4.12. Unfortunately, during the preparation of this thesis manuscript, the X-ray determination of the structure of this complex had not yet been achieved. Interestingly, the distances for the Fe—S bonds on the equatorial plane can be directly related with the spin density found for each side of the ligand in each spin state. In general, the fragments presenting beta spin density feature shorter Fe—S and Fe—N bond distances that those with alpha spin density. We believe that this can be associated to the attraction or repulsion generated between the opposite or parallel disposition of the electrons, respectively, in each fragment of the ligand.

Table 4.12 Calculated bond distances (in Å) for complex $\mathbf{6^+}$. Labels correspond to those shown in Figure 4.1.

	Calculated		
Bond	**Doublet**	**Quartet**	**Sextet**
d(Fe-S_{50})	2.4769	2.5502	2.6376
d(Fe-S_2)	2.2540	2.2510	2.2904
d(Fe-S_3)	2.2574	2.2727	2.2890
d(Fe-N_4)	1.8743	1.8774	1.9088
d(Fe-N_6)	1.8791	1.9259	1.9210

DFT-Mössbauer parameters were calculated in order to further characterize the intrinsic complicated electronic structure of these complexes. The results are summarized in Table 4.13. The differences between the experimental and the computed parameters are inside the expected range.[82,90] The results obtained for complex **6**, fit well with the experimental values. Although it is worth mentioning, that due to the similar spin density found on the Fe center of complex **6** in its triplet and quintet spin states (2.54 and 2.40, respectively), it is not trivial to determine which calculated parameters fit better with the experimental findings.

Table 4.13 DFT-calculated Mössbauer parameters: isomer shift (δ) and quadrupole splitting (ΔE_Q), for $\mathbf{6^-}$, **6** and $\mathbf{6^+}$ complexes. Experimental values are provided for comparison. Some of the computed values for ΔE_Q are negative, even if experiment can only measure the absolute value.

		δ [mm s^{-1}]		**ΔE_Q [mm s^{-1}]**	
Complex	**$S_{complex}$**	**Exp.**	**Calc.**	**Exp.**	**Calc.**
6^-, $Fe[N_2S_3]^-$	½		0.23		2.90
	3/2		0.17		3.46
	5/2		0.39		-1.80
6, $Fe[N_2S_3]^0$	0		0.16		3.42
	1	0.15	0.13	2.83	3.39
	2		0.25		2.81
6^+, $Fe[N_2S_3]^+$	½		0.13		3.29
	3/2		0.15		3.53
	5/2		0.17		4.13

Natural orbital analysis for $[Fe(N_2S_3)]^0$ and its redox partners

In this section we will introduce the results for the natural orbital analysis for the frontier orbitals of the ground spin state of each redox partner. This study will allow us to better understand the electronic structure of the complexes by comparing the shape of the orbitals for each redox state. In addition, thanks to the electron occupancy of each orbital, we will be able to estimate the oxidation state of the metal center and hence, the redox characteristics of the ligand.

It is worth noting that the appearance of extra open shells on the complexes makes the analysis of these orbitals much more complicated. Nevertheless, we were able to identify the five d orbitals of the metal for all the complexes, together with three orbitals of the ligands which are responsible of the redox activity. In order to have a more clear analysis, we will present first the orbital analysis of complex **6**$^-$. This system does not present any extra open shell and hence, the explanation is easier.

The calculated S^2 value for complex **6**$^-$ was 3.80. This is very similar to the ideal value for a pure quartet spin state (3.75). The orbital analysis showed three semi-occupied orbitals almost fully localized on the metal center: orbitals d_{xz}, d_{z2} and d_{yz}. From the occupancies we can deduce that the metal center has only five electrons (Figure 4.9). So, we assign an oxidation state of +3 to iron, and -4 to the ligand.

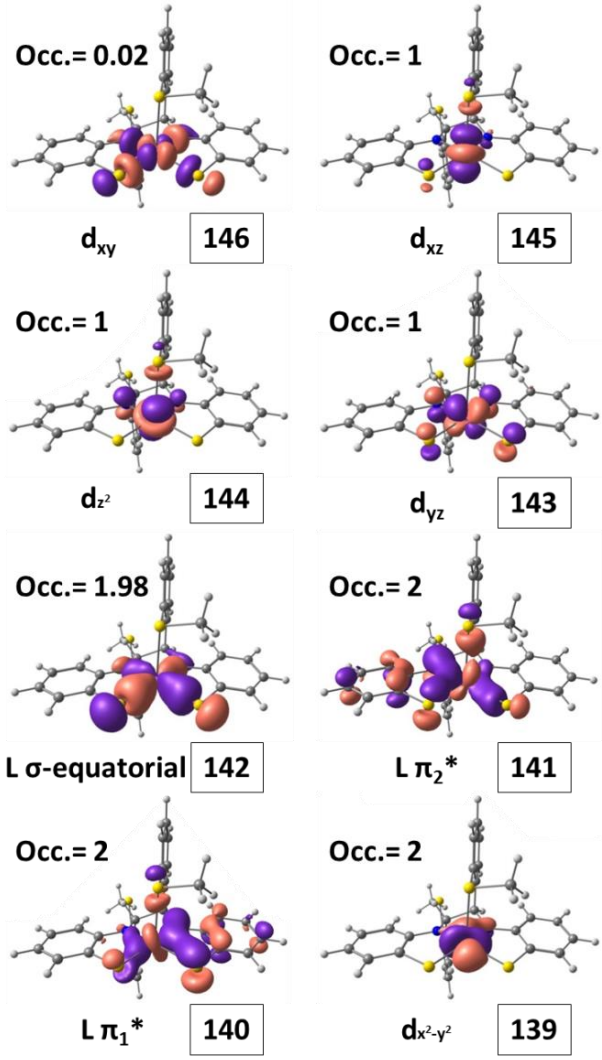

Figure 4.9 Frontier orbitals for complex **6**$^-$.

For complex **6**, the calculated S^2 value was 2.60. This result is far from the ideal value for a pure triplet state (2.00), and is indicative of the presence of extra open shells in the complex. We can observe in Figure 4.10 two orbitals mainly localized on the metal center, 144 and 143, corresponding to the d_{xz} and d_{z2} orbitals of the metal, respectively. The latter has some contribution from the axial thioether group of the L1(SNS) side of the ligand. This could explain the small spin density

found on the calculations (0.16). Orbitals 142 and 145 correspond to the bonding and anti-bonding interactions between the d_{xy} orbital and the π^* orbital of the L2(SN) fragment. The calculations report 1.67 and 0.33 occupancies for these orbitals, respectively. The contributions of the spin density in orbital 142 are larger for the Fe center than for the ligand fragment. In contrast, the shape of the orbital 145 shows larger lobes on the ligand (see Figure 4.10).

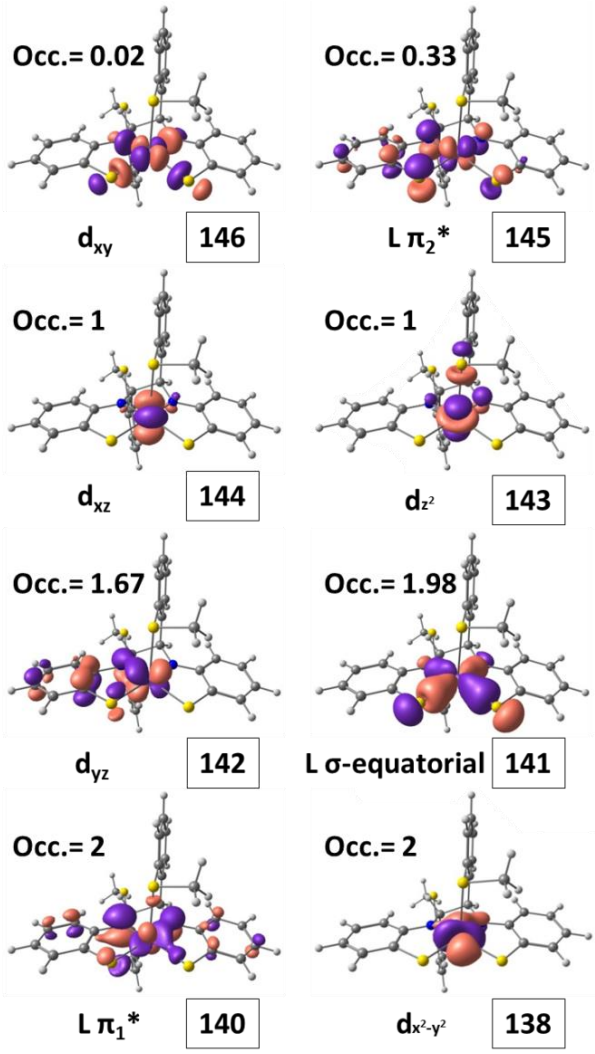

Figure 4.10 Frontier orbitals for complex **6**.

In summary, by comparison with the orbitals of complex **6**$^{-}$, the one-electron oxidation from **6**$^{-}$ to **6** is ligand based. Specifically, an electron is released from the L2(SN) side of the ligand. Then, the system stabilizes its electronic structure by merging the d_{xy} and the π_2* orbital, where the metal is partially oxidized from the ligand. Consequently, the metal remains in an oxidation state between Fe(II) and Fe(III), but closer to Fe(III).

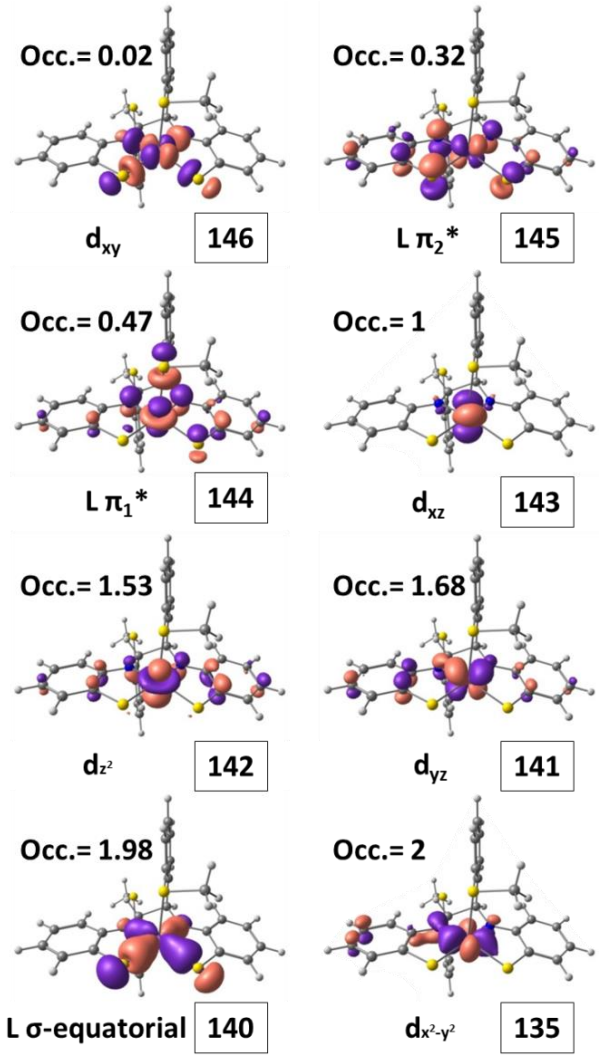

Figure 4.11 Frontier orbitals for complex **6**$^{+}$.

Finally, the concordance between the ideal (0.75) and calculated (2.07) values for the S^2 value of doublet complex $\mathbf{6}^+$, was even worse than for complex **6**. This again is indicative of the presence of more extra shells on the complex after oxidation from **6** to $\mathbf{6}^+$. By comparison with the orbitals on **6**, we can clearly observe that the new open shell on $\mathbf{6}^+$ is related to orbitals 142 and 144. Those orbitals correspond to the d_{z2} on the metal and to the π* orbital of the L1(SNS) fragment, respectively (Figure 4.11). Thus, the one-electron oxidation from **6** to $\mathbf{6}^+$ is again ligand based but, in this case, the electron is abstracted from the L1(SNS) fragment of the ligand. After rearrangement, both sides of the ligand pull electron density of the metal. This is translated on an oxidation state on the metal between Fe(II) and Fe(III), again closer to Fe(III).

Related complexes with CO and $P(OMe)_3$ ligands

As we mentioned in the introduction of this chapter, complex **6** can react with $P(OMe)_3$ and CO forming square pyramidal (**7**) or octahedral (**8**) complexes, respectively. Experimentally, both derivative species were found to be diamagnetic and their X-ray structures could be determined. In this subsection we will present the results of the DFT characterization of these complexes.

Four different spin states were considered for complex **7**: closed-shell singlet, open-shell singlet, triplet and quintet. The relative potential energies for these states are summarized in Table 4.14. We found the open-shell singlet state to be the ground state. The closed singlet, the triplet and the quintet states are at 2.2, 1.7 and 6.7 $kcal \cdot mol^{-1}$ above the open-shell singlet state. The spin state assignment agrees with the experimental magnetism.

Table 4.14 Corrected potential energies (in kcal·mol^{-1}) for the different spin states considered for complex **7**.

Spin state	Corrected Pot. Energy
Closed-shell singlet	0.0
Open-shell singlet	-2.2
Triplet	-0.5
Quintet	4.5

In this case, the comparison between the experimental and the DFT optimized structure is rather inconclusive (Table 4.15). The quintet spin state can be easily discarded because the optimized distances are significantly longer for all the key bonds. However, it is difficult to differentiate between the other three spin states as the optimization yields very similar bond distances.

Table 4.15 Experimental and calculated selected bond distances (in Å) for complex **7**.

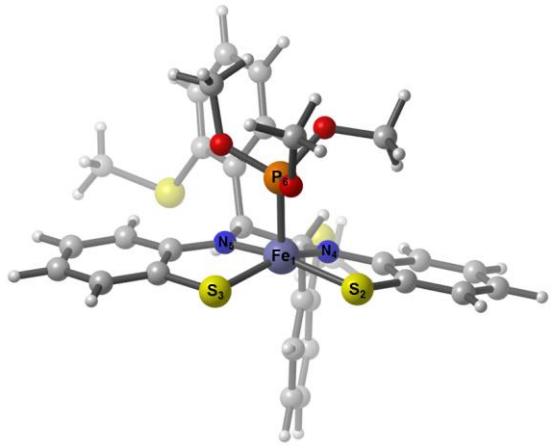

	X-ray values	Calculated			
Bond		**Closed-shell singlet**	**Open-shell singlet**	**Triplet**	**Quintet**
d(Fe-P_6)	2.1606	2.1769	2.2343	2.2540	2.7041
d(Fe-S_2)	2.2037	2.2598	2.2613	2.2714	2.2660
d(Fe-S_3)	2.1986	2.2436	2.3009	2.2650	2.3484
d(Fe-N_4)	1.8461	1.8463	1.8569	1.8421	1.8643
d(Fe-N_5)	1.8451	1.8530	1.8648	1.8622	1.9442

Finally, the last complex to be characterized with DFT tools was the CO complex **8**. We considered all the four spin states as for complex **7**. The Yamaguchi spin corrected potential energies are shown in Table 4.16. We found the closed singlet spin state to be the ground state. The triplet and the quintet states were found at 7.0 and 6.9 kcal·mol^{-1} above the singlet state. All our attempts to obtain the open-shell singlet state of this complex were unsuccessful.

Table 4.16 Corrected potential energies (in kcal·mol^{-1}) for the different spin states considered for complex **8**.

Spin state	Corrected Pot. Energy
Closed-shell singlet	0.0
Open-shell singlet	--
Triplet	7.0
Quintet	6.9

The comparison between the experimental and the calculated structure for complex **8** is summarized in Table 4.17. The results clearly point towards the assignment of the singlet state as the ground state of the complex, in agreement with the experimental findings.

Table 4.17 Experimental and calculated selected bond distances (in Å) for complex **8**.

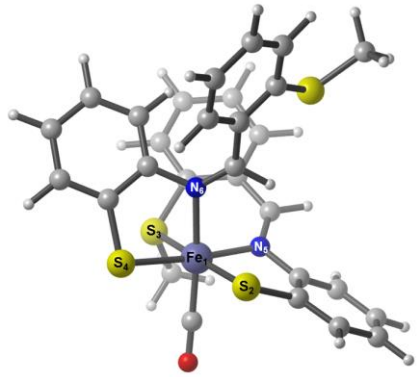

	X-ray values	Calculated		
Bond		**Closed-shell singlet**	**Triplet**	**Quintet**
d(Fe-S_2)	2.2925	2.3533	2.5214	2.4238
d(Fe-S_3)	2.2608	2.3575	2.6408	2.6673
d(Fe-S_4)	2.3026	2.3806	2.3561	2.4504
d(Fe-N_5)	1.9777	2.0070	2.1912	2.2611
d(Fe-N_6)	2.0214	2.0419	2.0201	2.1788
d(Fe-CO)	1.7559	1.7824	1.8000	2.1873

Summary

We have investigated with DFT calculations the electronic structure of **6** and its redox partners. The nature of the ground state of each complex predicated by calculation agrees with the experimental observation. The natural orbital analysis emerges as a key tool to explain the redox properties of these complexes. Specifically, in the first oxidation (from $\mathbf{6}^-$ to **6**) the electron is abstracted from the L2(SN) side of the ligand. This generates an electronic rearrangement in order to stabilize the complex, where a new open shell is formed. The second oxidation (**6** to $\mathbf{6}^+$) is again ligand based, but on the L1(SNS) side of the ligand. This makes sense considering that the L2(SN) side does not have the ability to re-

lease an electron anymore after the first oxidation. After the oxidation, an extra shell is created related with the d_{z2} orbital of the metal and the π* system of the L1(SNS) fragment. A schematic representation of these redox processes is depicted in Figure 4.12. The calculations lead us to conclude that the formal oxidation of the metal is Fe(III) throughout all these processes. We were also able to successfully characterize the CO and $P(OMe)_3$ derivatives of complex **6.**

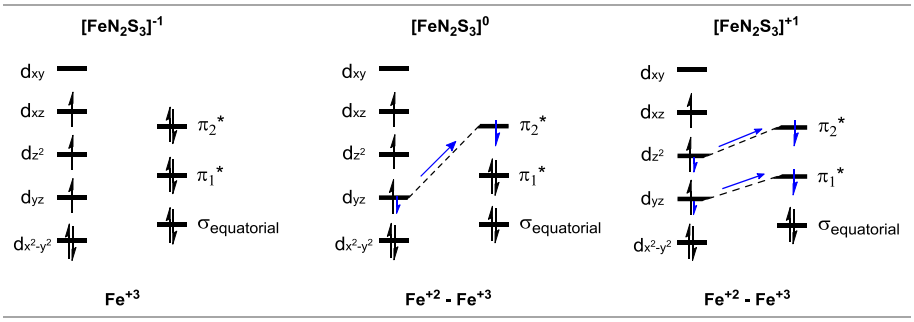

Figure 4.12 Schematic orbital diagram for **6**$^{-}$ (left), **6** (middle) and **6**$^{+}$ (right) complexes.

4.4 Reactivity

Complex **6** is able to selectively catalyze the hydroboration of aldehydes in very mild conditions and with low catalyst loading. From the experimental data we know that upon addition of HBpin to a solution of complex **6**, the color of the solution changes from purple to beige or colorless. This suggests that the boron reagent reacts first with catalyst **6** activating it. Moreover, the addition of aldehyde to **6** does not promote any change in the solution. To elucidate a plausible mechanism, we selected benzaldehyde (**a**) and HBpin (**b**) as model reagents.

The labels for each species in this section will be changed to capital letters instead of numbers. This was done to differentiate between the complexes in both sections. Thus, from now on, complex **6** will be complex **A**.

Monomeric mechanism

We first studied the direct reaction mechanism. Thanks to the previous electronic structure characterization done on complex **A**, we envisaged that a metal-ligand cooperativity could activate both reactants at the same time. The computed profile is depicted in Figure 4.13. The transition state associated to this process would consist of a six-membered ring where new B—S, C—H and Fe—O bonds are formed while the B—H bond of the pinacolborane and the Fe—S bond on the L2(SN) fragment of the ligand would be broken homolytically. The overall reaction for the formation of the hydroborated product is exergonic by 23.6 kcal·mol^{-1}. The transition state associated to this mechanism, **TS A-B**, was found at 35.5 kcal·mol^{-1} from initial reactants (**A** + **a** + **b**). This barrier is not affordable at the experimental conditions. After the transition state, the reaction would evolve barrierless to the formation of the product **B** due to the exergonicity of the reaction. In addition, this concerted mechanism would not match with the experimental finding that report that the HBpin reagent activates the precatalyst **A**, forming the active species.

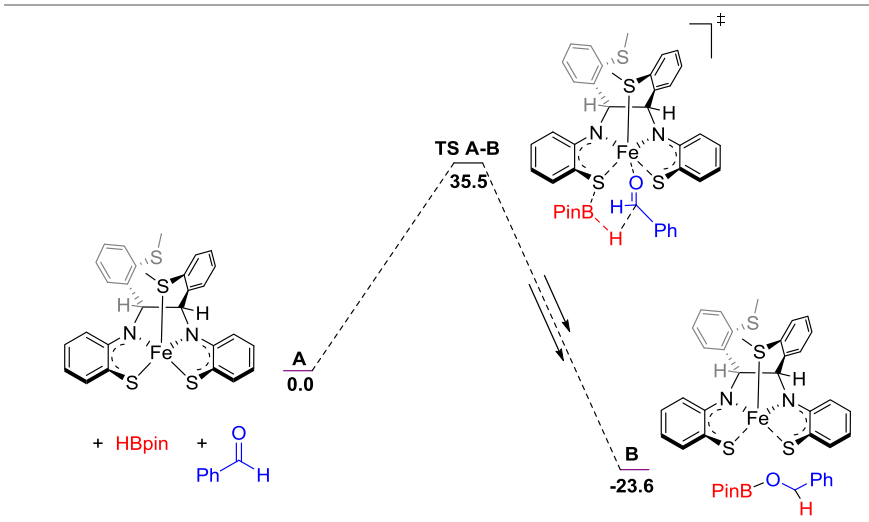

Figure 4.13 Free energy profile for the direct mechanism for the hydroboration of benzaldehyde catalyzed by **A**. Energies in kcal·mol^{-1}.

Afterwards, we decided to focus our efforts on the activation of the pinacolborane by complex **A**. The results for the first approach are shown on Figure 4.14. This mechanism starts with the interaction of reagent **b** with complex **A**. The preferred position would be with the boron atom of the pinacolborane interacting with the S atom of the L2(SN) arm of the ligand while the H atom is interacting with the Fe center. The transition state associated with the H—B bond activation following this pathway, **TS A-C**, was found at 30.0 kcal·mol^{-1}. This high barrier transition state is unaffordable at the reaction conditions. Nevertheless, we continued with the mechanism to check the relative energies of the subsequent steps. After **TS A-C**, intermediate **C** is formed with a relative free energy of 24.7 kcal·mol^{-1}. This intermediate presents a new Fe—H and B—S bond due to the activation of the pinacolborane. From this intermediate, the system could evolve through proton transfer from the Fe center to the S atom of the L1(SNS) side of the ligand. The transition state for this process, **TS C-D**, was found at 26.2 kcal·mol^{-1}. Finally, intermediate **D** was found at 12.1 kcal·mol^{-1} from the initial reactants (**A** + **b**). Although the formation of intermediate **D** is endergonic, the formation of it could be thermodynamically achieved under the reaction conditions. However, the high barriers found for this mechanism make complex **D** kinetically unreachable.

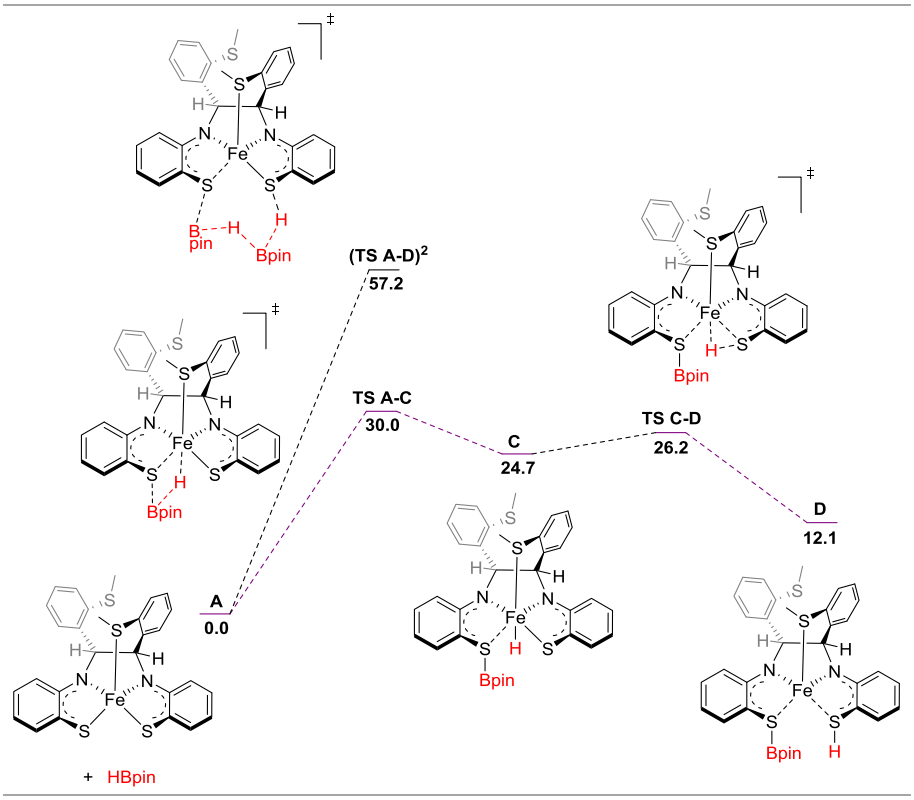

Figure 4.14 Free energy profile for the H—B bond activation *via* the synergetic cooperation of the Fe center and the L2(SN) fragment of the ligand. Energies in kcal·mol^{-1}.

Several alternative intermediates were calculated for **C**. For instance, the decoordination of the axial thioether group or the quintet spin state. Nevertheless, the relative free energies for these alternative intermediates were higher and are not shown on Figure 4.14. We also calculated the possible assistance of a second molecule of **b** which could help on the H—B bond breaking step leading directly to intermediate **D**. The barrier for this transition state, **(TS A-D)²**, was 57.2 kcal·mol^{-1}, totally prohibitive at room temperature.

From this point, we decided to study an alternative mechanism where the activation of the H—B bond of the pinacolborane was achieved with the synergetic cooperation of the Fe center and the S atom on the

L1(SNS) fragment of the ligand. This mechanism was carried out to check if the beta spin density found for the L2(SN) influences the activation step or, on the contrary, the energies for both mechanisms are similar. In addition, this mechanism will lead to a different intermediate were the H and the Bpin groups are bonded to the S atoms of the L2(SN) and L1(SNS) fragments, respectively. The results are summarized in Figure 4.15.

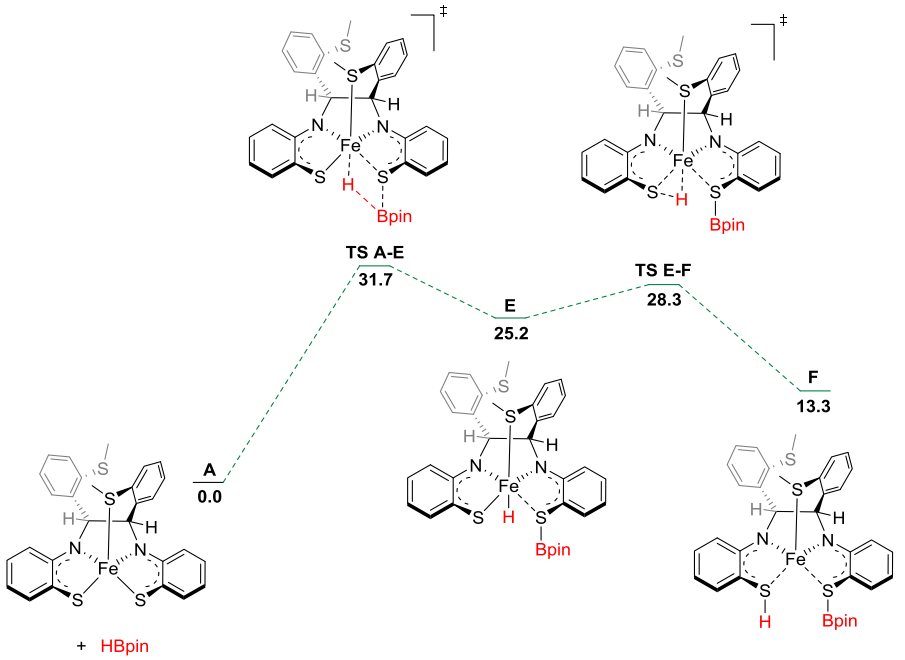

Figure 4.15 Free energy profile for the H—B bond activation *via* the synergetic cooperation of the Fe center and the L1(SNS) fragment of the ligand. Energies in kcal·mol^{-1}.

This alternative mechanism presents very little differences in terms of relative energies. For example, the high lying **TS A-E** in Figure 4.15 is only 1.7 kcal·mol^{-1} higher than **TS A-C** in Figure 4.14. Similar energy differences were found for the other stationary points of the profile depicted in Figure 4.15.

Even if our first approaches were not successful, these studies gave us the idea that several intermediates could be generated after the pinacolborane activation. This idea emerged after observing that both intermediates **D** and **F** had a very similar relative free energy, and both would be formed after surpassing comparable activation barriers (**TS A-C** and **TS A-E**, respectively). Thus, we decided to investigate the speciation of the reaction after the pinacolborane activation.

The results of the speciation study are shown in Figure 4.16. We studied many different species where the Bpin and the H groups are attached to different atoms on the complex. For example, complex **G** has both fragments attached on the L1(SNS) side of the ligand; the H atom is attached on the N while the Bpin group is attached to the S atom. Another example is complex **J**, where the H atom is attached to the N of the L1(SNS) part while the Bpin is on the S atom of the L2(SN) side of the ligand. In addition, for most species we have calculated the square planar version where the thioether group has been decoordinated from the metal center. The reported energies in Figure 4.16 are potential energies in solution. This was done to speed up the investigation on the possible species after the H—B activation step and, since we are comparing analogues species, the entropic corrections will account similar for all the complexes.

As can be observed in Figure 4.16, the energy range for the considered intermediates is quite large (from -21.1 to 12.8 kcal·mol^{-1}, for **J** and **E**, respectively). Several considerations can be extrapolated from those results. The higher energy structures present an Fe—H bond. In this regard, all the attempts to coordinate the Bpin fragment on the Fe center were unsuccessful. Instead, the Bpin group relocates and stays attached to a different S or N atom of the ligand. In general, the decoordination of the thioether group destabilizes the complex (*e.g.*, **J** *vs.* **J-noS**).

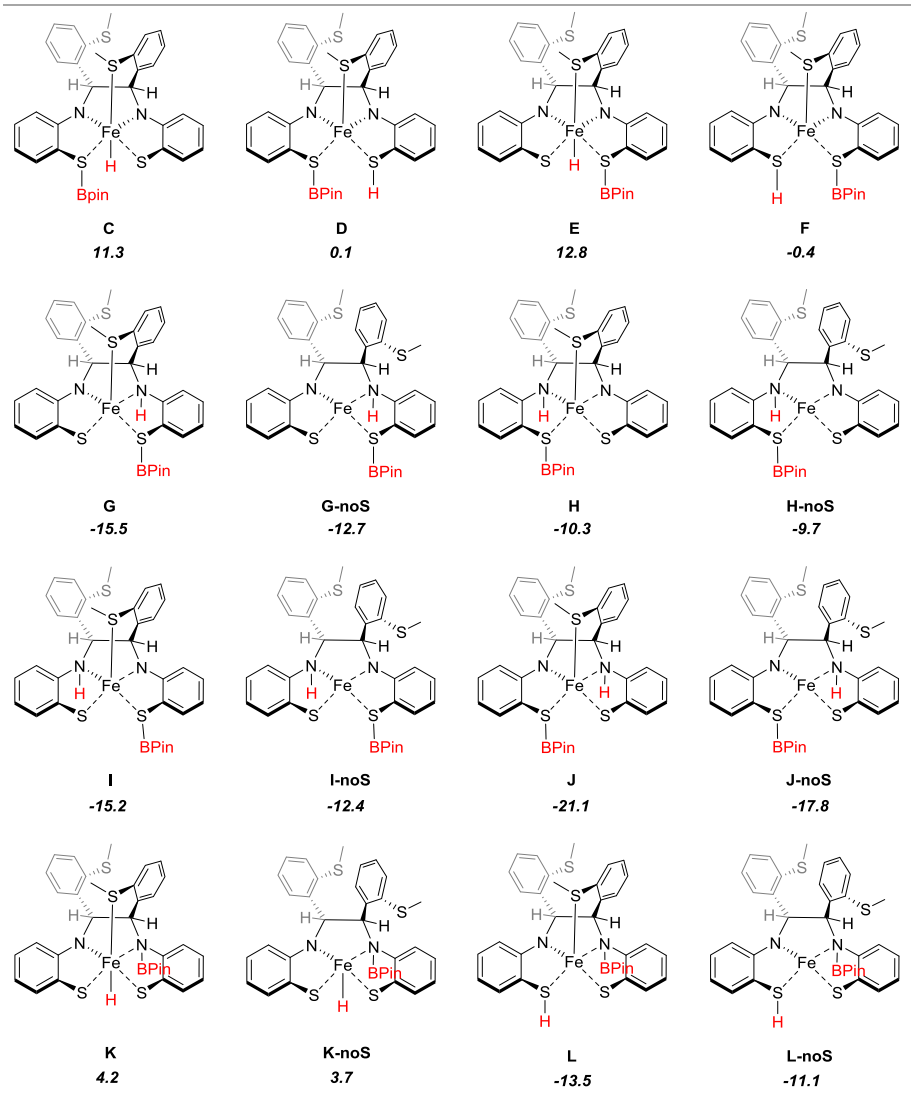

Figure 4.16 Possible structural isomers after the pinacolborane activation step. Potential energies in solution in kcal·mol^{-1}.

The most stable structure that we found was complex **J**. In this complex, the H atom is attached to the N atom of the L1(SNS) fragment while the Bpin group is bonded to the S atom of the L2(SN) side of the ligand. We considered different spin states for this structure (Figure 4.17). The singlet spin state was found 13.2 kcal·mol^{-1} above the triplet

state and interestingly, the quintet spin state was isoenergetic with the triplet state. The spin distribution for both states shows that the unpaired electrons are localized in the metal center.

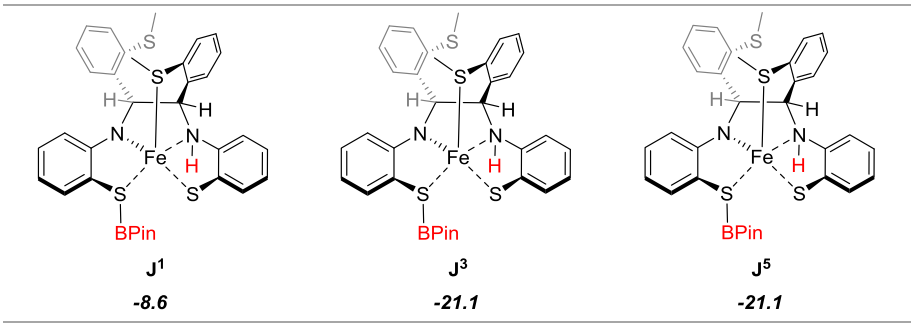

Figure 4.17 Potential energies for different spin states of complex **J**. Energies in kcal·mol^{-1}.

Unfortunately, we could not find a proper mechanism to obtain complex **J**. Probably due to the high complexity of the electronic structure that the transition state should have to break the H—B bond in a homolytic manner. Nevertheless, we decided to study the hydroboration of the benzaldehyde starting from **J**. The calculated profiles for the triplet (in green) and quintet (in purple) spin states are shown in Figure 4.18 and Figure 4.20.

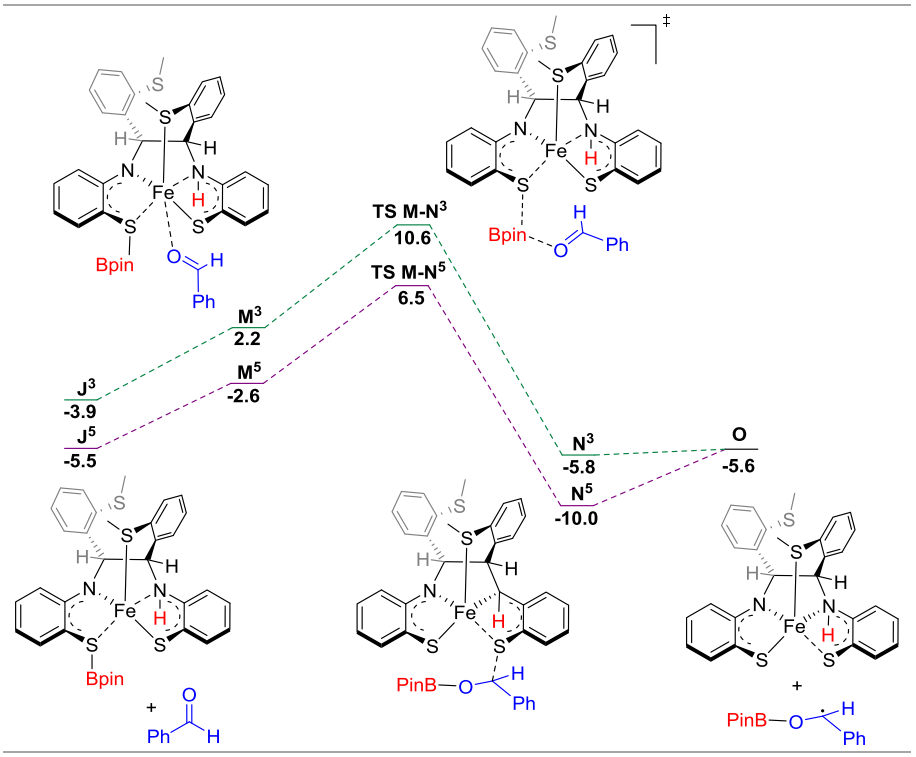

Figure 4.18 First step for the hydroboration of benzaldehyde from complex **J**. Energies in kcal·mol-1. Triplet and quintet spin surface in green and purple, respectively.

The first part of the mechanism (Figure 4.18) starts with the adduct formation between **J** and benzaldehyde (**a**). Then, the system evolves through the O—B bond formation, **TS M-N**, to form intermediate **N** in an exergonic step (see Figure 4.19 for 3D structures). This step has an activation barrier of 14.5 and 12.0 kcal·mol^{-1} on the triplet and quintet spin surface, respectively. Interestingly, the structure of intermediate **N** presents a new S—C bond, formed after the O—B bond step formation. The distances of this S—C bond are 1.92 and 1.91 Å, for the triplet and the quintet complexes, respectively. Finally, this bond can be easily broken to form complex **O** and releasing the radical **c**, which can be seen as the reduced radical form of benzaldehyde. Once radical **c** is released to the media, both surfaces converge to the same point in **O** because one unpaired electron was on the carbon atom of **c**.

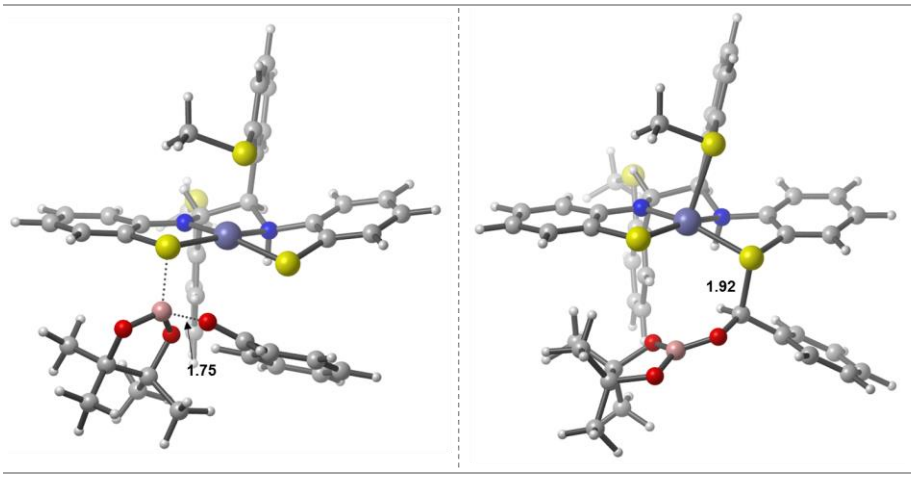

Figure 4.19 3D optimized structure of **TS M-N^3** (left) and **N^3** (right). Selected bond distances in Å.

The second part of the mechanism is depicted in Figure 4.20. The radical **c** can approach to the N—H group of the catalyst in a ferromagnetic or antiferromagnetic manner. The first approach will lead to complex **P^5**, which was found 2.7 kcal·mol^{-1} below intermediate **O**. The antiferromagnetic complex **P^3** was found on the triplet state surface, 2.3 kcal·mol^{-1} below intermediate **O**. The final step of this mechanism consists in the hydrogen atom transfer (HAT) from the N atom to the C atom, **TS P-A**, which leads to the final hydroborated aldehyde. In this case, the activation barrier associated to this transition state was higher for the quintet than for the triplet spin state. The respective values are 16.9 kcal·mol^{-1} for **TS P-A^5**, from intermediate **N^5**; and 11.8 kcal·mol^{-1} for **TS P-A^3**, from intermediate **P^3**. This energy difference can be rationalized considering that the initial catalyst **A** would be regenerated in this step and that the triplet state is more stable by *ca.* 7.0 kcal·mol^{-1}.

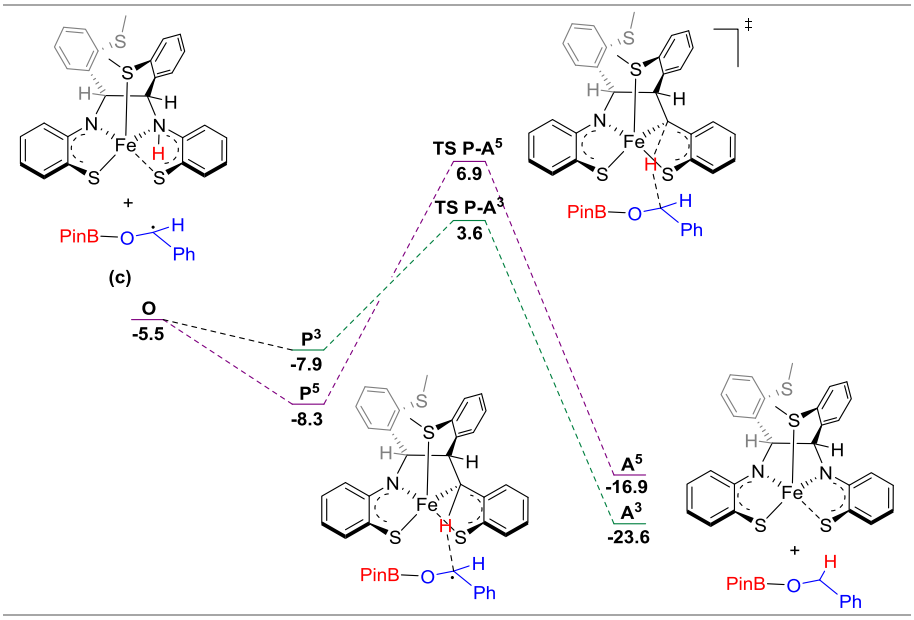

Figure 4.20 Final step for the hydroboration of benzaldehyde from complex **J**. Energies in kcal·mol^{-1}. Triplet and quintet spin surface in green and purple, respectively.

To sum up on this section, different species are energetically available after the activation of the HBpin substrate by catalyst **A**. Complex **J** is the most stable hydroborated intermediate within those considered. This complex **J** can hydroborate benzaldehyde with an overall barrier for this step of 14.5 kcal·mol^{-1}, associated to the formation of the O—B bond step. However, we were not able to elucidate a kinetically affordable pathway for the activation of the HBpin molecule.

Dimeric mechanism

Thanks to the speciation investigation carried out in the previous subsection, we envisaged that may be two complexes **A** could activate the pinacolborane (**b**) in a cooperative manner. As result, each fragment of reagent **b** (the H atom or the Bpin group) would remain attached to different complexes. The less hindered spot on complex **A** with the enough spin density to break this bond is the sulfur atom of the L2(SN)

fragment. Thus, we started calculating the thermodynamics of this reaction (Scheme 4.10).

Scheme 4.10 Schematic representation of the H—B bond activation by two initial catalysts **A**. Energies in kcal·mol^{-1}.

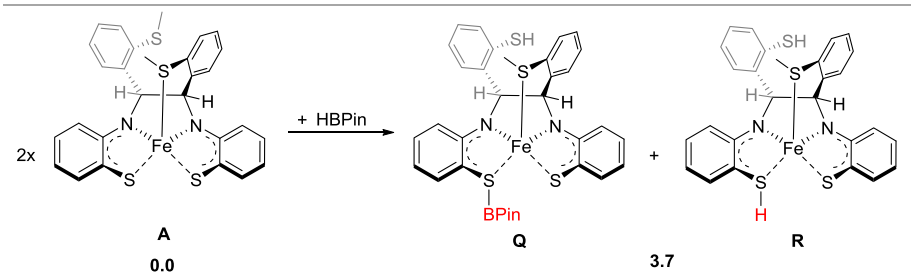

The reaction to cleave homolytically the HBpin reagent, forming complexes **Q** and **R**, was found thermodynamically unfavorable by 3.7 kcal·mol^{-1}. Nevertheless, we believe that after this step, the system can evolve to more stable intermediates.

The next step was to introduce two complexes on the same calculation modeling the H—B bond breaking event. This calculation is quite tricky. The bond breaking step would take place homolytically so, that means, both complexes should be in an antiferromagnetic arrangement. A further difficulty is that two complexes of **A** in the same calculation would increase the computing cost to unaffordable times. For this reason, we decided to model complex **A** in a rational way keeping the intrinsic electronic structure so that the reactivity is not affected. We decided to substitute the aryl group on the backbone of the ligand by simpler structures: for the group attached to the iron center by the thioether moiety, we substituted the benzene ring by an alkene. This keeps the ability of this moiety to interact with the metal center within similar distances. The other substituent was replaced by a methyl group because it does not seem to participate in the key orbitals in the electronic structure of the complex. In addition, the methyl groups of the

pinacolborane were replaced by hydrogen atoms to reduce the number of atoms on the calculation (see Scheme 4.11).

Scheme 4.11 Real (left) and model (right) systems for the calculation of the dimeric mechanism.

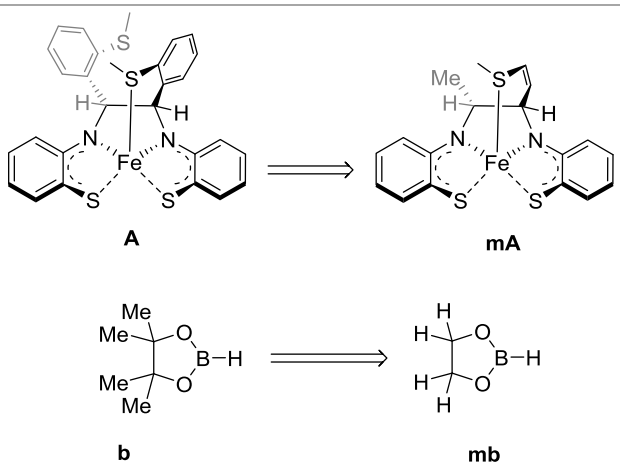

We successfully modelized complex **A** keeping the same electronic structure on the model complex **mA**. The electronic structure comparison between **A** and **mA** is shown in Table 4.18.

Table 4.18 Spin density comparison between real complex **A** and model complex **mA** in the triplet spin state.

System	Fe	L1(SNS)	L2(SN)
A	2.54	0.16	-0.70
mA	2.57	0.21	-0.78

With this, we were able to run the antiferromagnetic arrangement between two **mA** complexes (Figure 4.21a). The reaction runs on the open-shell singlet surface. The interaction between both complexes slightly stabilizes the complexes, in **mS**, by -0.5 kcal·mol^{-1}. The two monomers are displayed in an antiparallel way, where the thioether groups are pointing outwards (Figure 4.21b). In addition, they are in a rocking type arrangement between each other (rotation around 45°, between each complex). This shortens the distance between both S atoms

of each L2(SN) fragment (Figure 4.22, left). The S—S distance in **mS** is 3.76 Å. The introduction of the **mb** reagent unstabilizes the system by 5.0 kcal·mol^{-1}, **mT**. Although the distances between the HBpin reactant and the two monomers are quite large (3.53 and 3.61 Å for H—S and B—S distances, respectively), the interaction reduces the distances between both S atom of each L2(SN) fragment of the monomers (from 3.75 to 3.59 Å in **mS** and **mT**, respectively). The next step would consist on the homolytically cleavage of the H—B bond. Unfortunately, we could not find the associated transition state, **TS mT-mU**. Probably, due to electronic issues. Instead, we were able to find the product of this step, **mU**, lying at 1.5 kcal·mol^{-1}, from the initial reactants. The comparison between the spin distribution in **mT** and **mU** clearly shows that both monomers aid in the H—B bond breaking step (Figure 4.21c). Once HBpin has approached the dimer, this interaction promotes a rearrangement on the electronic structure of both complexes to place and entire electron on the L2(SN) fragment of each ligand to achieve the bond breaking process. This spin density is not found on intermediate **mU** due to the formation of the S—H and S—B bond. Interestingly, the optimized structure of **mU** showed an interaction between the S—H group and the S atom of the L1(SNS) fragment of the other monomer. The distances are 1.40 and 2.15 Å, respectively. This suggests that the H atom can be easily transferred to the other monomer, affording intermediate **mD**. In fact, we were able to locate the transition state associated to this hydrogen atom transfer, **TS mU-mD**, with a low barrier of 1.4 kcal·mol^{-1}, from intermediate **mU** (see Figure 4.22, right, for 3D structure). The product of this path would lead to intermediate **mD**, with the H and the boron group attached to the L2(SN) and L1(SNS) fragments of the ligand, respectively; together with the regeneration of the initial catalyst **mA**. The formation of **mD** is slightly endergonic by 1.4 kcal·mol^{-1}, from **mU** (Figure 4.21a).

We have to take into account that other destinations for the proton are possible. For instance, the proton could be transferred to the N atom of the L1(SNS) side of the second monomer achieving intermediate **mJ** (model of complex **J** shown on Figure 4.16). Complex **J** has been previously demonstrated that is capable of hydroborate benzaldehyde producing the desired product with very low barriers (Figure 4.18 and 4.20).

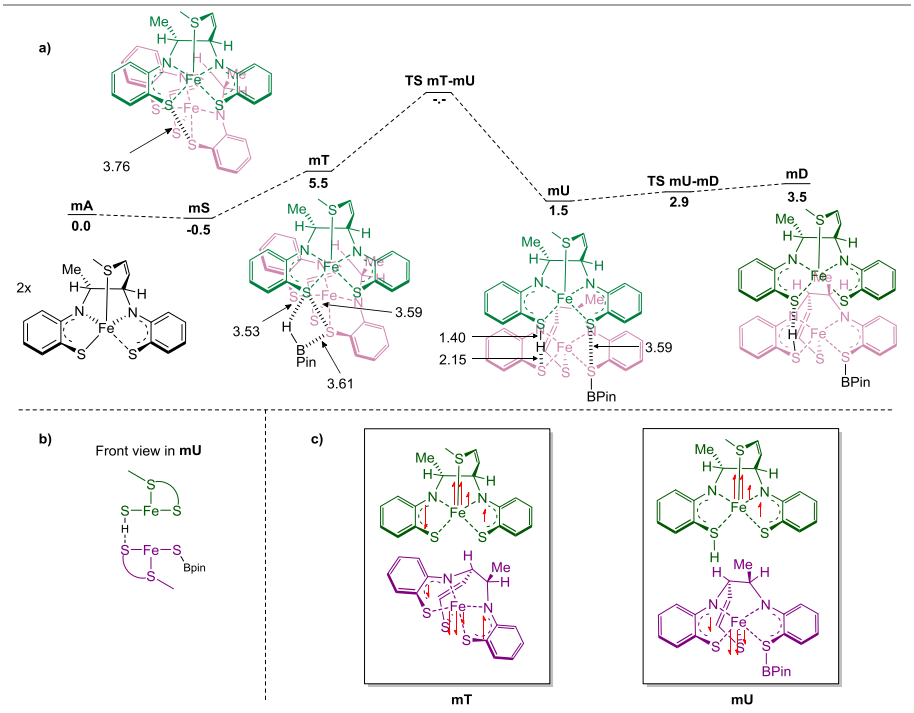

Figure 4.21 a) Free energy profile for the dimeric activation of the model pinacolborane (**mb**). Energies are free energies in solution in kcal·mol^{-1}. Green and purple colors used to distinguish between both monomers interacting in an antiferromagnetic arrangement. b) Front view of intermediate **mU.** c) Spin density disposition in intermediate **mT** and **mU**. Half arrows pointing up and down, account for the α and β spin density, respectively.

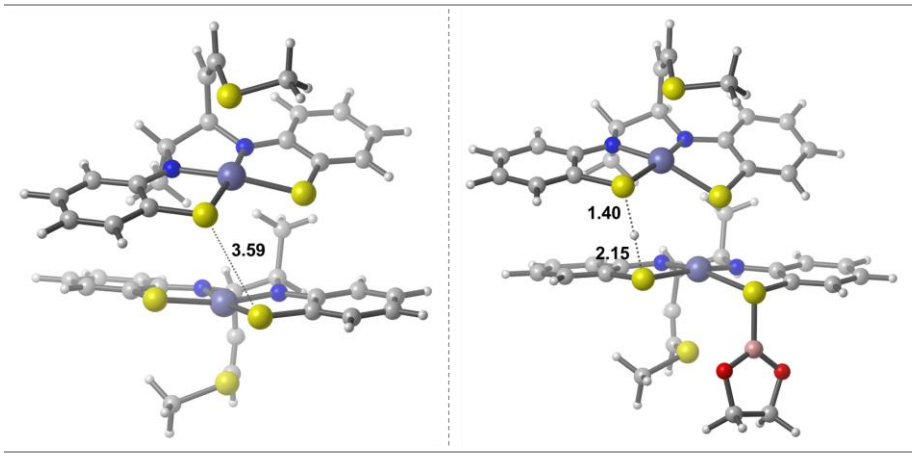

Figure 4.22 3D optimized structure of **mS** (left) and **TS mU-mD** (right). Selected bond distances in Å.

The direct extrapolation of these results from the model to the real system is not trivial. The latter would generate a higher steric hindrance between complexes, caused by the substituents of the backbone of the ligand. Thus, the interaction between two **A** species would not be very favorable. Nevertheless, since the reaction takes place on the S atoms of each complex, we think that this mechanism could be possible, probably with a different arrangement between complexes.

4.5 Summary

In this section we have studied the possible mechanism for the hydroboration of benzaldehyde catalyzed by $[Fe(N_2S_3]^0$ (**A**). We were not able to find a proper mechanism to activate the H—B bond. All our attempts to cleave this bond homolytically reported higher barriers, not affordable at the reaction conditions. We believe that this is due to the electronic structural complexity that the presumed transition state may bear. The speciation study after the H—B bond breaking step, reported the possible formation of many intermediates in a wide range of energies. We decided to study the hydroboration of benzaldehyde from one of these intermediates, complex **J**, which was found to be the most stable among all the considered species. Complex **J** shows the ability to

carry out this reaction step in the triplet and quintet spin surfaces, with very low barrier. This suggests that once the H—B bond has been broken, forming any of the complexes shown in Figure 4.16, the reaction proceeds with very low barriers.

We investigated a dimeric mechanism where two complexes **A** were able to activate and break the H—B bond of pinacolborane. Due to the size of the system, we had to model complex **A**, reducing the number of atoms. We found a possible mechanism were the cooperativity of two **mA** complexes could activate the H—B bond homolytically. However, we were not able to find the key transition state for this mechanism, probably due to the complexity of its electronic structure. These results are a good starting point for the elucidation of the real mechanism governing this transformation, in a research that will continue in the group.

4.6 References

[1] Lee, S. C.; Holm, R. H. *Chem. Rev.* **2004**, 104, 1135-1158.

[2] Kovacs, J. A. *Chem. Rev.* **2004**, 104, 825-848.

[3] Fontecilla-Camps, J. C.; Volbeda, A.; Cavazza, C.; Nicolet, Y. *Chem. Rev.* **2007**, 107, 4273-4303.

[4] Tard, C.; Pickett, C. J. *Chem. Rev.* **2009**, 109, 2245-2274.

[5] Niviere, V.; Bonnot, F.; Bourgeois, D. *Handbook of Metalloproteins*; Vols. 4 and 5, Wiley & Sons: Chichester, U.K., **2011**.

[6] McQuilken, A. C.; Goldberg, D. P. *Dalton Trans.* **2012**, 41, 10883-10899.

[7] Lubitz, W.; Ogata, H.; Rüdiger, O.; Reijerse, E. *Chem. Rev.* **2014**, 114, 4081-4148.

[8] De Lacey, A. L.; Fernández, V. M.; Rousset, M.; Cammack, R. *Chem. Rev.* **2007**, 107, 4304-4330.

[9] Seefeldt, L. C.; Hoffman, B. M.; Dean, D. R. *Annu. Rev. Biochem.* **2009**, 78, 701-722.

[10] Hoffman, B. M.; Lukoyanov, D.; Dean, D. R.; Seefeldt, L. C. *Acc. Chem. Res.* **2013**, 46, 587-595.

[11] Felton, G. A. N.; Petro, B. J.; Glass, R. S.; Lichtenberger, D. L.; Evans, D. H. *J. Am. Chem. Soc.* **2009**, 131, 11290-11291.

[12] Ryde, U.; Greco, C.; De Gioia, L. *J. Am. Chem. Soc.* **2010**, 132, 4512-4513.

[13] Shomura, Y.; Yoon, K.-S.; Nishihara, H.; Higuchi, Y. *Nature* **2011**, 479, 253-256.

[14] Almazahreh, L. R.; Apfel, U.-P.; Imhof, W.; Rudolph, M.; Görls, H.; Talarmin, J.; Schollhammer, P.; El-khateeb, M.; Weigand, W. *Organometallics* **2013**, 32, 4523-4530.

[15] Wang, W.; Nilges, M. J.; Rauchfuss, T. B.; Stein, M. *J. Am. Chem. Soc.* **2013**, 135, 3633-3639.

[16] In-noi, O.; Haller, K. J.; Hall, G. B.; Brezinski, W. P.; Marx, J. M.; Sakamoto, T.; Evans, D. H.; Glass, R. S.; Lichtenberger, D. L. *Organometallics* **2014**, 33, 5009-5019.

[17] Capon, J.-F.; Gloaguen, F.; Schollhammer, P.; Talarmin, J. *J. Electroanal. Chem.* **2006**, 595, 47-52.

[18] Hirotsu, M.; Santo, K.; Tsuboi, C.; Kinoshita, I. *Organometallics* **2014**, 33, 4260-4268.

[19] Rose, M. J.; Betterley, N. M.; Mascharak, P. K. *J. Am. Chem. Soc.* **2009**, 131, 8340-8341.

[20] Rose, M. J.; Betterley, N. M.; Oliver, A. G.; Mascharak, P. K. *Inorg. Chem.* **2010**, 49, 1854-1864.

[21] Harrop, T. C.; Mascharak, P. K. *Acc. Chem. Res.* **2004**, 37, 253-260.

[22] Kovacs, J. A.; Brines, L. M. *Acc. Chem. Res.* **2007**, 40, 501-509.

[23] Widger, L. R.; Jiang, Y.; Siegler, M. A.; Kumar, D.; Latifi, R.; de Visser, S. P.; Jameson, G. N. L.; Goldberg, D. P. *Inorg. Chem.* **2013**, 52, 10467-10480.

[24] Widger, L. R.; Jiang, Y.; McQuilken, A. C.; Yang, T.; Siegler, M. A.; Matsumura, H.; Moënne-Loccoz, P.; Kumar, D.; de Visser, S. P.; Goldberg, D. P. *Dalton Trans.* **2014**, 43, 7522-7532.

[25] Xiao, J.; Deng, L. *Organometallics* **2012**, 31, 428-434.

[26] Ye, S.; Kaim, W.; Albrecht, M.; Lissner, F.; Schleid, T. *Inorg. Chim. Acta* **2004**, 357, 3325-3330.

[27] Blackwell III, W. C.; Bunich, D.; Concolino, T. E.; Rheingold, A. L.; Rabinovich, D. *Inorg. Chem. Commun.* **2000**, 3, 325-327.

[28] Klerman, Y.; Ben-Ari, E.; Diskin-Posner, Y.; Leitus, G.; Shimon, L. J. W.; Ben-David, Y.; Milstein, D. *Dalton Trans.* **2008**, 3226-3234.

[29] McGuinness, D. S.; Wasserscheid, P.; Keim, W.; Morgan, D.; Dixon, J. T.; Bollmann, A.; Maumela, H.; Hess, F.; Englert, U. First. *J. Am. Chem. Soc.* **2003**, 125, 5272-5273.

[30] Lumsden, S. E. A.; Durgaprasad, G.; Muthiah, K. A. T.; Rose, M. J. *Dalton Trans.* **2014**, 43, 10725-10738.

[31] Schnödt, J.; Manzur, J.; García, A.-M.; Hartenbach, I.; Su, C.-Y.; Fiedler, J.; Kaim, W. *Eur. J. Inorg. Chem.* **2011**, 9, 1436-1441.

[32] Hübner, R.; Weber, S.; Strobel, S.; Sarkar, B.; Záliš, S.; Kaim, W. *Organometallics* **2011**, 30, 1414-1418.

[33] Takemoto, S.; Kawamura, H.; Yamada, Y.; Okada, T.; Ono, A.; Yoshikawa, E.; Mizobe, Y.; Hidai, M. *Organometallics* **2002**, 21, 3897-3904.

[34] Imbert, C.; Hratchian, H. P.; Lanznaster, M.; Heeg, M. J.; Hryhorczuk, L. M.; McGarvey, B. R.; Schlegel, H. B.; Verani, C. N. *Inorg. Chem.* **2005** , 44, 7414-7422.

[35] Roy, N.; Sproules, S.; Weyhermüller, T.; Wieghardt, K. *Inorg. Chem.* **2009**, 48, 3783-3791.

[36] Fox, D. J.; Bergman, R. G. *J. Am. Chem. Soc.* **2003**, 125, 8984-8985.

[37] Zhao, H.; Li, X.; Zhang, S.; Sun, H. *Z. Anorg. Allg. Chem.* **2015**, 641, 2435-2439.

[38] Koizumi, T.-a.; Teratani, T.; Okamoto, K.; Yamamoto, T.; Shimoi, Y.; Kanbara, T. *Inorg. Chim. Acta* **2010**, 363, 2474-2480.

[39] Singh, P.; Singh, A. K. *Organometallics* **2010**, 29, 6433-6442.

[40] Harkins, S. B.; Peters, J. C. *J. Am. Chem. Soc.* **2004**, 126, 2885-2893.

[41] Shaffer, D. W.; Szigethy, G.; Ziller, J. W.; Heyduk, A. F. *Inorg. Chem.* **2013**, 52, 2110-2118.

[42] Ye, S.; Sarkar, B.; Lissner, F.; Schleid, T.; van Slageren, J.; Fiedler, J.; Kaim, W. *Angew. Chem. Int. Ed.* **2005**, 44, 2103-2106.

[43] Noveron, J. C.; Olmstead, M. M.; Mascharak, P. K. *Inorg. Chem.* **1998**, 37, 1138-1139.

[44] Miecznikowski, J. R.; Lo, W.; Lynn, M. A.; Jain, S.; Keilich, L. C.; Kloczko, N. F.; O 'Loughlin, B. E.; DiMarzio, A. P.; Foley, K. M.; Lisi, G. P.; Kwiecien, D. J.; Butrick, E. E.; Powers, E.; Al-Abbasee, R. *Inorg. Chim. Acta* **2012**, 387, 25-36.

[45] Bouwman, E.; Henderson, R. K.; Powell, A. K.; Reedijk, J.; Smeets, W. J. J.; Spek, A. L.; Veldman, N.; Wocadlo, S. J. *Chem. Soc., Dalton Trans.* **1998**, 3495-3500.

[46] Das, U. K.; Daifuku, S. L.; Gorelsky, S. I.; Korobkov, I.; Neiding, M. L.; Le Roy, J. J.; Murugesu, M.; Baker, R. T. *Inorg. Chem.* **2016**, 55, 987-997.

[47] Das, U. K.; Higman, C. S.; Gabidullin, B.; Hein, J. E.; Baker, R. T. *ACS Catal.* **2018**, 8, 1076-1081.

[48] Sarvary, I.; Almqvist, F.; Frejd, T. *Chem. - Eur. J.* **2001**, 7, 2158-2166.

[49] Oluyadi, A. A.; Ma, S.; Muhoro, C. N. *Organometallics* **2013**, 32, 70-78.

[50] Khalimon, A. Y.; Farha, P.; Kuzmina, L. G.; Nikonov, G. I. *Chem. Commun.* **2012**, 48, 455-457.

[51] Tamang, S. R.; Findlater, M. *J. Org. Chem.* **2017**, 82, 12857-12862.

[52] Kaithal, A.; Chatterjee, B.; Gunanathan, C. *Org. Lett.* **2015**, 17, 4790-4793.

[53] Guo, J.; Chen, J.; Lu, Z. *Chem. Commun.* **2015**, 51, 5725-5727.

[54] Bagherzadeh, S.; Mankad, N. P. *Chem. Commun.* **2016**, 52, 3844-3846.

[55] Mukherjee, D.; Osseili, H.; Spaniol, T. P.; Okuda, J. *J. Am. Chem. Soc.* **2016**, 138, 10790-10793.

[56] Mukherjee, D.; Ellern, A.; Sadow, A. D. *Chem. Sci.* **2014**, 5, 959-964.

[57] Lampland, N. L.; Hovey, M.; Mukherjee, D.; Sadow, A. D. *ACS Catal.* **2015**, 5, 4219-4226.

[58] Yadav, S.; Pahar, S.; Sen, S. S. *Chem. Commun.* **2017**, 53, 4562-4564.

[59] Yang, Z.; Zhong, M.; Ma, X.; Nijesh, K.; De, S.; Parameswaran, P.; Roesky, H. W. *J. Am. Chem. Soc.* **2016**, 138, 2548-2551.

[60] Jakhar, V. K.; Barman, M. K.; Nembenna, S. *Org. Lett.* **2016**, 18, 4710-4713.

[61] Blake, A. J.; Cunningham, A.; Ford, A.; Teat, S. J.; Woodward, S. *Chem. - Eur. J.* **2000**, 6, 3586-3594.

[62] Locatelli, M.; Cozzi, P. G. *Angew. Chem. Int. Ed.* **2003**, 42, 4928-4930.

[63] Lummis, P. A.; Momeni, M. R.; Lui, M. W.; McDonald, R.; Ferguson, M. J.; Miskolzie, M.; Brown, A.; Rivard, E. *Angew. Chem. Int. Ed.* **2014**, 53, 9347-9351.

[64] Hadlington, T. J.; Hermann, M.; Frenking, G.; Jones, C. *J. Am. Chem. Soc.* **2014**, 136, 3028-3031.

[65] Chong, C. C.; Hirao, H.; Kinjo, R. *Angew. Chem. Int. Ed.* **2015**, 54, 190-194.

[66] Evans, D. F. *J. Chem. Soc.* **1959**, 2003-2005.

[67] Luca, O. R.; Crabtree. R. H. *Chem. Soc. Rev.* **2013**, 42, 1440-1459.

[68] Sproules, S.; Wieghardt, K. *Coord. Chem. Rev.* **2010**, 254, 1358-1382.

[69] Stoian, S. A.; Yu, Y.; Smith J. M.; Holland, P. L.; Bominaar, E. L.; Münck, E. *Inorg. Chem.* **2005**, 44, 4915-4922.

[70] Stoll, S.; Schweiger A. *J. Magn. Reson.* **2006**, 178, 42-55.

[71] Frisch, M. J.; Trucks, G. W.; Schlegel, H. B.; Scuseria, G. E.; Robb, M. A.; Cheeseman, J. R.; Scalmani, G.; Barone, V.; Mennucci, B.; Petersson, G. A.; Nakatsuji, H.; Caricato, M.; Li, X.; Hratchian, H. P.; Izmaylov, A. F.; Bloino, J.; Zheng, G.; Sonnenberg, J. L.; Hada, M.; Ehara, M.; Toyota, K.; Fukuda, R.; Hasegawa, J.; Ishida, M.; Nakajima, T.; Honda, Y.; Kitao, O.; Nakai, H.; Vreven, T.; Montgomery, J. A., Jr.; Peralta, J. E.; Ogliaro, F.; Bearpark, M.; Heyd, J. J.; Brothers, E.; Kudin, K. N.; Staroverov, V. N.; Kobayashi, R.; Normand, J.; Raghavachari, K.; Rendell, A.; Burant, J. C.; Iyengar, S. S.; Tomasi, J.; Cossi, M.; Rega, N.; Millam, J. M.; Klene, M.; Knox, J. E.; Cross, J. B.; Bakken, V.; Adamo, C.; Jaramillo, J.; Gomperts, R.; Stratmann, R. E.; Yazyev, O.; Austin, A. J.; Cammi, R.; Pomelli, C.; Ochterski, J. W.; Martin, R. L.; Morokuma, K.; Zakrzewski, V. G.; Voth, G. A.; Salvador, P.; Dannenberg, J. J.; Dapprich, S.; Daniels, A. D.; Farkas, Ö.; Foresman, J. B.; Ortiz, J. V.; Cioslowski, J.; Fox, D. J. *Gaussian 09, revision D.01*; Gaussian, Inc., Wallingford, CT, **2013**.

[72] Becke, A. D. *J. Chem. Phys.* **1993**, 98, 5648-5652.

[73] Gimme, S. Antony, J. Ehrlich, S.; Krieg, H. *J. Chem. Phys.* **2010**, 132, 154104-19.

[74] Marenich, A. V.; Cramer, C. J.; Truhlar, D. G. *J. Phys. Chem. B.* **2009**, 113, 6378-6396.

[75] a) Hehre, W.J.; Ditchfield, R.; Pople, J.A. *J. Chem. Phys.* **1972**, 56, 2257-2261. b) Hariharan, P.C.; Pople, J.A. *Theoret. Chimica Acta* **1973**, 28, 213-222. c) Francl, M.M.; Petro, W.J.; Hehre, W.J.; Binkley, J.S.; Gordon, M.S.; DeFrees, D.J.; Pople, J.A. *J. Chem. Phys.* **1982**, 77, 3654-3665.

[76] Hay, P. J.; Wadt, W. R. *J. Chem. Phys.* **1985**, 82, 270-283.

[77] a) Yamaguchi, K.; Jensen, F.; Dorigo, A.; Houk, K. N. *Chem. Phys. Let.* **1988**, 149, 537-542. b) Yamanaka, S.; Kawakami, T.; Nagao, H.; Yamaguchi, K. *Chem. Phys. Let.* **1994**, 231, 25-33. c) Swart, M.; Guell, M.; Josep M. Luis, J. M.; Sola, M. *J. Phys. Chem. A* **2010**, 114, 7191-7197.

[78] a) Neese, F. *WIREs Comput Mol Sci* **2012**, 2, 73-78. b) Neese, F. *WIREs Comput Mol Sci* **2018**, 8, e1327.

[79] a) Barone, V.; Cossi, M. *J. Phys. Chem. A* **1998**, 102, 1995-2001. b) Cossi, M.; Rega, N.; Scalmani, G.; Barone, V. *J. Comput. Chem.* **2003**, 24, 669-681.

[80] a) Han, W.-G.; Liu, T.; Lovell, T.; Noodleman, L. *J. Comput. Chem.* **2006**, 27, 1292-1306. b) Hopmann, K. H.; Ghosh, A.; Noodleman, L. *Inorg. Chem.* **2009**, 48, 9155-9165. c) Sandala, G. M.; Hopmann, K. H.; Ghosh, A.; Noodleman, L. *J. Chem. Theory Comput.* **2011**, 7, 3232-3247. d) Pápai, M.; Vankó, G. *J. Chem. Theory Comput.* **2013**, 9, 5004-5020.

[81] a) Weigend F.; Ahlrichs, R. *Phys. Chem. Chem. Phys.* **2005**, 7, 3297-3305. b) Nesse, F. *Inorg. Chim. Acta* **2002**, 337, 181-192. c)

Sinnecker, S.; Slep, L. D.; Bill, E.; Neese, F. *Inorg. Chem.* **2005**, 44, 2245-2254.

[82] Römelt, M.; Ye, S.; Neese, F. *Inorg. Chem.* **2009**, 48, 784-785.

[83] Legault, C. Y. CYLview, 1.0b; Université de Sherbrooke: Quebec, Montreal, Canada, **2009**; www.cylview.org

[84] Chemcraft - graphical software for visualization of quantum chemistry computations. www.chemcraftprog.com

[85] Zhao, Y.; Schultz, N. E.; Truhlar, D. G. *J. Chem. Theory Comput.* **2006**, 2, 364-382.

[86] Perdew, J. P.; Burke, K.; Ernzerhof, M. *Phys. Rev. Lett.* **1996**, 77, 3865-3868.

[87] Chai, J. D.; Head-Gordon, M. *Phys. Chem. Chem. Phys*. **2008**, 10, 6615-6620.

[88] Perdew, J. P. *Phys. Rev. B* **1986**, 22, 8822-8824.

[89] Grimme, S. *J. Comp. Chem.* **2006**, 27, 1787-1799.

[90] a) McWilliams, S. F.; Brennan-Wydra, E.; MacLeod, K. C.; Holland, P. L. *ACS Omega* **2017**, 2, 2594-2606. c) Proppe, J.; Reiher, M. *J. Chem. Theory Comput.* **2017**, 13, 3297-3317. d) Rugg, G.; Senn, H. M. *Phys. Chem. Chem. Phys.* **2017**, 19, 30107-30119.

Chapter 5

Light-activated reactions

5.1 Background

General introduction

Photochemistry is the branch of chemistry focusing on the exploitation of light for the promotion of novel transformations. Photochemistry has a number of appealing features, among them that the energy input can come from an inexhaustible source such as sunlight,[1] and that it usually prevents the use of harder reaction conditions such high temperature or pressure. Photoactivated reactions present an interesting alternative to thermally activated reactions in a number of cases. The photo-excitation of selected reactants can give access to kinetically and thermodynamically unfavourable products.[2] The excited molecule can react in a different manner than its non-excited analogue and in this way surpass a reaction step that is not feasible under thermal conditions.

Despite the benefits, light-driven reactions have been poorly developed for many decades. The main reason is that many organic simple molecules generally interact weakly with light. In addition, its excited states are only accessible upon irradiation at ultraviolet (UV) regions. The photons at these wavefunction regions are highly energetic and can originate undesired photodegradation processes. This has limited the usage of photochemical synthesis in the development of new complex organic molecules or transformations. After all, the energy of a photon in the UV regions can be in the order of some C—C bond breaking energy.[3] In addition, other deactivation routes such as fluorescence, phosphorescence or nonradiative relaxations can exist, all of them returning to the ground state of the molecule.[4]

The development of transition metal-based photosensitizers was a major breakthrough in the field of photochemistry. These complexes are able to transform solar energy into an electrochemical potential,[5,6] and this potential can be applied to the catalysis of useful and unique organic reactions. Some of the features of these metal-based photosensitizers are that they have strong absorption in the visible light spectra and the lifetimes of the excited states are long enough to react with another species. The most common and largely explored photosensitizers are those based on Ru(II) and Ir(III) with chelating polypyridyl ligands.[7,8] Other metal-based photocatalysts bearing Cu,[9] Au [10] or Fe,[11,12] have been recently developed. Organic chromophores, from simple aromatic molecules, to highly conjugated organic systems, have been found to absorb light to promote electron transfer events (Scheme 5.1).[13,14]

Scheme 5.1 Examples of representative transition metal-based (left) and organic (right) chromophores.

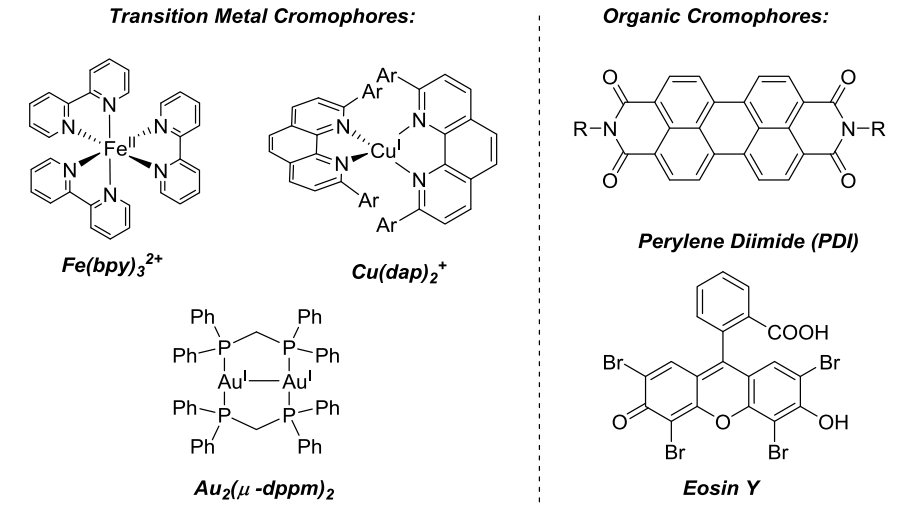

In the context of synthetic organic chemistry, a photocatalyst can play a unique and promising role. The interaction of organic molecules with photocatalysts provides a novel strategy to access radical ions, diradical, or electronically excited organic compounds that usually cannot be generated using non-photochemical approaches.[15] In 2008, two seminal works were published simultaneously by the groups lead by MacMillan and Yoon, both using $Ru(bpy)_3^{2+}$ as photocatalyst. Yoon *et al.* reported the [2+2] cycloaddition of bis(enone) (Scheme 5.2a). Previous studies of this reaction had shown that the cycloaddition step was initiated by a single electron reduction of the enone, thus forming a radical anionic intermediate.[16] Thanks to the intrinsic reactivity of photocatalysts to participate in single electron transfer steps, the replacement of the common catalysts (Cu [17] or Co [18]) by a photocatalysts achieved the product very efficiently, reaching a 95% yield in one hour under sunlight.[19]

The second work, reported by MacMillan *et al.*, consisted in the combination of an asymmetric organocatalyst with the $Ru(bpy)_3^{2+}$ photocatalyst for the direct α-alkylation of aldehydes (Scheme 5.2b). The

mechanism involves two synergistic catalytic cycles where a terminal alkyl radical is generated *via* SET from the photocatalyst to an alkyl halide; and this alkyl is ultimately trapped by the enamine intermediate.[20] The rational design behind this coupling was to imitate photoredox enzymatic catalysis, which replaces highly energetic two-electron steps by low energy single electron pathways.[21]

Scheme 5.2 $Ru(bpy)_3^{2+}$ catalysis for a) cycloaddition of bis(enone) and b) asymmetric alkylation of aldehydes.

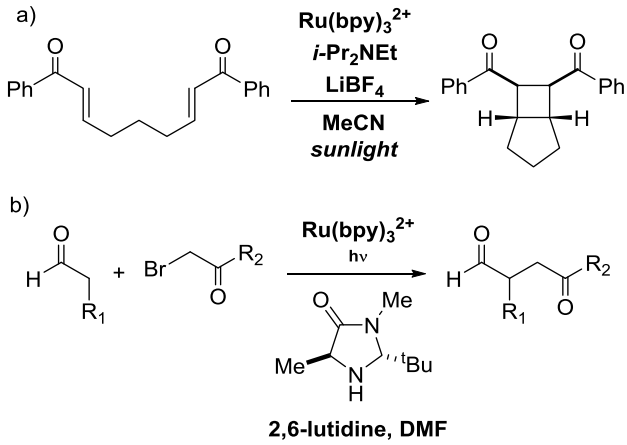

Mechanism of photocatalysis

One of the main reasons why photochemistry is so attractive for the synthetic community is the ability of the photoexcited chromophore to react *via* single electron transfer (SET) steps. This novel reactivity is complementary to the more classical two electron chemistry.[22,23] This approach has been extensively used to obtain products that otherwise are not affordable. The type of reactions that run thanks to the photoinduced electron transfer (PET) steps promoted by excited photocatalysts are called photoredox catalysis in the chemical Literature. A photogenerated electronically excited state molecule **PS*** is both a stronger reductant and a stronger oxidant species than its ground state analogue. Thus, upon the irradiation process, two photocatalytic scenarios exist. If the initial substrate oxidizes the excited form of the

photocatalyst, the pathway is termed oxidative quenching cycle (Scheme 5.3 in purple). The photocatalyst is one-electron oxidized to its electron poor derivative, $\mathbf{PS^+}$. In contrast, if the first one-electron transfer is from the substrate to the electronic excited photocatalysts, this pathway is called reductive quenching cycle (Scheme 5.3 in green). The photoredox catalyst is reduced to its electron rich derivative $\mathbf{PS^-}$ while the substrate is oxidized. In both cases, the photocatalyst is regenerated later on to its initial ground state by accepting or donating an electron (Scheme 5.3). [24]

Scheme 5.3 Different pathways in photoredox catalysis. PS represents the photosensitizer. A, D and S stand for acceptor, donor and substrate, respectively.

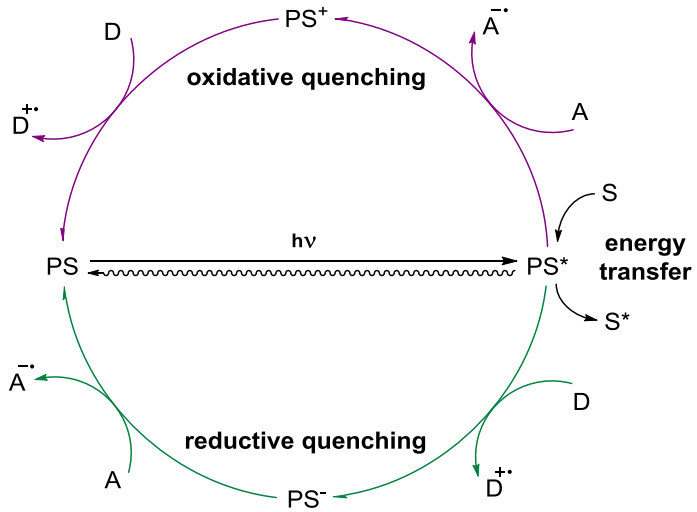

Another possible mechanism, although less common, is the direct energy transfer from the excited photocatalyst to the substrate (Scheme 5.3 in black). One of the mechanisms to describe this event was firstly proposed by Dexter.[25] This non-radiative transition can be viewed as a bilateral electron exchange between the photocatalyst in the excited state and the substrate in its ground state. The result of the energy transfer is that the photocatalyst recovers the initial ground state and the substrate moves to the excited state (Scheme 5.4). This process is only operative if the reaction step is thermodynamically favourable and it

requires a good overlap between the involved orbitals in the donor and the acceptor. This mechanism occurs at distances typically within 10 Å,[26] while other energy transfer processes happen at larger distances. Energy transfer processes are relatively scarce compared to the photoredox processes explained above and will not be further discussed in this thesis.

Scheme 5.4 Dexter energy transfer diagram from an electronic excited photocatalyst to a substrate.

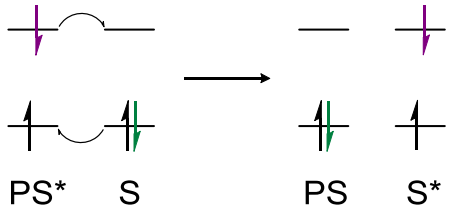

A differentiation must be made with this kind of reactivity and the photoactivated reactions where no electron transfer step is found during the reaction mechanism. In our group we have recently explored this kind of transformations but they will not be discussed in this thesis.[27,28]

Experimental overview

Nickel catalysis has been a highly exploited field in recent years, with many new and impressive transformations.[29] One of the main reasons for the development on nickel-based reactions is the necessity to replace second and third row transition metals. Nickel is more abundant and less toxic, thus appealing for a more sustainable chemistry. In addition, nickel-based complexes has been shown to perform extraordinarily in many important reactions such as cross-coupling,[30] reductive coupling,[31] and photoredox catalysis.[32]

A peculiarity of nickel-based complexes is the availability of different oxidation states: from Ni(0) to Ni(III). Even some species of Ni(IV)

have been recently characterized.[33,34] Nickel exhibits an inherent ability to change its oxidation state in one unit at a time,[35] which is complementary to the more conventional two-electron chemistry found in other metals such as palladium.[36,37] This makes the merging of nickel-based catalysts with photoredox active species appealing. Following this approach, several strategies based on single electron transfer (SET) steps were developed.[38,39] These so-called dual-catalysts systems react in a symbiotic manner, merging the properties of both individual processes and achieving novel reactivity not possible with any of each catalysts independently.[40] Computational characterization studies of the mechanism for these dual nickel/photoredox systems are still scarce.[41,42,43]

In this chapter we will present our DFT computational characterization of the full catalytic mechanism for a photoredox nickel-based process. The reactions is the regioselective synthesis of indolines from iodoacetanilides and 1-alkenes reported by Tasker and Jamison (Scheme 5.5).[44] This approach presents two main points of interest: the reductive elimination to form C_{sp3}—N bonds is inherently challenging and this step must outcompete the β-hydride elimination (which would form Heck-type undesired products). In what follows, we will introduce the most interesting results reported in the original experimental work.

Scheme 5.5 Regioselective synthesis of indoline using Ni/Ru photoredox catalysis reported by Jamison and co-workers.[44]

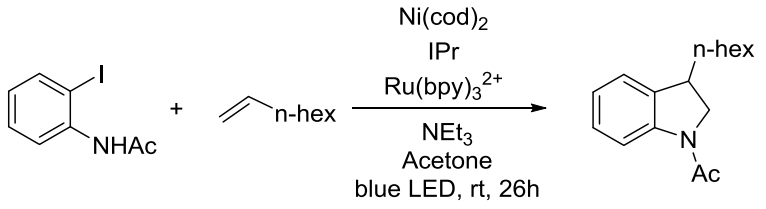

The reaction optimization is shown in Table 5.1. The selected nickel pre-catalyst was $Ni(cod)_2$. First, they tested the conditions similar to

those of a Heck reaction (entry 1) and found that for different electrophiles, protecting groups on the aniline moiety, bases and ligands, only Heck products were obtained. The use of N-heterocyclic carbene (NHC) ligand IPr reported small amounts of the desired indoline product (entry 2). Although the yield was very low (7%), the indoline product (**C**) was obtained in a high selectivity (>19:1) compared to all other products (**D**-**F**). Substituting the protecting group of the aniline by acetate showed a small increase on the indoline product yield (up to 14%) when tested with different electrophiles, although the selectivity was lower (> 10:1) (entry 3).

Table 5.1 Reaction optimization for the indoline synthesis reaction.

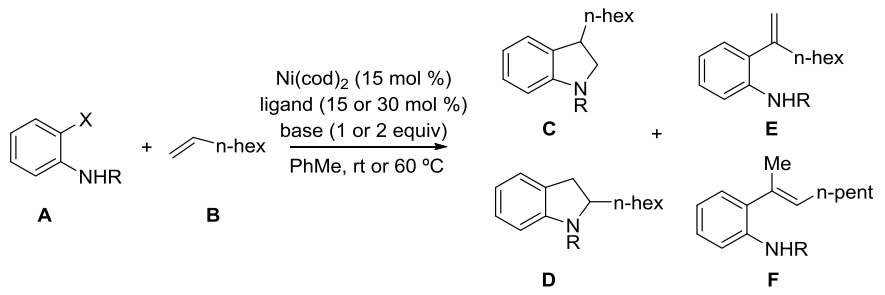

entry	X; R	ligand	base	yield C
1	OTf; Piv	phosphine, PyBOX	various organic/inorganic	0 %
2	OTf; Piv	IPr	LiOt-Bu	7 %
3	Cl, OTf, Br, I; Ac	IPr	LiOt-Bu	10 - 14 %
4	Br, Ac	IPr, $[Ru(bpy)_3]$	2,6-lutidine	15 %
5	Br, Ac	IPr, $[Ru(bpy)_3]$, 66 h	NEt_3	33 %
6	I, Ac	IPr, $[Ru(bpy)_3]$, 26 h	NEt_3	88 %

Inspired by the reports on dual nickel/photoredox systems by Molander [45] and Doyle and MacMillan,[46] they decided to introduce a photoredox catalyst in the reaction mixture. Entries 4 and 5 showed an important increase on the indoline product formation when $[Ru(bpy)_3]$ photocatalysts was introduced to the reaction solution. Further optimi-

zation using triethylamine as base and aryl iodides instead of bromides (entry 6), reported almost quantitative yields in high selectivity for the formation of the indoline product (>19:1) over the Heck products.

With the optimal conditions in hand, they explored the scope of this transformation. The reaction tolerates several substituents on the 4- and 5-positions on the aryl ring, both electron donating and withdrawing groups. However, substitution on the 3- or 6- positions lowers the yield of the indoline product. An increase of 10 °C on the reaction conditions improves the reactions yields, although greater amounts of products of the *β*-hydride elimination were also observed. Interestingly, substitution of the iodine by bromine reduced the indoline product yield from 88 to 27 % (Scheme 5.6).

Scheme 5.6 Selected examples of the scope of aryl electrophile.

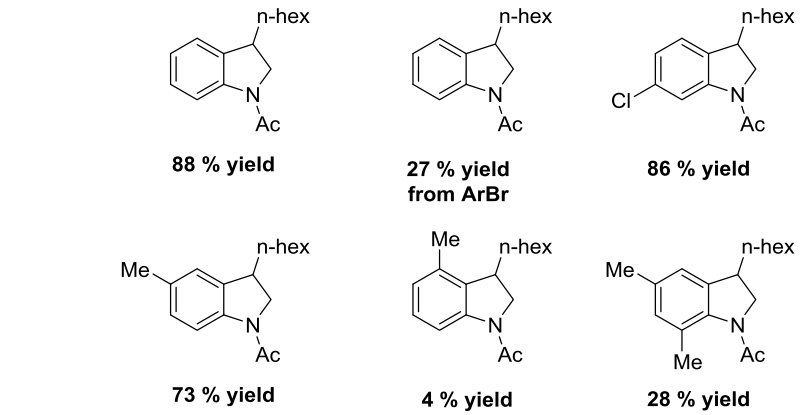

The scope of the alkene substrate was also analyzed (Scheme 5.7). The reaction, again, tolerates a wide variety of functional groups on the alkene moiety, including trimethylsilyl or protected alcohols and amines. Styrenyl substrates were also well tolerated, although the selectivity toward the indoline product is notably reduced for this kind of reagents. Internal and 1,1-disubstituted alkenes were not able to afford the desired product.

Scheme 5.7 Selected examples of the scope of alkene coupling partner.

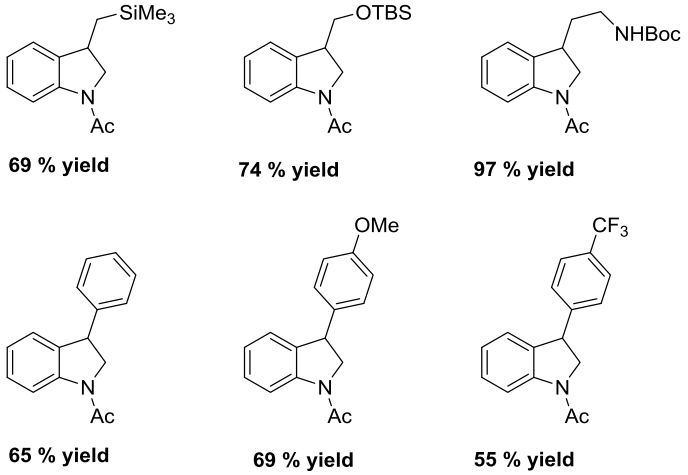

To gain more insight in the complex mechanism governing this reaction, they performed some mechanistic studies. In order to check if the Heck product **E** was an intermediate of the reaction, they performed the reaction introducing amounts of **E** independently synthetized. The reagent **E** was completely recovered indicating that it is not an intermediate of the reaction for the formation of the indoline product (Scheme 5.8a). The second mechanistic study was to run the reaction between **A** and **B** in stoichiometric conditions without the presence of the photoredox catalysts. Portions of the reaction mixture were then exposed to different oxidants (Scheme 5.8b). Without an oxidant, very few indoline product was observed, and several other products were found in trace amounts. When stirred open to air or adding $PhI(OAc)_2$, significant amounts of **C** were obtained with good selective for the indoline product (75 and 60%, respectively). Interestingly, addition of catalytic $Ru(bpy)_3^{2+}$ did not produce the indoline product. Probably this is due to the larger excess of nickel complexes which leads to undesired and unproductive reduction/oxidation or deactivation of the photoredox catalysts. In summary, an oxidation, presumably from Ni(II) to Ni(III), is necessary to achieve the C—N bond formation step.

Scheme 5.8 Experimental mechanistic studies.

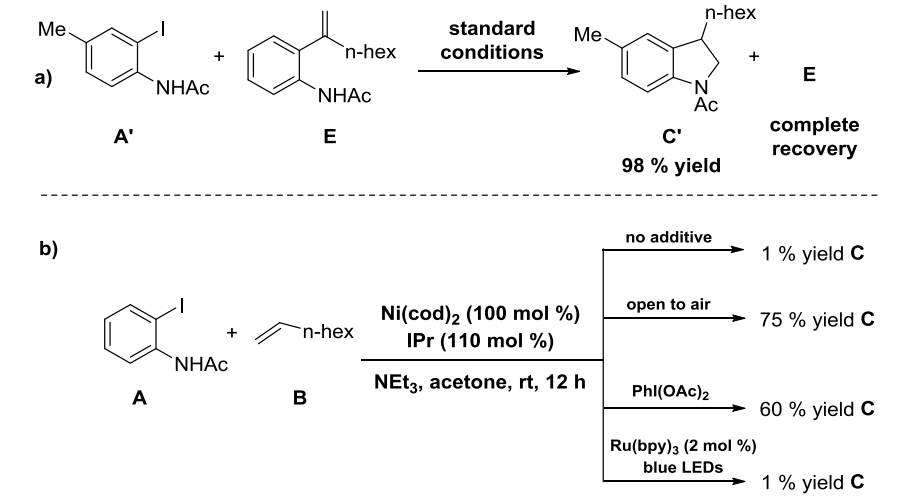

Finally, they were able to characterize by X-ray and NMR some intermediates of the catalytic cycle. In particular, the crystal structures of species resulting from the oxidative addition and migratory insertion steps were obtained. Further investigation by cyclic voltammetry (CV) shown that the potential wave for the Ni(I/0) transition is -0.74 V vs SCE, suggesting that it can be easily reduced by $Ru(bpy)_3^+$ ($E_{1/2}^{II/I}$ = -1.33 V vs SCE in MeCN).[5] In addition, the potential for the Ni(II/III) oxidation was +0.80 V vs SCE, suggesting also that it can be oxidized by $*Ru(bpy)_3^{2+}$ (+0.77 V vs SCE in MeCN).[5]

The wealth of experimental data, together with the number of remaining mechanistic uncertainties, makes this system highly appealing for a computational study. This is a chemically relevant process where for the first time the photoredox catalyst appears to oxidize and reduce the nickel directly. We selected 2'-iodoacetanilide (**A**) and octene (**B**) as representative reagents for the study of the full catalytic cycle. This combination of reagents reports the best experimental results and is relatively easy to model computationally.

5.2 Computational details

Computational method

In this chapter 5, we carried out all the calculations using Gaussian09 (D.01) [47] at the B3LYP level of theory.[48] Grimme empirical dispersion was introduced with the GD3 term on all the optimizations calculations.[49] The solvation was introduced implicitly in all the optimizations using the SMD model with the experimental solvent, acetone (ε=20.493).[50] Considering the possible presence of different charged structures in the mechanism, we included diffuse functions in the basis set, even in the geometry optimizations. For optimizations and frequency calculations, we combined the LANL2DZ basis set for nickel and iodine atoms (with the associated pseudopotential),[51] and the 6-31+G(d) basis set for the rest of the atoms.[52] In order to minimize the basis set superposition error (BSSE), potential energies were further refined using 6-311++G(d,p) [53] for C, H, N, O atoms, LANL2DZdp[54] for the I atom and LANL2TZ(f) [55] for the Ni atom.

All geometry optimizations were carried out without symmetry restrictions. All the stationary points were assigned to minima (zero imaginary frequencies) or transition states (one imaginary frequency) by frequency analysis. Free energy corrections were calculated at 298.15 K and 105 Pa pressure, including Zero Point Energy (ZPE) corrections.

The barrier for the outer-sphere single electron transfer (SET) steps was estimated with Marcus theory, following the methodology explained in chapter 2.

All the 3D structures were drawn with CYLview program.[56]

5.3 Reaction mechanism

Oxidative addition *vs* halide abstraction

We started our computational study with the experimentally observed Ni(0) complex **1**. We first studied the coordination of a second octene molecule, resulting in **1'**, and the decoordination of octane, resulting in **1"**. Both **1'** and **1"** are higher energy intermediates, 4.3 and 26.8 kcal·mol^{-1} above **1**, respectively. We discarded them and studied the interaction of the initial reactant **A** with complex **1**. Based on previous studies in our group on the reaction of aryl halides with Ni(0) species,[57] two different pathways were considered: oxidative addition and halide abstraction (Figure 5.1).

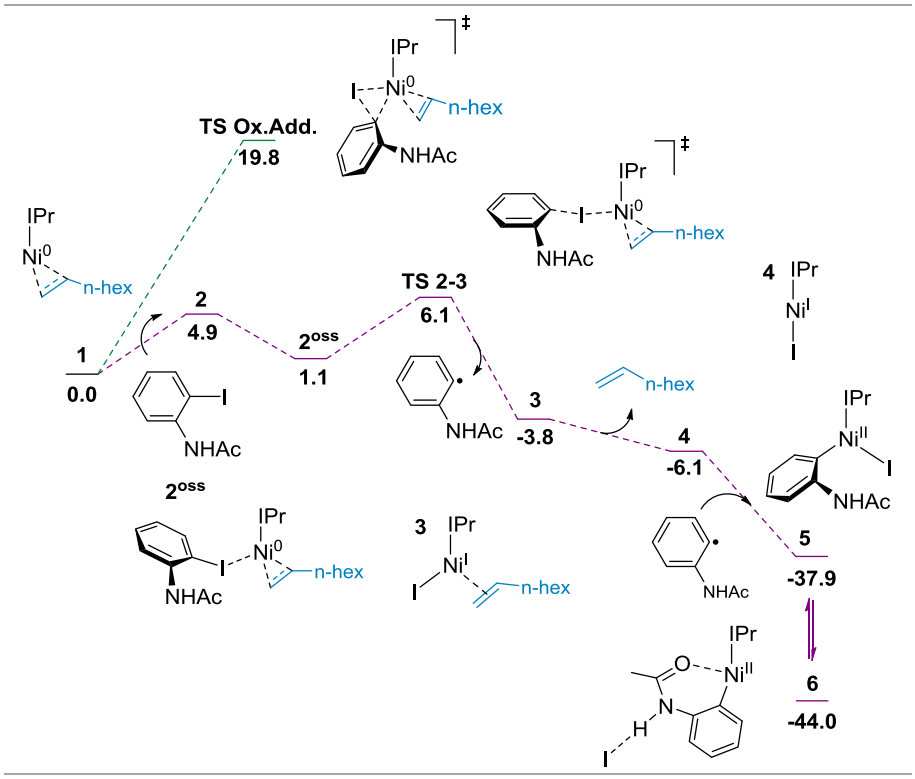

Figure 5.1 2-iodoacetanilide (**A**) activation by IPrNi(0) catalysts *via* concerted oxidative addition (in green) and halide abstraction (in purple). Free energies in kcal·mol^{-1}.

The concerted oxidative addition of **A** to the Ni(0) complex **1** (Figure 5.1, in green) has an activation barrier of 19.8 kcal·mol^{-1}. Although the barrier found was affordable at the reaction conditions, we decided to check the pathway for the halide abstraction (Figure 5.1, in purple). This mechanism starts with the interaction of **A** with the Ni(0) center, **2**, with the iodine atom pointing towards the nickel atom. This adduct **2** is found at 4.9 kcal·mol^{-1} from **1** and can rapidly evolve to the more stable form **2**^{oss} in the open-shell singlet surface, stabilizing the system by 3.8 kcal·mol^{-1}. Finally, the transition state **TS 2-3** associated with the halide abstraction mechanism takes place, with a low barrier of 6.1 kcal·mol^{-1}. This transition state runs *via* inner-sphere single electron transfer (SET) from the Ni metal center to the σ* C—I antibonding orbital. It involves the simultaneous cleavage of the C—I bond and formation of the new Ni—I bond. Figure 5.2 shows the 3D structure of **TS 2-3** with the corresponding spin population depicted in each atom participating in the SET step.

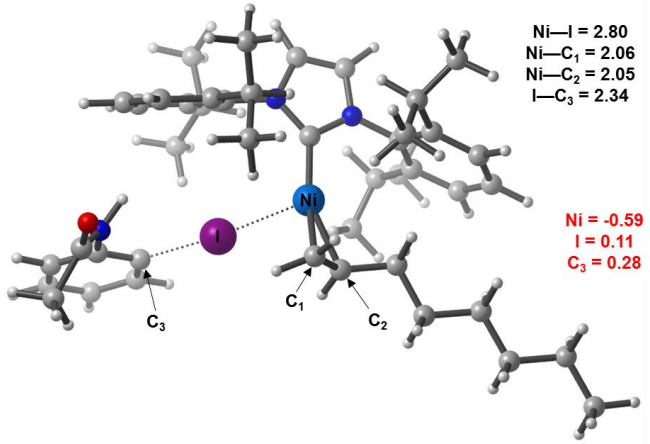

Figure 5.2 3D optimized structure of the transition state for the halide abstraction (**TS 2-3**). Relevant bond distances in Å and atomic spin densities in red.

TS 2-3 evolves to a new Ni(I) species **3**. An aryl radical is released in the same step. This intermediate **3** is 3.8 kcal·mol^{-1} below **1** and can easily decoordinate the initial alkene, leading to intermediate **4**. Complex **4**

subsequently traps the aryl radical and the Ni(II) intermediate **5** is obtained, 37.8 kcal·mol^{-1} from the initial reactants. The next step is a rearrangement to place the O atom of the carbonyl group coordinated to the metal center, resulting in intermediate **6**, 44.0 kcal·mol^{-1} below **1**. The high exergonicity of this step makes it irreversible and facilitates the detection of intermediate **6** by X-ray and NMR spectroscopy. It is worth remarking that the existence of the Ni(I) intermediate **3** decreases the activation barrier to access the Ni(II) species **6**.

Migratory insertion

We explored the regioselective alkene migratory insertion into the Ni—C bond from complex **6**. Figure 5.3 shows the two lower energy pathways. In agreement with the experimental results, our calculations find that the alkene insertion takes place with the alkyl chain close to the aryl ring to form preferentially intermediate **7** (Figure 5.3, in purple). We found all the possible transition state to form the relative regioisomers of **7**. The transition state **TS 6-7** is the most stable, 3.9 kcal·mol^{-1} below the second more stable transition state **TS 6-7'**, which would lead to intermediate **7'** (Figure 5.3, in green). The difference in energy between the two transition states can be attributed to the steric clash between the alkyl chain and the N-heterocyclic carbene (NHC) ligand in **TS 6-7'**.

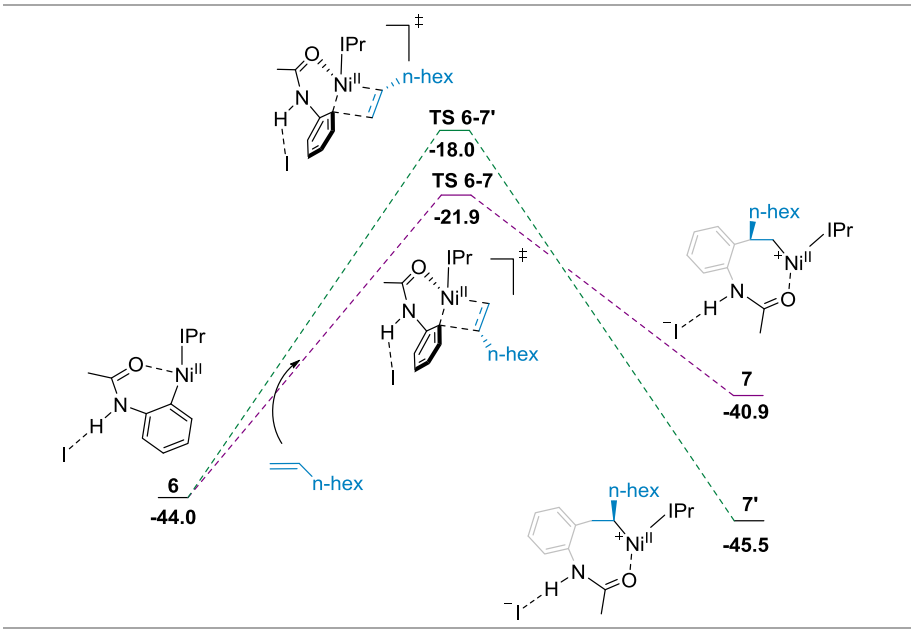

Figure 5.3 Free energy profile for the regioselective alkene insertion into the Ni-C bond from intermediate **6**. Energies in kcal/mol.

This energy difference can be further rationalized through the interaction between the Ni center and the oxygen atom of the carbonyl group, which is much stronger in **TS 6-7** (2.02 Å) than in **TS 6-7'** (2.33 Å) (Figure 5.4). The importance of the O atom interaction with the Ni center in the migratory insertion step will be addressed later in another subsection.

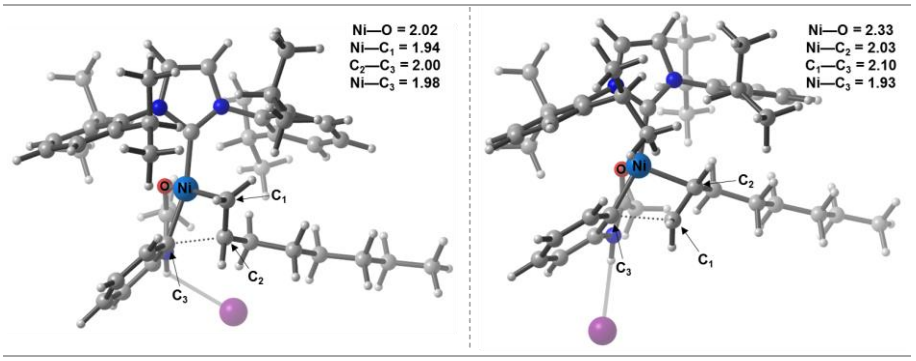

Figure 5.4 3D structures of lower transition states for the migratory insertion step, **TS 6-7** (left) and **TS 6-7'** (right). Selected distances in Å.

Although intermediate **7'** is more stable than **7** by 4.6 kcal·mol^{-1}, this is kinetically irrelevant, as the next steps of the catalytic cycle are downhill and the formation of **7** becomes irreversible.

Final steps of the mechanism

The reaction continues with the rearrangement and deprotonation steps shown in Figure 5.5. The ligand rearranges in the coordination sphere of nickel to bring the nitrogen atom close to the Ni center, while the O atom of the carbonyl moiety decoordinates. In this disposition, the NEt_3 base is able to deprotonate complex **8** in a downhill manner. The deprotonated complex **9** is found at 12.4 kcal·mol^{-1} below intermediate **7**. Alternative pathways were investigated for this step, for instance, changing the order between rearrangement and deprotonation. However, all of them were higher in energy.

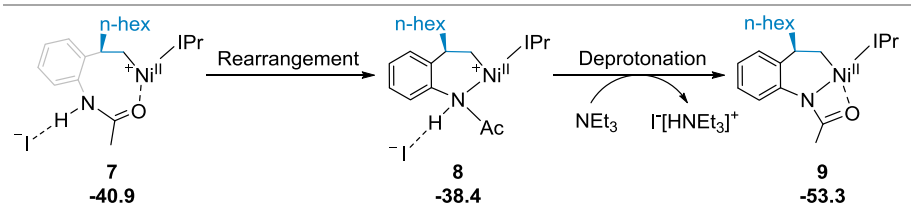

Figure 5.5 Rearrangement and deprotonation steps. Energies in kcal·mol^{-1}.

The evolution of intermediate **9** into products is shown in the free energy profile in Figure 5.6. The Ni(II) intermediate **9** has the perfect stoichiometry to form the indoline product *via* direct reductive elimination. The computed barrier is however extremely high. The transition state associated with this step **TS 9-Ni(II)** involves a barrier of 66.0 kcal·mol^{-1} (Figure 5.6, in green). Here is where the photosensitizer plays a crucial role.

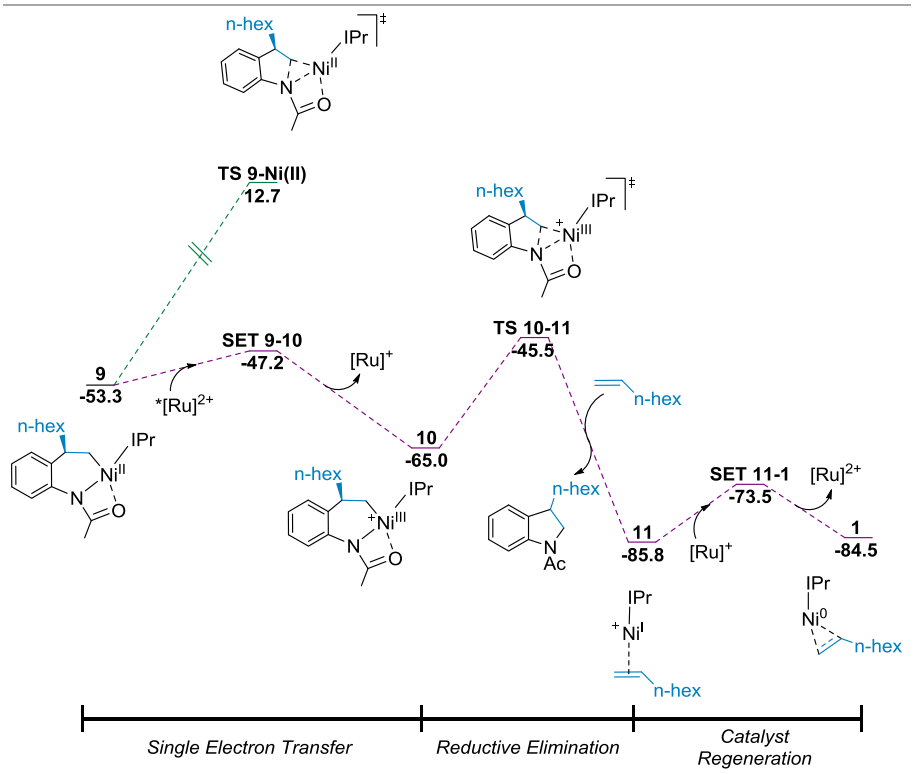

Figure 5.6 Free energy profile for the indoline formation from intermediate **9**. Energies in kcal·mol^{-1}. [Ru] stands for [Ru(bpy)$_3$] and *[Ru] for the excited state.

The excited state of the Ru-photoredox catalyst has a high oxidation potential capable to oxidize the Ni(II) intermediate **9** to the Ni(III) complex **10** in a thermodynamically favourable step (Figure 5.6, in purple). Thus, we estimated the barrier for the outer-sphere single electron transfer (SET) event with Marcus theory. The nuclear and solvent reorganization terms were considered following the procedure reported before by our group [58] and introduced in Chapter 2. The outer-sphere **SET 9-10** has a low barrier of 6.1 kcal·mol^{-1}, generating the stable Ni(III) complex **10**. From this intermediate **10**, the reaction evolves towards the formation of the indoline product **C** through the reductive elimination transition state **TS 10-11**, with a barrier of 19.5 kcal·mol^{-1}. The tremendous change in the reaction barrier after the oxidation of the metal center has been recently characterized also in an iridium system,

and the process has been labeled as oxidatively induced reductive elimination (OIRE).[59]

Finally, the initial Ni(0) species **1** and the Ru(II)-photoredox catalyst are regenerated by a second outer-sphere SET step closing both photo- and non-photocatalyzed cycles, **SET 11-1**. Again, the Marcus theory was applied to estimate the barrier for the SET step. The energy barrier found was 12.3 kcal·mol^{-1} from intermediate **11**. Although this step is mildly endergonic, the low barrier found for the halide abstraction mechanism will push the reaction toward a new catalytic cycle. The electron rebound alternative has a higher kinetic barrier (11.0 kcal·mol^{-1} from **1** to **SET 11-1** *vs* 6.1 kcal·mol^{-1} for **TS 2-3**).

Off cycle reactions

Although the steps depicted above are the most likely to occur, several alternative mechanisms have been calculated.

As mentioned before, the interaction between the O atom of the carbonyl moiety and the metal center has proven decisive for the correct allocation of the lowest energy transition state at the migratory insertion step. For this reason, we decided to calculate the migratory insertion of the alkene from the Ni(II) intermediate **5**, that is, without the O atom interacting with the Ni center. The results are depicted in Figure 5.7. The activation barrier for the migratory insertion from intermediate **5** is *ca.* 40.0 kcal·mol^{-1}. This is prohibitively high for the experimental conditions.

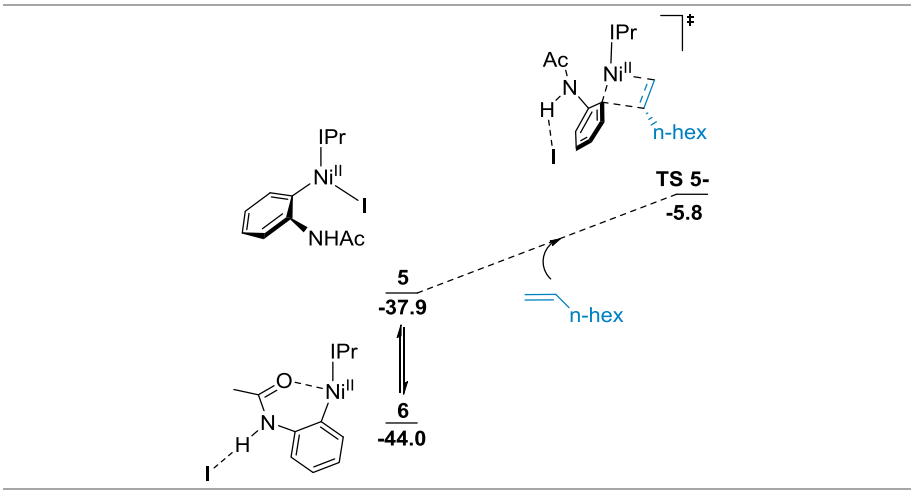

Figure 5.7 Migratory insertion from intermediate **5**. Free energies in kcal·mol^{-1}.

Next, we investigated other possible intermediates of the catalytic cycle where the base NEt_3 could react with the complex to deprotonate it. The results are summarized in Figure 5.8. Deprotonation of intermediate **6** or **7** involves an unfavourable transformation with reaction free energies of 4.6 and 3.3 kcal·mol^{-1}, respectively. In comparison, as reported above, the deprotonation of complex **8** is an exergonic reaction (-14.9 kcal·mol^{-1}).

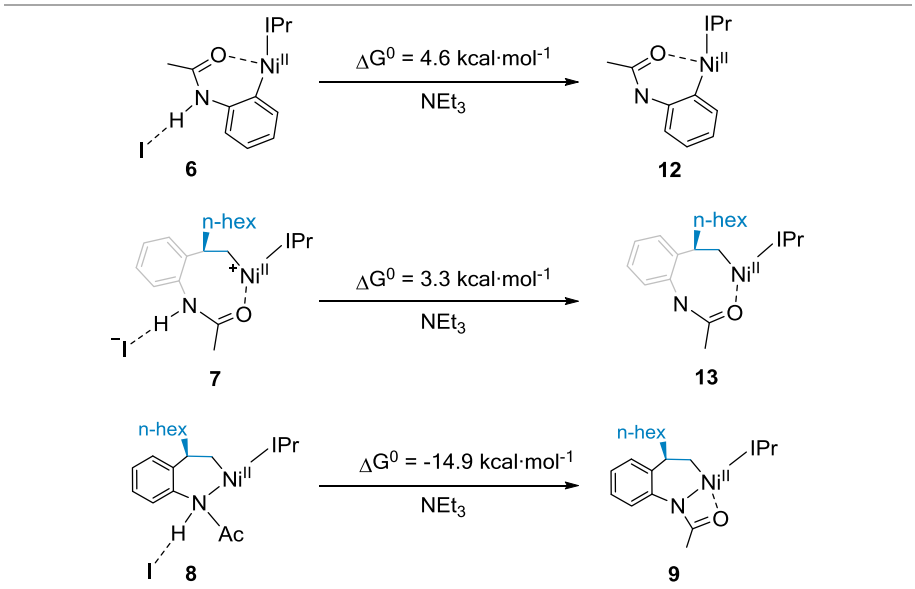

Figure 5.8 Deprotonation and halide abstraction of selected intermediates during the catalytic cycle.

Finally, to confirm the high selectivity towards the formation of the indoline product, we computed the pathway for the *β*-hydride elimination (BHE) mechanism, which would lead to the Heck products **E** and **F**. The results are shown in Figure 5.9. The BHE pathways were calculated from intermediate **7**. Two possible scenarios were considered: external abstraction of the proton by the stochiometric base (NEt_3), $\mathbf{TS_{NEt3}}$ **7-14**; or internal abstraction with the iodine atom, $\mathbf{TS_{iodine}}$ **7-14**. Both transition states have similar activation barrier, 34.6 and 35.8 kcal·mol^{-1}, respectively. Both are too high for the reaction to take place at the experimental conditions. Thus, these results are in total agreement with the experimental data where for the reaction between 2-idoacetanilide and octene, the desired indoline product is obtained in a high selective manner (>19:1).

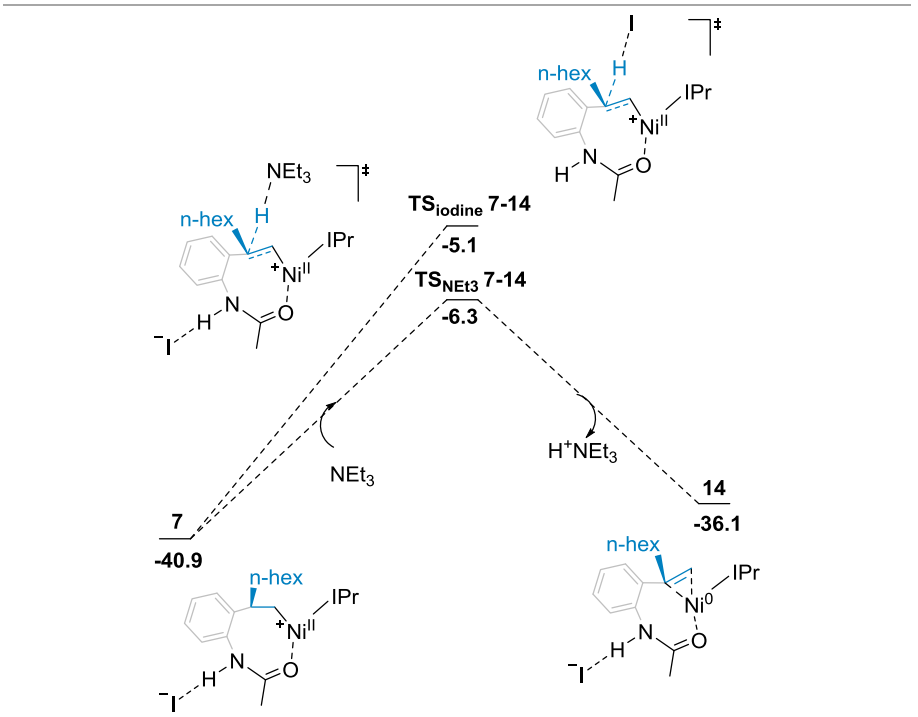

Figure 5.9 Free energy profiles for the β-hydride elimination. Energies in kcal·mol^{-1}.

5.4 Summary

The full mechanism for the indoline synthesis from 2'-iodoacetanilide and octene catalyzed by a Ni/Ru-photoredox dual system has been fully characterized (Scheme 5.9). The first steps of the mechanism can run without irradiation and move between Ni(0), Ni(I) and Ni(II). The first step is the activation of the 2'-iodoacetanalide *via* halide abstraction, followed by the migratory insertion of the alkene into the Ni—C bond. After rearrangement and deprotonation, the Ni(II) species can undergo one-electron oxidation by means of the Ru-photoredox catalyst. Then, the productive Ni(III) complex can undergo reductive elimination and release the indoline product. Finally, the reduced form of the photocatalyst can easily reduce the Ni(I) complex to the initial Ni(0) complex, closing both catalytic cycles.

There are three SET steps during the mechanism. One is inner-sphere and two are outer-sphere. The outer-sphere SET steps have been successfully characterized applying the Marcus theory. The calculated mechanism involves four different oxidation states of the Ni: from Ni(0) to Ni(III), and each one plays a crucial role in the course of the reaction.

Scheme 5.9 Calculated pathway for the full catalytic cycle of indoline formation catalyzed by [IPrNi] and Ru photocatalyst.

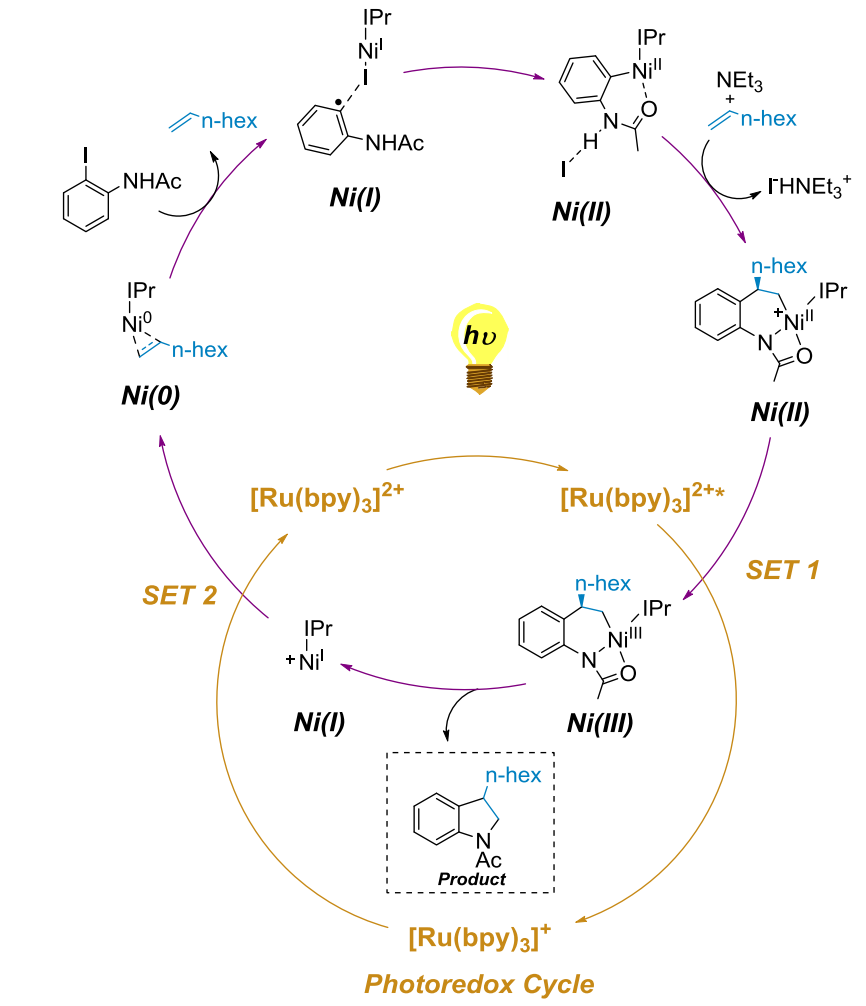

5.5 References

[1] Schultz, D. M.; Yoon, T. P. *Science* **2014**, 343, 1239176.

[2] Oelgemöller, M. *Chem. Rev.* **2016**, 116, 9664-9582.

[3] Bach, T.; Hehn, J.P. *Angew. Chem. Int. Ed.* **2011**, 50, 1000-1045.

[4] Snyder, J. A.; Grüninger, P.; Bettinger, H.F.; Bragg A. E. J. *Phys. Chem. A* **2017**, 121, 5136-5146.

[5] Prier, C. K.; Rankic, D. A.; MacMillan, D. W. C. *Chem. Rev.* **2013**, 113, 5322-5363.

[6] Yoon, T. P.; Ischay, M. A.; Du, J. *Nat. Chem.* **2010**, 2, 527-532.

[7] Arias-Rotondo, D. M.; McCusker, J. K. *Chem. Soc. Rev.* **2016**, 45, 5803-5820.

[8] Flamigni, L.; Barbieri, A.; Sabatini, C.; Ventura, B.; Barigelletti, F. *Top. Curr. Chem.* **2007**, 281, 143-203.

[9] Pirtsch, M.; Paria, S.; Matsuno, T.; Isobe, H.; Reiser, O. *Chem. Eur. J.* **2012**, 18, 7336-7340.

[10] Revol, G.; McCallum, T.; Morin, M.; Gagosz, F.; Barriault, L. *Angew. Chem. Int. Ed.* **2013**, 52, 13342-13345.

[11] Gualandi, A.; Marchini, M.; Mengozzi, L.; Natali, M.; Lucarini, M.; Ceroni, P.; Cozzi, P. G. *ACS Catal.* **2015**, 5, 5927-5931.

[12] Wenger, O. S. *Chem. Eur. J.* **2019**, 25, 6043-6052.

[13] Kainz, Q. M.; Matier, C. D.; Batoszewicz, A.; Zultanksi, S. L.; Peters, J. C.; Fu, G. C. *Science* **2016**, 351, 681-684.

[14] Discekici, E. H.; Treat, N. J.; Poelma, S. O.; Mattson, K. M.; Hudson, Z. M.; Luo, Y.; Hawker, C. J.; Read de Alaniz, J. *Chem. Commun.* **2015**, 51, 11705-11708.

[15] Albini, A.; Fagnoni, M. *Photochemically Generated Intermediates in Synthesis*; 1st Edition, Wiley & Sons: Hoboken, NJ, **2013**.

[16] Yang, J.; Felton, G. A. N.; Bauld, N. L.; Krische, M. J. *J. Am. Chem. Soc.* **2004**, 126, 1634-1635.

[17] Yang, J.; Cauble, D. F.; Berro, A. J.; Bauld, N. L.; Krische, M. J. *J. Am. Chem. Soc.* **2004**, 69, 7979-7984.

[18] Baik, T.-G.; Luis, A. L.; Wang, L.-C.; Krische, M. J. *J. Am. Chem. Soc.* **2001**, 123, 6716-6717.

[19] Ischay, M. A.; Anzovino, M. E.; Du, J.; Yoon, T. P. *J. Am. Chem. Soc.* **2008**, 130, 12886-12887.

[20] Nicewicz D. A.; MacMillan, D. W. C. *Science* **2008**, 322, 77-80.

[21] Gray, H. B.; Winkler, J. R. *Annu. Rev. Biochem.* **1996**, 65, 537-561.

[22] Romero, N. A.; Nicewicz, D. A. *Chem. Rev.* **2016**, 116, 10075-10166.

[23] Levin, M. D.; Kim, S.; Toste, F. D. *ACS Cent. Sci.* **2016**, 2, 293-301.

[24] Tucker, J. W.; Stephenson, C. R. J. *J. Org. Chem.* **2012**, 77, 1617-1622.

[25] Dexter, D. L. *J. Chem. Phys.* **1953**, 21, 836-850.

[26] Monguzzi, A.; Mezyk, J.; Scotognella, F.; Tubino, R.; Meinardi, F. *Phys. Rev. B* **2008**, 78, 195112.

[27] Wegeberg, C.; Fernandez-Alvarez, V. M.; de Aguirre, A.; Frandsen, C.; Browne, W. R.; Maseras, F.; McKenzie, C. J. *J. Am. Chem. Soc.* **2018**, 140, 14150-14160.

[28] Fernandez-Alvarez, V. M.; Ho, S. K. Y.; Britovsek, G. J. P.; Maseras, F. *Chem. Sci.* **2018**, 9, 5039-5046.

[29] Tasker, S. Z.; Standley, E. A.; Jamison, T. F. *Nature* **2014**, 509, 299-309.

[30] a) Han, F.-S. *Chem. Soc. Rev.* **2013**, 42, 5270-5298. b) Ritleng, V.; Henrion, M.; Chetcuti, M. J. *ACS Catal.* **2016**, 6, 890-906. c) Hazari, N.; Melvin, P. R.; Beromi, M. M. *Nat. Rev. Chem.* **2017**, 1, 0025.

[31] a) Everson, D. A.; Weix, D. J. J. *Org. Chem.* **2014**, 79, 4793-4798. b) Börjesson, M.; Moragas, R.; Gallego, D.; Martin, R. *ACS. Catal.* **2016**, 6, 6739-6749.

[32] Shaw, M. H.; Twilton, J.; MacMillan, D. W. C. *J. Org. Chem.* **2016**, 84, 6898-6926.

[33] Camasso, N. M.; Sandford, M. S. *Science* **2015**, 347, 1218-1220.

[34] Bour, J. R.; Ferguson, D. M.; McClain, E. J.; Kampf, J. W.; Sandford, M. S. *J. Am. Chem. Soc.* **2019**, 141, 8914-8920.

[35] Ananikov, V. P. *ACS Catal.* **2015**, 5 1964-1971.

[36] Balcells, D.; Nova, A. *ACS Catal.* **2018**, 8, 3499-3515.

[37] Bonney, K. J.; Schoenebeck, F. *Chem. Soc.* **2014**, 43, 6609-6638.

[38] Skubi, K. L.; Blum, T. R.; Yoon, T. P. *Chem. Rev.* **2016**, 116, 10035-10074.

[39] a) Twilton, J.; Le, C.; Zhang, P.; Sham, M. H.; Evans, R. W.; MacMillan, D. W. C. *Nat. Rev. Chem.* **2017**, 1, 0052. b) Tellis, J. C.; Kelly, C. B.; Primer, D. N.; Jouffroy, M.; Patel, N. R.; Molander, G. A. *Acc. Chem. Res.* **2016**, 49, 1429-1439.

[40] Hopkinson, M. N.; Sahoo, B.; Li, J.-L.; Glorius, F. *Chem. Eur. J.* **2014**, 20, 3874-3886.

[41] Gutierrez, O.; Tellis, J. C.; Primer, D. N.; Molander, G. A.; Kozlowski, M. C. *J. Am. Chem. Soc.* **2015**, 137, 4896-4899.

[42] Qi, Z.-H.; Ma, J. *ACS Catal.* **2018**, 8, 1456-1463.

[43] Lim, C.-H.; Kudisch, M.; Liu, B.; Miyake, G. M. *J. Am. Chem. Soc.* **2018**, 140, 7667-7673.

[44] Tasker, S. Z.; Jamison, T. F. *J. Am. Chem. Soc.* **2015**, 137, 9531-9534.

[45] Tellis, J. C.; Primer, D. N.; Molander, G. A. *Science* **2014**, 345, 433-436.

[46] Zuo, Z.; Ahneman, D. T.; Chu, L.; Terrett, J. A.; Doyle, A. G.; MacMillan, D. W. C. *Science* **2014**, 345, 437-440.

[47] Frisch, M. J.; Trucks, G. W.; Schlegel, H. B.; Scuseria, G. E.; Robb, M. A.; Cheeseman, J. R.; Scalmani, G.; Barone, V.; Mennucci, B.; Petersson, G. A.; Nakatsuji, H.; Caricato, M.; Li, X.; Hratchian, H. P.; Izmaylov, A. F.; Bloino, J.; Zheng, G.; Sonnenberg, J. L.; Hada, M.; Ehara, M.; Toyota, K.; Fukuda, R.; Hasegawa, J.; Ishida, M.; Nakajima, T.; Honda, Y.; Kitao, O.; Nakai, H.; Vreven, T.; Peralta, J. E., Jr; Ogliaro, F.; Bearpark, M.; Heyd, J. J.; Brothers, E.; Kudin, K. N.; Staroverov, V. N.; Kobayashi, R.; Normand, J.; Raghavachari, K.; Rendell, A.; Burant, J. C.; Iyengar, S. S.; Tomasi, J.; Cossi, M.; Rega, N.; Millam, J. M.;

Klene, M.; Knox, J. E.; Cross, J. B.; Bakken, V.; Adamo, C.; Jaramillo, J.; Gomperts, R.; Stratmann, R. E.; Yazyev, O.; Austin, A. J.; Cammi, R.; Pomelli, C.; Ochterski, J. W.; Martin, R. L.; Morokuma, K.; Zakrzewski, V. G.; Voth, G. A.; Salvador, P.; Dannenberg, J. J.; Dapprich, S.; Daniels, A. D.; Farkas, O.; Foresman, J. B.; Ortiz, J. V.; Cioslowski, J.; Fox, D. J. Gaussian 09, revision D.01; Gaussian Inc.: Wallingford, CT, **2013**.

[48] a) Becke, A. D. *J. Chem. Phys.* **1993**, 98, 1372-1377. b) Becke, A. D. *J. Chem. Phys.* **1993**, 98, 5648- 5652. c) Lee, C.; Yang, W.; Parr, R. G. *Phys. Rev. B* **1988**, 37, 785-789. d) Stephens, P. J.; Devlin, F. J.; Chabalowski, C. F.; Frisch, M. J. *J. Phys. Chem.* **1994**, 98, 11623-11627.

[49] Grimme, S.; Antony, J.; Ehrlich, S.; Krieg, H. *J. Chem. Phys.* **2010**, 132, 154104.

[50] Marenich, A. V.; Cramer, C. J.; Truhlar, D. G. *J. Phys. Chem. B* **2009**, 113, 6378-6396.

[51] Hay, P. J.; Wadt, W.R. *J. Chem. Phys.* **1985**, 82, 270-283.

[52] a) Hehre, W. J.; Ditchfield, R.; Pople, J. A. *J. Chem. Phys.* **1972**, 56, 2257-2261. b) Hariharan, P. C.; Pople, J. A. *Theor. Chim. Acta* **1973**, 28, 213-222. c) Francl, M. M.; Pietro, W. J.; Hehre, W. J.; Binkley, J. S.; Gordon, M. S.; DeFrees, D. J.; Pople, J. A. *J. Chem. Phys.* **1982**, 77, 3654-3665.

[53] a) Krishnan, R.; Binkley, J. S.; Seeger, R.; Pople, J. A. *J. Chem. Phys.* **1980**, 72, 650-654. b) McLean, A. D.; Chandler, G. S. *J. Chem. Phys.* **1980**, 72, 5639-5648.

[54] Check, C. E.; Faust, T. O.; Bailey, J. M.; Wright, B. J.; Gilbert, T. M.; Sunderlin, L. S. J. *Phys. Chem. A* **2001**, 105, 8111-8116.

[55] Roy, L. E.; Hay, P. J.; Martin, R. L. *J. Chem. Theory Comput.* **2008**, 4, 1029-1031.

[56] Legault, C. Y. CYLview, 1.0b; Université de Sherbrooke: Quebec, Montreal, Canada, **2009**; www.cylview.org

[57] a) Funes-Ardoiz, I.; Nelson, D. J.; Maseras, F. *Chem. Eur. J.* **2017**, 23, 16728-16733. b) Nelson, D. J.; Maseras, F. *Chem. Commun.* **2018**, 54, 10646-10649.

[58] a) Fernandez-Alvarez, V. M.; Nappi, M.; Melchiorre, P.; Maseras, F. *Org. Lett.* **2015**, 17, 2676-2679. b) Fernandez-Alvares, Maseras, F. *Org. Biomol. Chem.* **2017**, 15, 8641-8647.

[59] Shin, K.; Park, Y.; Baik, M.-H.; Chang, S. *Nat. Chem.* **2018**, 10, 218-224.

UNIVERSITAT ROVIRA I VIRGILI
NON-INNOCENT LIGANDS: FROM PRO-TON SHUTTLE TO PHOTO-ACTIVATION
Adiran de Aguirre Fondevila

Chapter 6

Conclusions

We have shown that Density Functional Theory calculations are very useful for the characterization of mechanism of different ligand metal cooperation reactions. The reported results will help in the rational design of new systems bearing proton-, electron- and photo-responsive ligands. The following paragraphs outline the most relevant conclusions on each chapter.

Chapter 3:

- We have elucidated the different reactivity of the chloro and acetate ligands in $[Ru(X)H(CO)(P\textit{i}Pr_3)_2]$ (X= Cl or OAc) complexes for the activation of phenylacetylene . The chloro system reacts with one molecule of phenylacetylene to form the alkenyl derivative. The acetate system can react further with a second equivalent of phenylacetylene to achieve the alkynyl complex.
- This enhanced reactivity is governed by the acetate ligand. The calculations shown that it assists on the C—H bond ac-

tivation step via concerted metalation deprotonation mechanism and subsequently delivers the proton to a different part of the complex. The later mechanism is a variation of the ligand-assisted proton shuttle (LAPS). The acetate ligand delivers the H between two mutually *trans* ligands. This is a first time that a mechanism of this type has been characterized.

- This new variation of the LAPS mechanism can be extrapolated from the reported catalytic behavior of this kind of complexes in the hydrosilylation reactions of 1-alkynes. The acetate ligand can assist on the Si—H activation step and deliver one moiety to the *trans* ligand.

Chapter 4:

- We have characterized a series of $[Fe(N_2S_2)(L)]^n$ (L= none, $P(OMe)_3$, CO and n = -1, 0, +1) complexes. We have been able to elucidate the electronic structure of these complexes with Density Functional Theory.
- The DFT results have shown that the oxidation and reduction of the initial $[Fe(N_2S_3)]^0$ complex is ligand based. The analysis of the spin density in different parts of the complex, together with the natural orbital analysis shows that the formal oxidation state of the metal is Fe(III) throughout all the redox processes.
- The computational studies on the hydroboration of benzaldehyde catalyzed by $[Fe(N_2S_3]^0$ suggest that the rate-determining step of the reaction must be the H—B bond activation. Unfortunately, we have not been able to find a low energy transition state for the homolytically cleavage of this bond. The speciation study after the H—B bond activation step has allowed the identification of many possible intermediates that are capable to complete the hydroboration of

benzaldehyde with low barriers at the experimental conditions.

- These results constitute a good starting point for future research in the group on the elucidation of the real mechanism governing this transformation.

Chapter 5:

- We have fully characterized the mechanism for the indoline synthesis from 2'-iodoacetanilide and octene catalyzed by a combination of Ni/Ru-photoredox dual system.
- Four oxidation states of Ni are found during the catalytic cycle: from Ni(0) to Ni(III). Each one plays a crucial role in the course of the reaction.
- Three different single electron transfer steps have been characterized during the proposed mechanism. The outer-sphere SET steps have been successfully estimated applying the Marcus theory.
- The regioselective determining step is the migratory insertion of the octene into the Ni—C bond. The IPr ligand together with the substituent on the alkene controls this step.
- Several off-cycle reactions have been studied to account for the high regioselectivity of the reaction. For instance, the β-hydride elimination pathways reported high activation barriers, not affordable at the experimental conditions.

UNIVERSITAT ROVIRA I VIRGILI
NON-INNOCENT LIGANDS: FROM PRO-TON SHUTTLE TO PHOTO-ACTIVATION
Adiran de Aguirre Fondevila

UNIVERSITAT ROVIRA I VIRGILI
NON-INNOCENT LIGANDS: FROM PRO-TON SHUTTLE TO PHOTO-ACTIVATION
Adiran de Aguirre Fondevila

UNIVERSITAT ROVIRA I VIRGILI
NON-INNOCENT LIGANDS: FROM PRO-TON SHUTTLE TO PHOTO-ACTIVATION
Adiran de Aguirre Fondevila

NON-INNOCENT LIGANDS: FROM PRO-TON SHUTTLE TO PHOTO-ACTIVATION

Adiran de Aguirre Fondevila